A junction level study of the activation process in nanowire networks

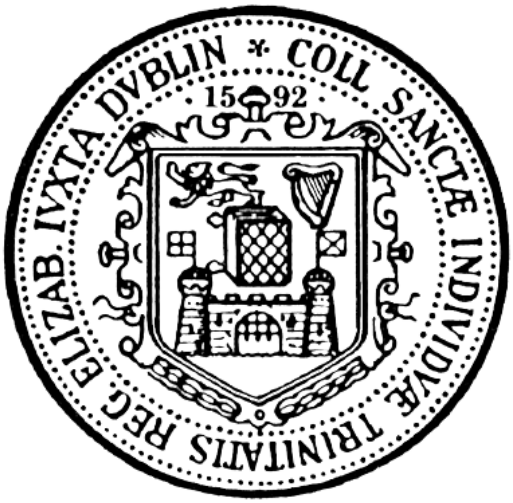

A thesis presented to the University of Dublin, Trinity College

for the degree of

Doctor of Philosophy in Chemistry

by

Fabio Niosi

Under the supervision of Prof. John Boland

School of Chemistry & CRANN

Trinity College Dublin

2019

Declaration

I, the undersigned, declare that this work has not previously been submitted as an exercise for a degree at this, or any other University, and that unless otherwise stated is my own work. Elements of this work that have been carried out jointly with others or by collaborators have been duly acknowledged in the text.

I agree to deposit this thesis in the University's open access institutional repository or allow the library to do so on my behalf, subject to Irish Copyright Legislation and Trinity College Library conditions of use and acknowledgement.

_____ _____

Fabio Niosi Date

Summary

Over the past decade, the growth and continued improvement of electronic devices has pushed technologies beyond perceived limits. Extremely complicated devices based on single atom transistors and touch-screens made of an expensive and rare materials are examples of the limits which with the technological world are currently dealing. Alternative solutions are needed to improve and enhance our current devices. In this context, the integration of nanowires in the pre-existing devices such as FIN-FETs or GAA-FETs represents the new frontier of fabrication that aims to improve performances and scalability at the same time.

Here we study the electrical properties of single nanowires (NWs) devices and networks that comprise of them. We use Ag NWs, coated with a polyvinylpyrrolidone (PVP) passivation layer, as a platform material to study the electrical activation of nanowire networks (NWNs). Although the passivation layer is often considered as an obstacle to overcome, in this study we exploit its properties to increase the functionality of the device. The role of the junctions, or more precisely the metal insulator metal structures created between NWs, is crucial since it can facilitate the formation of a conductive filament (CF) which bridges the cores of the NWs modulating electrical conduction. Through experimental evidence and extensive simulation work, we propose a model that describes the formation of CFs within junctions thereby enabling conduction across NW films. Combining the results obtained from single wire devices and networks enables us to distinguish between two different conduction mechanisms, one based on a tunnelling effect and one related to ohmic conduction.

Measurements conducted on multiple single wire and network devices reveal that their conductance follows a power-law dependency with the charge passed through the NWs. On this basis, we introduce a universal scaling behaviour

in which networks and junctions follow the same scaling laws independent of their electrical properties (i.e. material type, coating layer, thickness of the layer). Exploiting this dynamical model we can obtain information about the activation of the system and its conductivity evolution as the current flows through it. In defining two scaling coefficients we can distinguish between the different types of activations. One, which occurs through an electrical percolating path defined as "Winner-Takes-All" paths (WTA) and one that instead evolves in a more homogenous way. Thanks to a voltage contrast technique it was possible to actually visualize the formation of the WTA path within the NWNs. Through further characterizations, we prove that by modulating the amount of current used to set the device we can access different conductance states or memory levels that have vastly different retention times. Moreover, simulations support experimental evidence that the WTA path represents the most efficient way for networks to transmit charge from one electrode to the other. Simulations also provide insights into network entropy that showed how the connectivity evolution proceeds in the network as the current is increased.

Studies on other NWs materials have confirmed the same scaling law found in Ag NWs and networks. Core-shell NWs are shown to be a very promising candidates for the realization of NW-based devices since they add a new degree of resistive switching control onto networks. Their unipolar and/or bipolar resistive switching behaviour along with the properties of the WTA paths described earlier are expected to have a large impact in many research fields such as memory devices and neuromorphic computing.

Acknowledgements

I would like to thank my supervisor Prof. John J. Boland for giving me the opportunity to proceed my studies within the Trinity College Dublin. This challenging chance enable me to pursue my research carrier and improve my skills within the scientific world. I would to thank Dr. Allen T. Bellew that was a wonderful guide during the first year of my PhD introducing me to the everyday challenges behind the project and the techniques needed for the device fabrication. I am very grateful to Hugh Manning for the precious help provided to me for the fabrication and electrical tests of devices.

I would also kindly thank my colleagues Dr. Shaun Mills, Dr. Curtis O'Kelly and Dr. Jessamyn Fairfield for the help and tips useful to address my project in the right direction and Mary McCarthy and Rachel Kavanagh for their precious work within the Boland research group.

A particular thank to our collaborators Dr. Claudia Gomes da Rocha and Colin O'Callaghan that are taking care of the modelling to support the experimental results within the Theory and Modelling group headed by Prof. Mauro Ferreira. A special thanks to Claudia for proofreading this manuscript. And finally a very grateful thank to my family that support me with love and patience during my studies.

Contents

List of figures

List of tables

List of abbreviations

AE	Active Electrode
AFM	Atomic Force Microscopy
BRS	Bipolar Resistive Swicthing
C-AFM	Conductive Atomic Force Microscopy
CBRAM	Conductive Bridge RAM
CE	Counter Electrode
CF	Conductive Filament
CG	Control Gate
Cmos	Complementary Metal Oxide Semiconducutor
CNT	Carbon Nano Tubes
CRS	Complementary Resistive Swicthing
CTAB	Cetrimonium Bromide
DRAM	Dinamic Random Access Memory
DUT	Device Under Test
EBL	Electron Beam Lithography
ECM	Electro Chemical Mechanism
EDX	Electron Diffraction X-ray
EMT	Effective Medium Theory
EPPs	Electrical Percolating Paths
FEG	Field Emission Gun
FET	Field Emission Transistor
FG	Floating Gate
FTO	F-doped Titanium Oxide
GAA-FET	Gate All Around Transistor
HRS	High Resistance State
I/O	Input Output
Icc	Current Compliance

IMFP	Inelastic Mean Free Path
IPA	Isopropanol
ITO	Indium Titanium Oxide
JDA	Junction dominated Assumption
JXN	Junction
LED	Light Emitter Diode
LiT	Lock-in Thermography Technique
LRS	Low Resistance State
MIM	Metal Insulator Metal
MMA	Methyl Methacrylate
MNR	Multi-Nodal Representation
MNWNs	Metallic Nanorire Networks
MOSFET	Metal Oxide Semiconductor Fet
NP	Nanoparticle
NW	Nanowire
NWN	Nanowire Network
PDMS	Polydimethylsiloxane
PEDOT:PSS	Poly(3,4-ethylenedioxythiophene) Polystyrene Sulfonate
PL	Power Law
PMC	Programmable Metallization Cell
PMMA	Poly Methyl Methacrylate
PPL	Post-Power Law
PVC	Passive Voltage Constrast
PVP	PolyVinylPyrrolidone
QCP	Quantum Conductance Point
QD	Quantum Dots
RERAM	Resistive Swicthing Random Access Memory
SE	Secondary Electron
SEM	Scanning Electron Microscopy
SMU	Source Measure Unit
SRAM	Static Random Access Memory

TC	Transparent Conductors
TCM	Thermo Chemical Mechanism
TEM	Transmission Electron Microscopy
TG	Transient Growth
URS	Unipolar resistive swicthing
UV	Ultra Violet
VCM	Valence Change Mechanism
VLS	Vapor Liquid Solid
WTA	Winner-Takes-All
1C1T	1 Capactior 1 Transistor

List of publications

Manning, Hugh G., Fabio Niosi, Claudia Gomes da Rocha, Allen T. Bellew, Colin O'Callaghan, Subhajit Biswas, Patrick F. Flowers, et al. 2018. "Emergence of Winner-Takes-All Connectivity Paths in Random Nanowire Networks." *Nature Communications* 9 (1).

O'Callaghan C, C G Rocha, F Niosi, H G Manning, J J Boland, and M S Ferreira. 2018. "Collective Capacitive and Memristive Responses in Random Nanowire Networks: Emergence of Critical Connectivity Pathways." *Journal of Applied Physics* 124: 152001.

Chapter 1

Introduction

The functioning world around us relies on knowledge and information. Languages have been developed to communicate and spread information using particular codes. For instance, the English language has 26 different characters used to refer to different words and concepts. Genetic code has 4 different chemical base groups, abbreviated by the characters A, T, C and G, that combined together to form DNA strands. A particular code, the Boolean type [1], is made of only 2 characters “0” and ”1” and is the simplest way to represent information. Its peculiarity lays in the fact that the information, called a bit, is the fundamental unit by which electronic devices store information. Since 1959, when Richard Feynman at an American Physical Society meeting held his talk “there is plenty of space at the bottom” [2], the scientific world has sought ways to optimize the density and quality of transferred information. The capability to store more information within a smaller volume, the writing/reading speed of bits in memory devices or the ability to minimize the power consumption represent some of the problems the miniaturization process must address. This technological evolution is summarized by Moore’s law (Fig 1.1) [3,4].

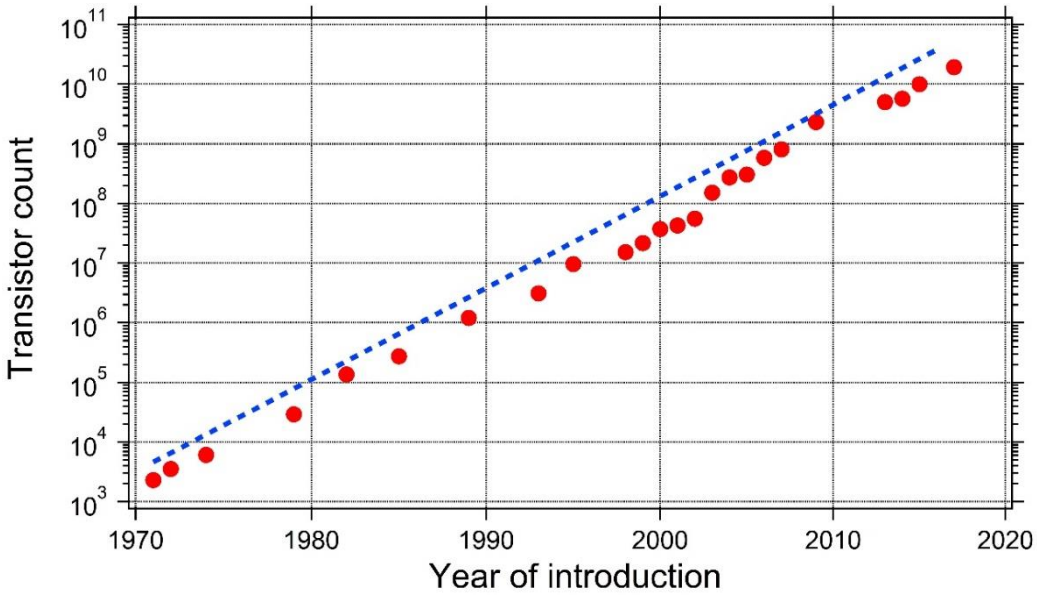

Fig. 1.1 Moore's law that describes the evolution of integrated circuit (IC) device densities over time [5]. The blue dashed line is an eye-guide that indicated the trend doubling the number of transistors per year.

In this law, Moore predicted that the number of transistors incorporated within a chip will approximately double every 2 years [4]. The first central processing unit (CPU) released by Intel in 1971 was capable to make simple I/O calculations. The fabrication process, back in time, was performed on a 2-inch wafer using a lithography technique [6].

Throughout the years, everyday devices such as transistors and integrated circuit allowed the development of more powerful CPUs that meet Moore's prediction. Nowadays devices have reached unimaginable sizes yielding device densities and capabilities comparable with the dimensions of single atoms. Considering, for example, the number of operations that a single CPU can do within a second. The 4004 model (1971) was capable of 92,000 instructions per second. After five decades, the latest version of supercomputers can manage almost $1\ exa\ (10^{18})$ instructions per second [7]. Closer inspection of Fig. 1.1, however reveals a departure from Moore's law. Initially, the high integration within chip was facilitated by the continuous improvements in the fabrication processes, in particular, the fabrication of increasingly smaller devices using improvements in

lithography. Table 1.1 summarizes the evolution that lithography had between the 70's and 80's with the relative resolution [8].

Table 1.1 Lithography evolution [8] with relative resolution achievable.

Semiconductor lithography technology transitions			
Technology generation	**First industry sale**	**Initial resolution (μm)**	**Market dominance**
Contact	1962	7.00	N/A
Proximity	1972	3.00	1973
Projection	1973	2.00	1977
E-beam	1976	0.5	Never
X-ray	1978	0.3	Never
G-line	1978	1.25	1982
I-line	1985	0.80	1991
DUV $248nm$ (deep UV)	1986	0.45	1998
DUV $193\ nm$	1996	0.15	2006
DUV $157\ nm$	1998	0.10	Never
DUV $193\ nm$ immersion	2005	0.04	2012
EUV $13.5\ nm$ (Extreme UV)	R&D	0.0135	R&D

For decades, research and development went side by side as can be seen from the table 1.1 but nowadays the semiconducting industry is facing the fact that lithography is reaching its limit to top the finite feature size. The latest generation of integrated circuit (IC) are now comparable with the dimensions of a few atoms. According to the semiconductor roadmap [9], the dimension of a single transistor in 2019 will be around $5 - 10\ nm$ corresponding roughly to $20 - 40$ atoms. This will inevitably cause problems such as reproducibility of the devices, leakage, increased production costs and increasingly sophisticated manufacturing technologies. There will be difficulties arising from the interaction and manipulation of single atoms to create devices. Devices such as FIN Field-Effect Transistor (Fin-FET) and multi-gate FET [10] aim to minimize these problems but yet, their manufacturing requires the ability to control and tune the materials at a single atom scale. For this reason, a change of device architecture is necessary. Recently many approaches have been proposed but the most promising candidate

that can allow the continuation of Moore's law is the memristor and its integration within the pre-existing device technologies [11]. To further enhance the capabilities of the next generation electronic devices, the integration of 3D features is now being considered. More complex structures such as Gate–All-Around (GAA-FET) or Multi-Gate nanowires (NWs) FET are being employed to improve the properties of transistors and IC using nanostructures. Fig. 1.2 shows a practical example in which a Si nanowire is used within a GAA MOSFET device to connect source and drain electrodes [12]. The Si nanowire, encapsulated within a Ge cover layer, plays a key role within the scaling process. It enables the integration of nanometre size objects bypassing the UV lithography step and its limitation along with it. The bottom-up approach used to create the GAA device grants the possibility to create structures with sub-10 nm features, something unachievable with conventional lithography techniques. The sharp interface between the Si NW and the Ge layer also improves the electrical performances as reported by a research group on IMEC technologies [12].

The memristor, as first introduced by Chua [13], is a two terminal device capable of changing its resistance according to the current or voltage stimulus, and it retains its resistance (memory) level even after the stimulus is removed. Thanks to its remarkable qualities, it can be potentially used as memory devices, computer logic or even for neuromorphic (brain-like) applications.

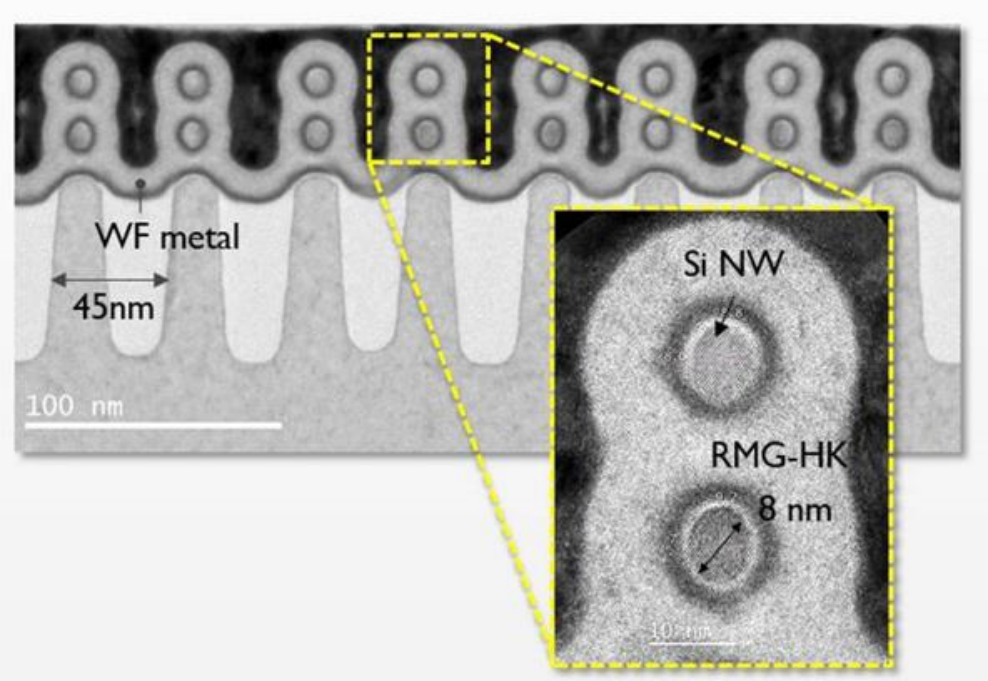

Fig. 1.2 GAA MOSFET device, one of the first semiconducting devices with a Si NW integrated into it [12]. The "Gate All Around" structure is clearly visible in the inset in which the Si NWs are embedded in the surrounding Ge layer.

For these reasons, it is worth considering the implementation of nanowires and memristor components as a completely new paradigm for device operation. Here, following, a comprehensive introduction on memristor and Resistive Random-Access-Memory ReRAM capabilities we describe how nanowire networks (NWNs) may represent the new paradigm needed to maintain Moore's law level performance.

1.2 Memristor devices

The term memristor, was introduced by Chua in 1971 [13]. According to his pioneering work, a memristor is a nonlinear two terminal circuit element in which the resistance depends on the charge q flowing through the device [14,15]. A memristor can in principle work as a memory device with associated non-volatility properties. Earliest reports based on memristor operation are dated within the 60's. Hickmott in 1962 [16], for example reported a large negative resistance when

contacts were established to different insulating oxide layers such as NiO_x, SiO_x, TiO_2, and Al_2O_3. The interest in Chua's work has grown rapidly since HP reported a memristor effect [17] in a confined TiO_2 Metal-Insulator-Metal (MIM) nanodevice. The interest in memristor devices, as shown in Fig.1.3, has grown abruptly in the last years thanks to their potential in electronic applications.

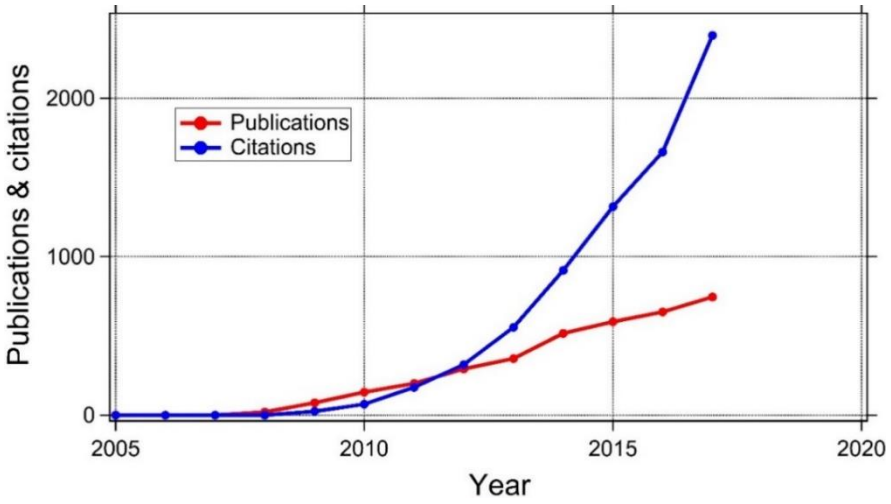

Fig. 1.3 Number of publications (in red) and citations (in blue) referring to memristor devices. Data acquired from https://www.scopus.com using as keyword "Memristor device".

Memristor devices can have different operational modes depending on the structure and the characteristic of the insulating layer used [18]. In order to describe a memristor device, it is opportune to introduce the notation that will be used throughout this thesis. A memristor can exhibit different characteristic resistance states known as High Resistance State (HRS) and Low Resistance State (LRS). The HRS is commonly associated with the OFF (or "0") state of the device while the LRS corresponds to the ON (or "1") state. The operations by which a device can be switched between the two states are known as SET (write) and RESET (erase). In both the operations, a voltage is applied to the device to change the resistance from the HRS to the LRS in the write (SET) operation or from the LRS to the HRS in the erase (RESET) operation. The switching properties of devices can be classified as: unipolar (URS), bipolar (BRS) and complementary resistive switching (CRS) device [19].

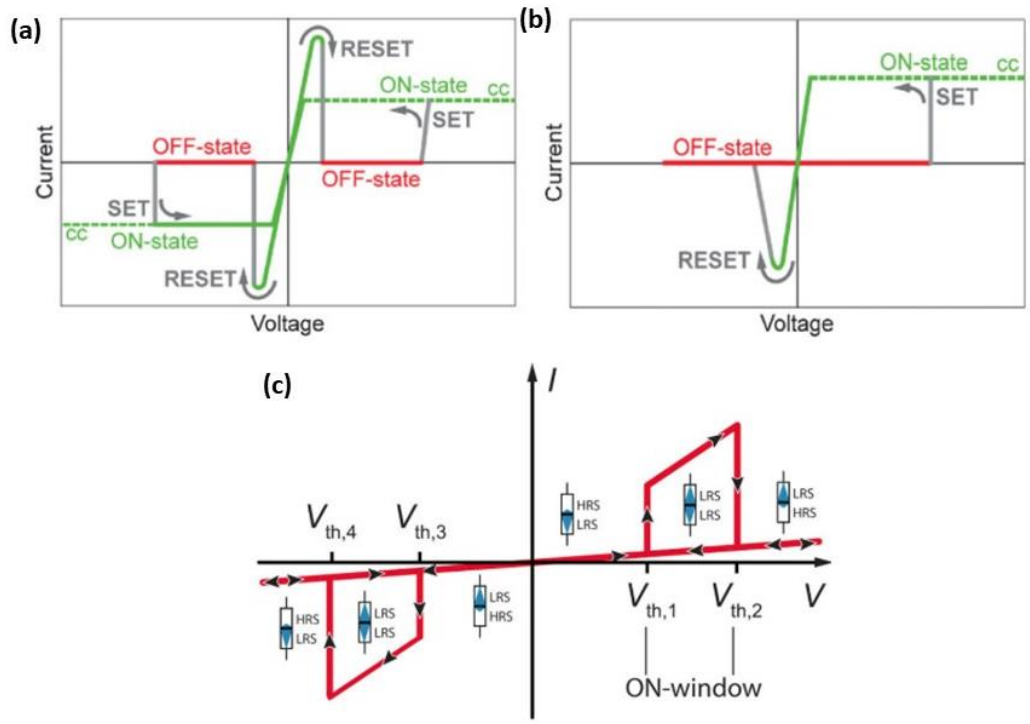

Fig. 1.4 Typical I-V curves for unipolar (a), bipolar (b) and complementary resistive switching (c) devices [20,21]. In unipolar devices set and reset operations are obtained applying one voltage polarity while in the bipolar configuration to two different voltage polarities are required to set/reset the cell. In the latter case, the complementary resistive switching, both the mechanism described for uni/bipolar devices are present.

In a unipolar device, the two operations, SET and RESET, can be executed using the same voltage polarity as shown in Fig. 1.4 (a). The system starts at its pristine HRS and a voltage in the positive direction is used to SET the device. A current compliance I_{cc} is initially set to prevent electrical failure of the sample during the SET operation. Once the sample is in the LRS, the second positive sweep is applied without any compliance causing the RESET of the device due to the high current flowing within the device [20].

A bipolar switching process is associated with the fact that SET/RESET happen using two different voltage polarities. Fig. 1.4 (b) shows how, with the application of a positive bias, the device goes from the HRS to the LRS. A current compliance is used even in this case in order to prevent electrical damage to the device.

A negative voltage is then applied to the sample to restore the initial conditions with the device passing from the LRS to the HRS.

The complementary resistive switching (CRS) is a more complex process and, as suggested by Linn et al [20], can be built using two bipolar resistive switches in a back-to-back manner. Due to this particular configuration, CRS is widely used within crossbar arrays to eliminate the leakage currents through the adjacent bars that otherwise degrades very easily the qualities of the devices. The reading operation for CRS requires higher voltages (few V) compared to URS and BRS (hundreds mV) eliminating the problem that sufficiently low voltages often cause leakage currents.

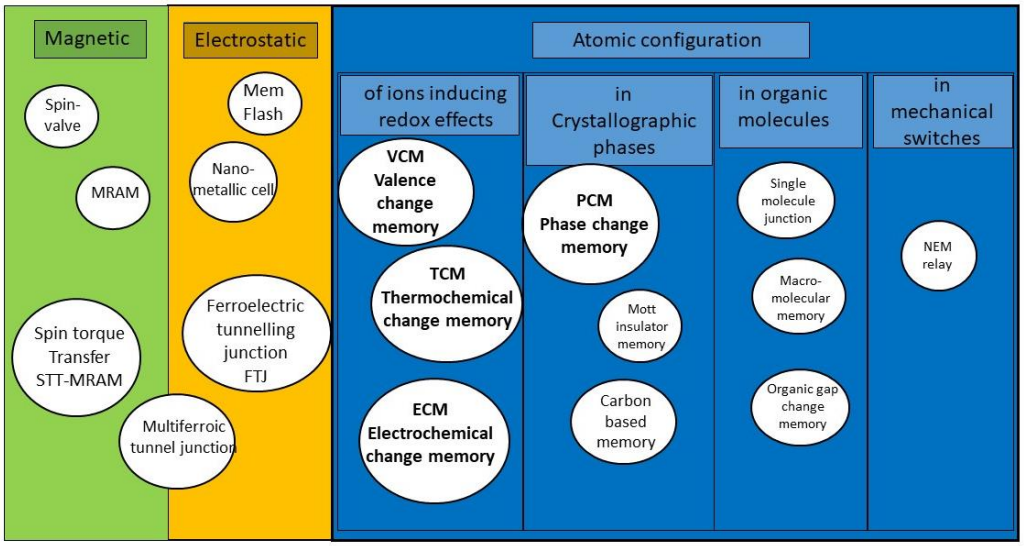

Fig. 1.5 Overview on memristor phenomena based on the different mechanisms [9]. Despite the vastness of this research field across this PhD project we will describe the characteristics of the devices based on redox reactions with particular attention to the redox effect materials.

A second important distinction, shown in Fig. 1.5, is on the basis of the mechanism that drives the memristor behavior within the device. Among the different categories, particular attention will be focused on devices regulated by the redox reactions effects. The high electrical fields applied to nanoscale device induces the motion of ions within the insulating layer leading to internal reduction-oxidation processes that control the overall resistance level. Memristor devices whose operation depend on a Redox-based ReRAM will be further discussed in section 1.2.2.

1.2.1 Memory devices

Memory devices appear in a wide range of modern electronic devices including smartphones, TV screens, personal computers, etc. Memory is classified as volatile or non-volatile. As suggested by the name, volatile memory devices are capable of storing information as long as voltage is supplied. Shutting off the power will cause the loss of any saved data. Dynamic Ram (DRAM) and Static RAM (SRAM) are two of the most common examples of volatile memory on the market. The working principle of DRAM's is quite simple. The charge stored on a capacitor acts as switch between the OFF state or "0" and the ON state ("1"). A transistor is coupled to the capacitor allowing the READ operation without perturbing the state itself. The combination of the capacitor as a storage unit and transistor as the reading counterpart is known as a 1C-1T technology and is capable of recording a single bit of information. This simple unit 1C-1T is then embedded within arrays to create the memory device.

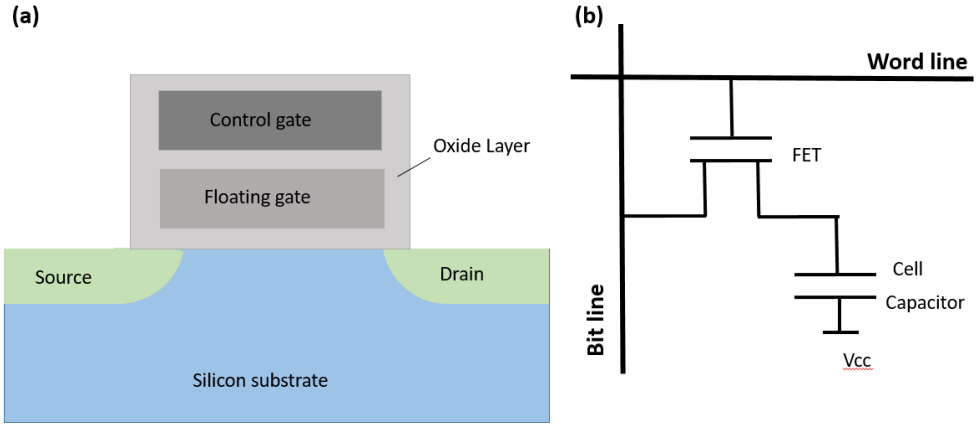

Fig. 1.6 A floating gate memory device (a) and its schematic (b), readapted from [22].

Nonvolatile devices retain the stored information even when the power is removed. In contrast to volatile memory, this kind of memory provides lower performances in terms of reading information, worse endurance and most important the cost to store information is higher. Nonvolatile memories are often

used as long-term storage of information, most common devices are hard disk drives, read-only–memory and flash memory. The latter is now the dominant type and is used in almost all electronic equipment. Fig. 1.6 (a) schematizes the structure of the device that resembles common MOSFET [22]. A floating gate (FG) electrically isolated from the rest of the device, is positioned between the control gate and the source-drain channel and basically acts as a switch. The charges accumulating on the FG cause a screening effect affecting the control gate (CG) leading to the logic states “0” and “1”. State “1” can be obtained removing the charges from the FG by the application of a voltage or UV light. The logic states are governed by the current that flow between the source and drain; if the channel is conducting, it means that the FG is not charged resulting in the logic state “1”. Otherwise, a “0” is obtained when the current cannot flow within the device. [22,23]. Therefore, flash memories are arranged in arrays and matrix to create components within electronic devices.

In the next section the two memory devices introduced, DRAM’s (volatile) and flash (nonvolatile), will be used to make a comparison in terms of performances, endurance, and longevity with ReRAM that represents next generation of nonvolatile memories.

1.2.2 RERAM devices

Conventional memory devices have to respect certain specifications in order to satisfy the market requirements. Ideally, the target for companies producing ICs is to produce faster, smarter, cheaper, and energy-efficient devices. The fabrication process has to be simple and scalable for mass production with the capability to implement 3D features if required. Table 1.2 summarizes the most important characteristic required for memory applications making also a comparison between DRAM, ReRAM and flash memories.

Table 1.2 Performances comparison between conventional memory devices and ReRams [22]. The F parameter used in the table is related to the current resolution of the UV lithography technique used.

	DRAM	**Flash**	**ReRAM**
Cell size	≈8F^2	5.44F^2	4.28F^2
Endurance	>10^{15}	>10^5	>10^8
Retention time	>64ms	1-3 years	>10years
Volatility	y	n	Y
Resistance ratio	-	5	10-1000
Read voltage	-	0.6V	0.3-0.7V
Multilevel storage	n	y	y
Energy per bit(J/bit)	4x10^{-15}	4x10^{-16}	>10^{-12}
Writing speed	<10ns	200µs	100ps

For decades the scalability of devices was linked to the technique resolution used for fabrication but as introduced earlier, this is no longer the case. As reported in Table 1.1, UV Lithography has reached its physical limitation (see Chapter 2), therefore, a new way of device fabrication is required. DRAM and flash memories have a limited resolution of $15\ nm$ while ReRAM exhibits higher scalability. Switching between the ON-OFF states has already been demonstrated in $10\ nm\ x\ 10\ nm$ devices [24]. Further increases in resolution are achievable since the conduction mechanism within ReRAM is driven by ions within the insulating layer of MIM cells. Thanks to this, devices could in principle be much smaller than $10\ nm$ [25]. The stackability of this kind of cells provides a way to re-think devices in a 3D fashion allowing the integration of multiple MIM structures. Besides that, the power consumption and reading/writing process will be substantially improved due to the more highly confined structures. The reduction in space allows for decreased read/write voltages, reducing the total power consumption [26]. Compared to flash memories substantial improvement of few orders of magnitude in writing speed are anticipated. This is achievable thanks to the nanoscale separation distance between electrodes. Besides, the high electric fields and

temperature, generated by Joule heating, (current density equal to $10^5\ A/cm^2$ has been demonstrated for a $10\ nm\ x\ 10\ nm$ device) help the carriers to diffuse faster within the insulating layer. Parameters such as endurance and retention time are on the other hand extremely dependent on the type of ReRAM used. The endurance, expressed as the number of cycles that a device can handle, can vary over a large window, almost six orders of magnitude (10^6 - 10^{12} for TaO_x devices) [1,22,27,28], depending on the composition of the insulating stack material. Retention time, on the other side, is the capability to store and preserve the information over time. In order to simulate the real conditions within hard drives the retention time is often calculated under thermal stress. In a conventional flash device, retention time is estimated to be between 1-3 years. For ReRAM, independent of the material used for devices, the information can be stored for longer periods [29]. This is possible thanks to the high resistance ratio, defined as R_{HRS}/R_{LRS}, associated to ReRAMs. Table 1.2 highlights the poor resistance ratio of flash memories in comparison to ReRAMs. Generally, higher resistance windows allows greater accuracy during the reading operation thanks to a wider operating margin.

1.3 Switching mechanism

Depending on the nature of the switching mechanism, it is possible to make further distinctions between ReRAMs. The behaviour of MIM cells is often related to the insulating material that is also known as active layer. A brief explanation of three switching mechanisms is presented in the following section. This will shed some light on the rich conduction mechanism that ReRAM devices can manifest.

Electro Chemical Mechanism (ECM)

The ECM effect is also a bipolar effect and it is known in the literature as Conductive Bridge RAM (CBRAM) or programmable metallization cell (PMC) [30]. As the name might suggest, a redox reaction happens at the active electrode (AE) resulting in the formation of a conductive filament within the device [30] as shown in Fig. 1.7 (a).

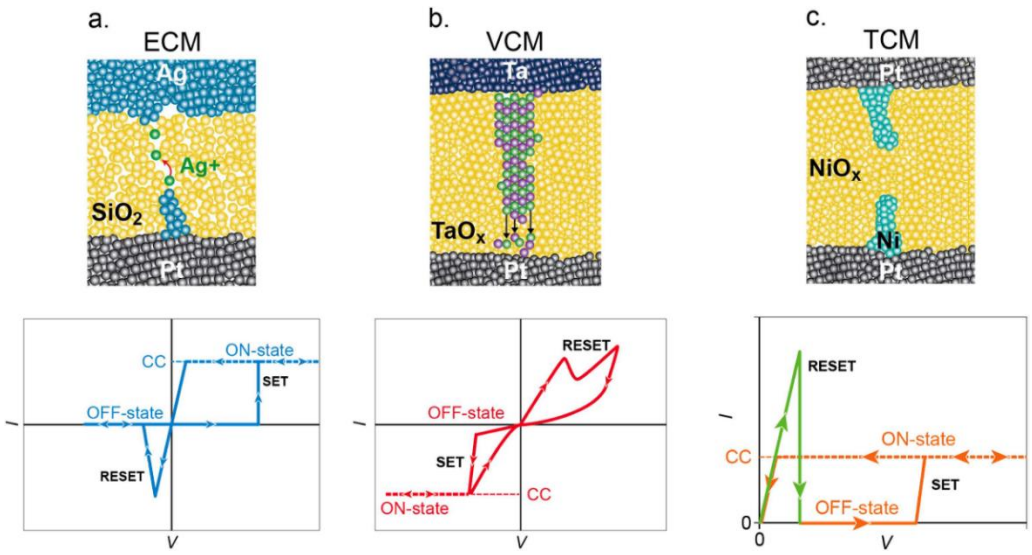

Fig. 1.7 Different mechanisms for the creation of a conductive filament within MIM devices captured in I-V curves [31].

The choice of the electrode material in the case of ECM is crucial; materials with high mobility such Ag, Cu or Au are commonly used as the active electrode. Their high electrochemical activity facilitates the reactions and therefore the creation of the CF. On the other side, inert materials such as W, Pt, and Ni are used as the counter electrode (CE). The role of the CE is to catalyse or to inhibit the redox reaction and therefore the CF formation. Cells performances are also heavily influenced by the AE/CE coupling in terms of energy requirements for the reactions (see Fig. 1.8). The easiest way to investigate this phenomenon is to perform cyclic voltammetry over cells made of different materials. As suggested by Tsuruoka et al [32], cyclic voltammetry measurements help to identify and prove that these processes are driven by redox reactions. In Fig. 1.8, several MIM cells

are tested applying low voltages to prevent the switching between the ON and OFF states. On the left hand side, the curves for cells made with Cu as AE, SiO_2 as the insulating layer and different CEs [32] are shown. In Fig. 1.8 (b), the same type of investigation is performed over a Cu/Ta_2O_5/Pt cell [32] and shows the different electrochemical reactions happening within the device.

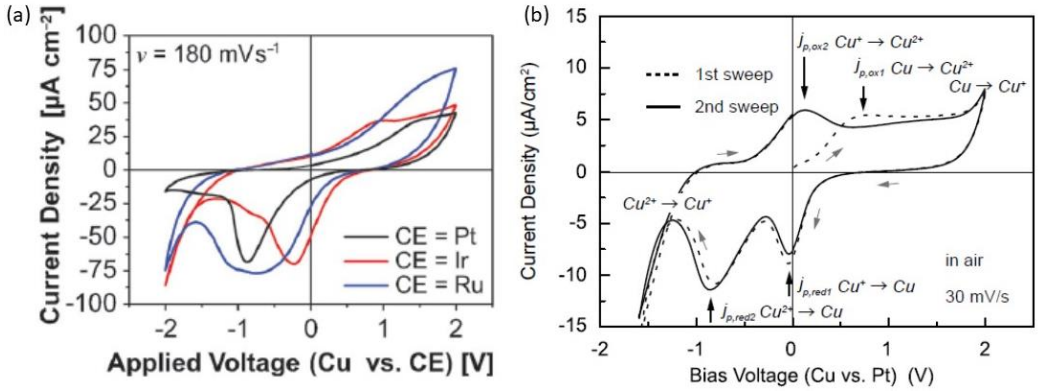

Fig. 1.8 Cyclic voltammograms measurements performed on different MIM devices. The voltage applied is deliberately chosen to prevent the switch within the cells [31,33]. In (a) the AE is always Cu while the CE is changed in order to test the importance of the CE material. A different active layer is instead used in (b). A Cu/Ta_2O_5/Pt cell is used to highlight the redox peaks. A comparison in terms of current within cells (two black curves in a-b) shows the role that the active layer plays within cells.

A typical voltammetry measurement is reported in Fig. 1.8. This electroanalytical method is commonly used to understand which redox reactions take place within MIM devices formed by different materials. A subthreshold voltage is swept in both polarities and, as can be seen from Fig. 1.8, several redox peaks are observed in the voltammograms plots for different AE/CE combinations.

Valence Change Mechanism (VCM)

This effect occurs within a wide range of metal oxide materials and is due to the migration of ions between the electrodes. In the case of oxide dielectrics, properly choosing the electrodes materials, oxygen vacancies are responsible for the creation of a conductive filament (CF) that spans between the electrodes, lowering

the overall resistance of the cell [34]. Different reports point out that even interstitial cations acting as mobile donors might be responsible for this conduction mechanism too. The motion of ions will induce a change in stoichiometry causing redox reactions [21]. Bipolar memory behaviour is typical of VCM devices and can be seen in Fig. 1.7 (b). Many reports correlate the switching effect to electrical pulses applied to the cell where the polarity of the voltage applied induces reduction or oxidation.

Thermo Chemical Mechanism (TCM)

This mechanism is slightly different from the first two. The main difference lies in the unipolar behaviour that this kind of devices shows. From Fig. 1.7 (c) it is possible to note how TCM can be switched between ON and OFF states using the same voltage polarity [35]. The operation to set the device usually involves the use of a current compliance I_{cc} to limit the maximum current flowing within the device to prevent electrical breakdowns. Furthermore, the heat generated by Joule effect induces redox reactions that change the stoichiometry of the cell allowing the formation of a CF. Reset operations are instead obtained by removing I_{cc}. The high current (mA range) that flows within cell can produce temperature gradients that eventually disrupt the CF growth and return the cell back to the OFF state. Due to its working principle, TCM is also known as fuse-antifuse memory. Because of the high currents and energies required for switching, TCM R&D decreased significantly in the past 5 years.

1.4 Conductive filament formation

Despite the different mechanisms, VCM, ECM and TCM have a feature in common which is the possibility of generating a conductive filament from redox reactions. The interest in describing this phenomenon has grown rapidly. Several studies have been published using both experimental [33,36] and computational [37]

approaches. Designed tests were performed over a wide variety of MIM cells to confirm that the switching mechanism is governed by the same CF growth process.

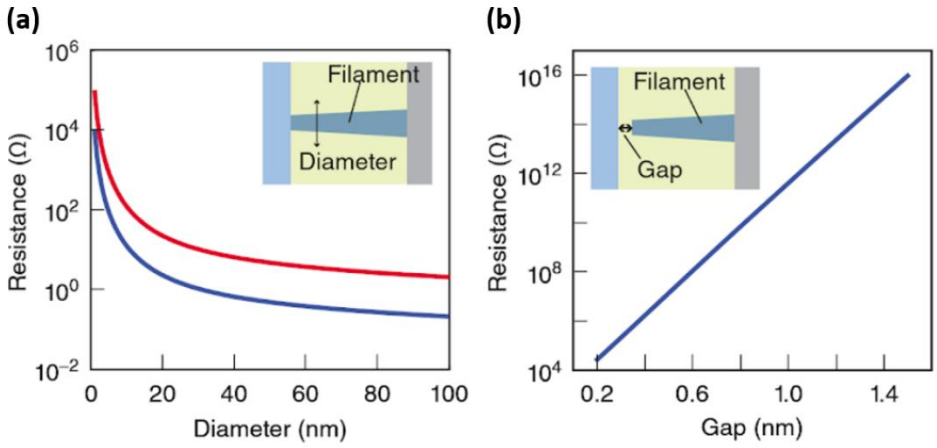

Fig. 1.9 Resistance vs diameter of a CF simulated with the variable diameter model [38] in (a). The resistivity used for the simulations are respectively $400 \mu\Omega\ cm$ for a Hf filament in red and $200\ \mu\Omega\ cm$ for Cu in blue [39]. In (b) the variation of the resistance as the gap decreases.

Fig. 1.9 shows the results obtained from two different simulation models used to describe the formation process of a CF. In the first model, the resistance is calculated considering the formation of a CF, with a variable diameter, that connects the electrodes. In the second scenario, the filament initially does not connect the electrodes and therefore tunnelling effect is considered responsible for the conduction within cells. Note that due to the wide variety of materials and CF growth mechanisms, particular devices might be described by a combination of the two models [38].

Two models were introduced initially to describe bipolar switching within MIM cells. Variable diameter model is based on the migration of localized defects which, under a certain bias, leads to the formation of a CF [38]. An inverse potential will reverse the process causing the dissolution of the filament, resetting the device. The process can be simply described using an Arrhenius-type approach as:

$$\frac{d\phi}{dt} = A\ exp\left(-\frac{E_A}{K_B T}\right) \qquad \text{Eq. (1.1)}$$

where $d\phi/dt$ represents the variation of the CF diameter, E_A is the activation energy for defect migration, A is a pre-exponential constant while K_B and T are respectively the Boltzmann constant and the local temperature.

Considering then Poole-Frenkel transport mechanism, as suggested by [37,40], the activation energy can be rewritten as a function of the applied voltage as

$$E_A = E_{A0} - \alpha eV \qquad \text{Eq. (1.2)}$$

Where E_{A0} is the energy barrier without voltage applied, α is a constant related to the hopping coefficient and V is the voltage across the device. In this picture, the diameter and consequently the CF growth will be only dependent on the bias applied to the ReRAM cell, indicating a voltage-driven process.

Fig. 1.10 depicts the CF evolution during a voltage dual sweep ($0V \rightarrow 1V \rightarrow -1V \rightarrow 0V$) performed on a $20\ nm$ thick HFO_x cell that shows bipolar (setting a I_{cc}) and complementary switching behaviour [38]. A positive voltage is applied initially to the cell (state 1) causing the accumulation of defects close to the positive electrode. Further increase in voltage will help the formation of the CF in state 2. Once the polarity of the voltage is changed, the defects migrate to the CE resetting the device (state 3). The cycle is repeated with the opposite polarity of the voltage. The conduction states in which the CF is not completely formed (1-3-5) yield resistances significantly higher (OFF states) as can be seen from the current-voltage (I-V) curve.

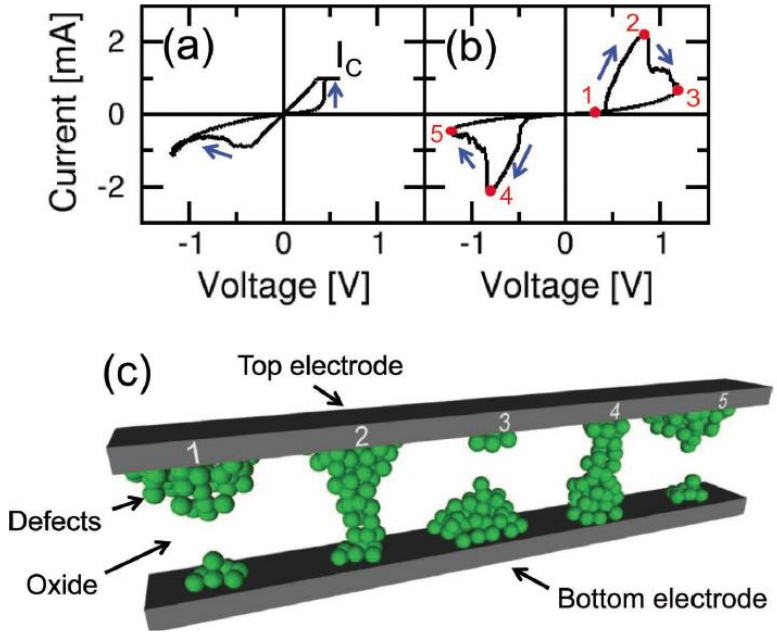

Fig. 1.10 I-V sweeps performed on HfO_x cell showing the formation of the conductive filament [38]. At the start the cell is in its virgin state and is activated through a voltage sweep as shown in (a) reaching the current compliance $I_c = 1\ mA$. The following evolution of the cell is shown in (b) with a relative cartoon of each configuration describing the state of the device in (c).

In the variable-gap model [41], the conduction can be virtually divided in two different contributions. The first contribution, that follows Ohm's law, is due to the conduction within the CF. A second part, inversely proportional to the voltage applied to the cell, is considered to account for the tunnelling effect. The two contributions can be described as a parallel circuit where the ionic current is due to the CF and the electronic current is associated to tunnelling effect as depicted in Fig. 1.11 (a).

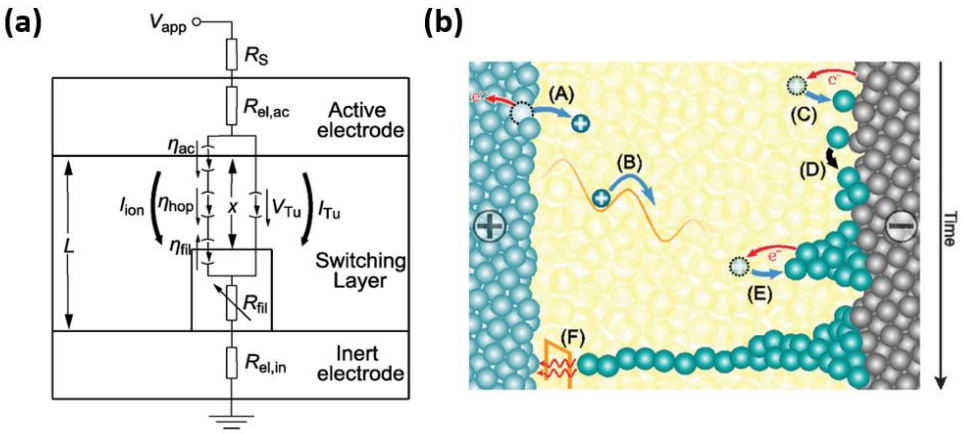

Fig. 1.11 Schematic of the equivalent circuit for the switching process (a). In (b) a sketch that describes electrochemical processes occurring during the SET operation [41].

Fig. 1.11 (b) depicts all the mechanisms responsible for the growth of a CF [41]. A positive voltage is applied to the active electrode AE (Ag/Cu) while the counter electrode CE (Pt) is grounded. Initially, the potential will favour the oxidation through charge-transfer reaction of Ag atoms (A). Ions are then migrating to the CE where the reduction reaction occurs (B-C). The accumulation of ions, by nucleation, will enable the formation of the filament that, under the effect of the potential, grows toward the AE (D-F). In the model, the CF is approximated as a cylinder with a cross section A_{fil} and length d, respectively while, the thickness of the insulating material is defined as L. As described earlier, the conduction is due to two different mechanisms indirectly related each other. In its virgin state, the device presents very high resistances, on the order of Gigaohms. As long as the filament keeps growing within the insulating layer, a reduction in resistance can be observed. The ohmic contribution on the total current will increase while the tunnelling gap decreases accordingly, lowering the overall resistance of the device. This trend is well summarized in Fig. 1.12 where the cell resistance is related directly to the CF radius [42].

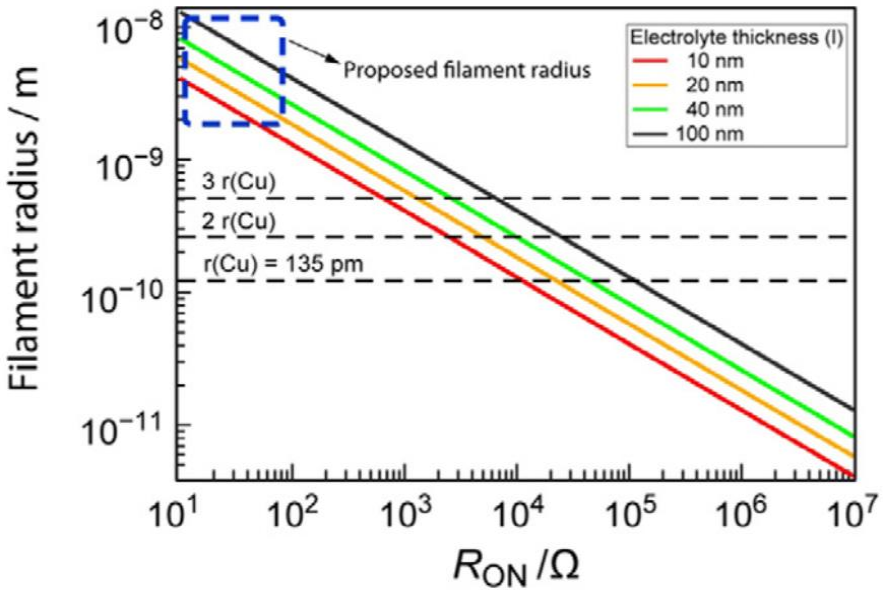

Fig. 1.12 Simulation that relates the R_{ON} (Ω) to the radius of the conductive filament growing within the cell as the thickness changes [42]. The horizontal lines represent the diameter of filaments ending with one two or three atoms that intercepting the curves give the R_{ON} values.

1.5 1D materials-nanowires

Materials that present at least one dimension smaller than $100\,nm$ can be classified as nanomaterials. Quantum dots or nanoparticles, for example, are considered as $0D$ materials, nanowires and nanotubes are $1D$ structures, and nanosheets and nanoflakes are examples of $2D$ confinement where only the thickness of the material falls within the nanometre range. The different physical properties of these novel materials have been ascribed to their structural characteristics. The exceptional electronic, mechanical, optical and magnetic properties of nanoscale materials can potentially revolutionise a wide range of technologies. As shown in Fig. 1.13, the interest in nanomaterials research has grown rapidly from the 90's onward. The development of electron microscope (see section 2.1.1) and tailoring of materials properties by quantum confinement effects are just two examples of the innovation that enable scientists to realise the era of nanotechnology.

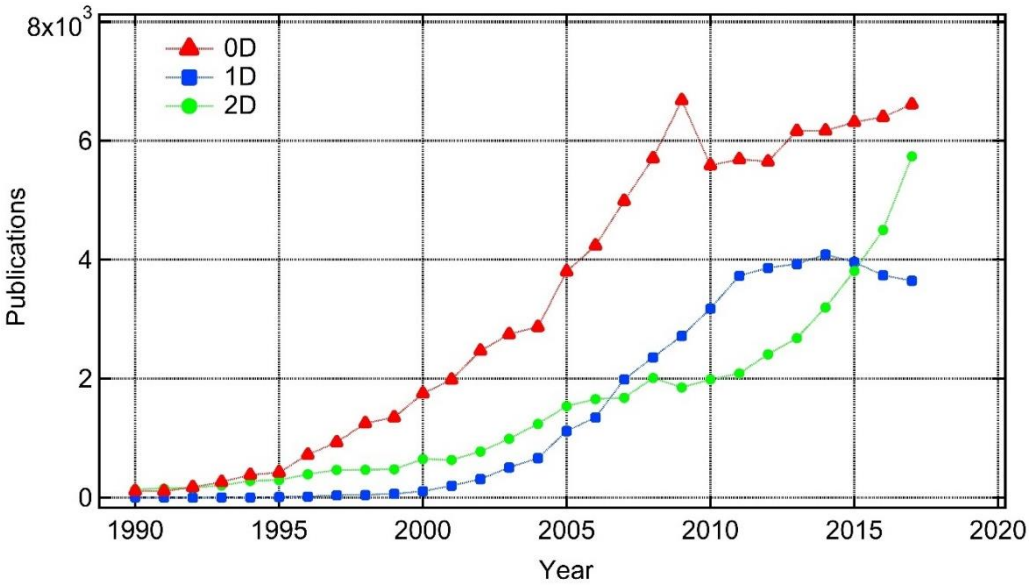

Fig. 1.13 Literature review that describes the number of publications of different nanoscale materials over the time. Data acquired from www.scopus.com using as keyword respectively 0D, 1D and 2D materials.

Fig. 1.13 summarizes the number of publications related to nanomaterials of distinct dimensionality [43]. $0D$ materials, in particular quantum dots (QDs) and nanoparticles (NPs), attract more interest thanks to their incredible surface area and catalytic properties [44]. Surface area is commonly described as the ratio between the atoms laying on the surface of a certain material respect to the bulk ones. The kinetics of reactions is deeply influenced by surface area because a bigger surface area also means that more atoms can undergo the reaction process. For this reason, nanoparticles and quantum dots are extensively studied nowadays in medicine, environmental applications, electronics, LEDs, batteries [45,46]. Recently, there has been a growing interest in $2D$ materials. Graphene is perhaps the most famous example with countless applications [47,48]. Made of a single sheet of carbon atoms, with a thickness of $0.345\ nm$, it provides outstanding mechanical and electrical properties. The main disadvantage is its poor integrability with 3D structures that has unfortunately impedes its device integration. The increasing interest in $2D$ structures have limited the research related to $1D$ material. Despite this, $1D$ materials still provide advantages in terms of aspect ratio, flexibility and robustness at the same time [43]. Besides, quantum

confinement effects provide new electronic properties to $1D$ structures opening a window on new conduction mechanism such as tunnelling and ballistic transport [49]. Mechanical properties of nanotubes and nanofibers have been widely studied because of tensile strength of these materials [50]. Scientists have recently produced peptides nanotubes with a Young's modulus of $19\ GPa$ that could be potentially even bio-compatible [50]. Core-shell and tubular nanowires have been studied for their thermoelectric efficiency [51,52]. Carbon nanotubes, thanks to their unique crystal structures, present remarkable electrical and mechanical qualities [53,54]. Catalysis and sensors are the major applications for the metal oxide and semiconductor $1D$ materials [55]. Yet another possibility is to assemble $1D$ nanomaterials into random oriented nanowire networks. This provide a natural transition between $1D$ and $2D$ materials since networks still present properties of $1D$ material but are incorporated into films with $2D$ characteristics. Therefore, the goal of this work is to study the electrical properties of metallic nanowire networks. The following sections describes the current state of the art of 1D nanomaterials with particular attention to their integration as networks within devices.

1.5.1 Transparent Conductors

Metallic nanowire networks (MNWNs) are often mentioned along with transparent conductors (TCs). Thanks to their excellent electrical and optical properties, they appear as ideal candidates for the next generation of touch screens, touch pads, and ultra-thin screens. State of the art touch screen technologies are built using layers of Indium Tin Oxide (ITO) or Fluorine-doped Tin Oxide (FTO) [56]. As a result, the price of raw indium material has rapidly increased in the last few decades [56]. Doped binary compounds such Aluminium Zinc Oxide has been proposed as alternative materials but unfortunately their electrical and optical properties are not comparable to ITO layers. Ideally, as shown in Fig. 1.14, materials should present high transparency and low sheet resistance. The first parameter is very important in order to maintain high levels of brightness within

devices and according to the market standards, the transparency should be higher than 90%. On the other hand, sheet resistance is crucial in lowering the energy requirement of the devices. Sheet resistance is expressed as $\Omega/\square$ and represents the resistance associated with a $2D$ layer or thin film of the material. Even in this case, according to the standards, ideal materials should have sheet resistance lower then $100\ \Omega/\square$. In Fig. 1.14, the transmittance is plotted against the sheet resistance for TCs fabricated using different nanomaterial. Focusing the attention on Fig. 1.14, currently researcher goal is to obtain films with transparency over $90\ \%$ with a sheet resistance lower then $100\ \Omega/\square$. In doing this, the performances of the actual devices will be hugely boosted granting high brightness and a low power dissipation.

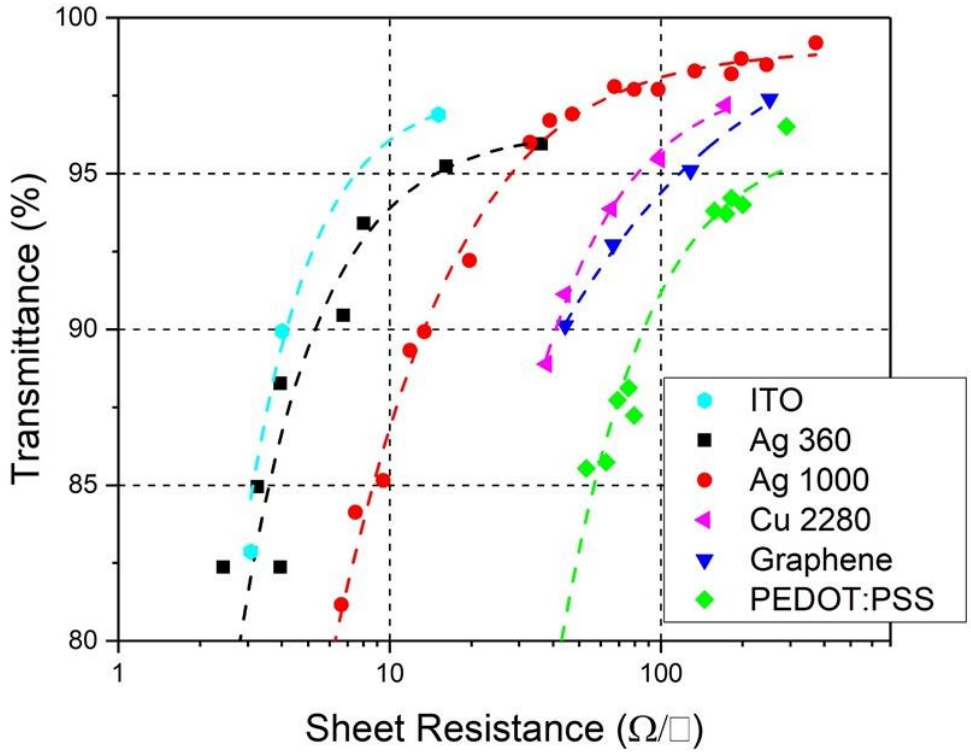

Fig. 1.14 Transparency vs Sheet resistance for different nanomaterials [57,58]. ITO films are currently used in devices but the properties of Ag NW networks are starting to be similar to the ITO films. A parameter that influences the outcome, especially in terms of R_S, is the aspect ratio expressed as $length\ /diameter$ of the NWs. Remarkably the Ag NW network with an aspect ratio equal to 360 (black squares) has a resistance that almost match the properties of ITO.

As can be seen, carbon based materials such as graphene or synthetic materials are not adequate due to their high resistances. The contact point resistance between nanotubes or flakes ranges from $50\ k\Omega$ to $100\ k\Omega$ as reported by [59]. The implementations of carbon based materials are therefore limited since homogenous films can present resistance in the order of magnitude of Gigaohms. On the other hand, metallic nanowire networks might be suitable for the purpose. As depicted by Fig. 1.14, the properties of Ag random oriented networks are close enough to match the standards of ITO films currently used as commercial devices. Ag nanowires are particularly attractive due to their low resistivity compared to Cu nanowires. Furthermore, another factor that needs to be considered is the aspect ratio of the NWs used that plays a massive role in the properties of the final device. Moreover, as will be further discussed in section 3.2.1, the quality of the films are hugely influenced by the contact point resistance or junction formed between two touching nanowires [60]. For this reason, numerous reports are focused at reducing the sheet resistance by minimizing the junction resistances. Thermal annealing [61], mechanical pressing [62], chemical etching [63] and laser welding [64,65] are examples, shown in Fig. 1.15, of techniques used to improve the quality of the devices in order to meet industry performance standards.

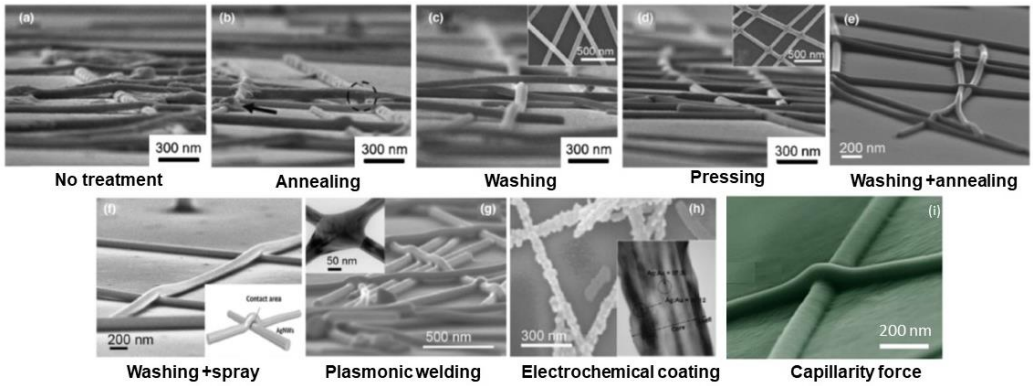

Fig. 1.15 Two different approaches are mainly used to reduce the junction resistance of NWs. The first is about physical treatment such as annealing or pressing of the films or alternately chemical treatments as shown in (h) [63,66].

With the constant market demand for flexible touch screens, another remarkable quality of MNWs is their mechanical properties. Thanks to the fact that nanomaterials can be dispersed practically within any solvent, they can be deposited very easily over any kind of surface including flexible ones [67,68], and the natural elasticity of the nanowire opens up the possibility of flexible devices.

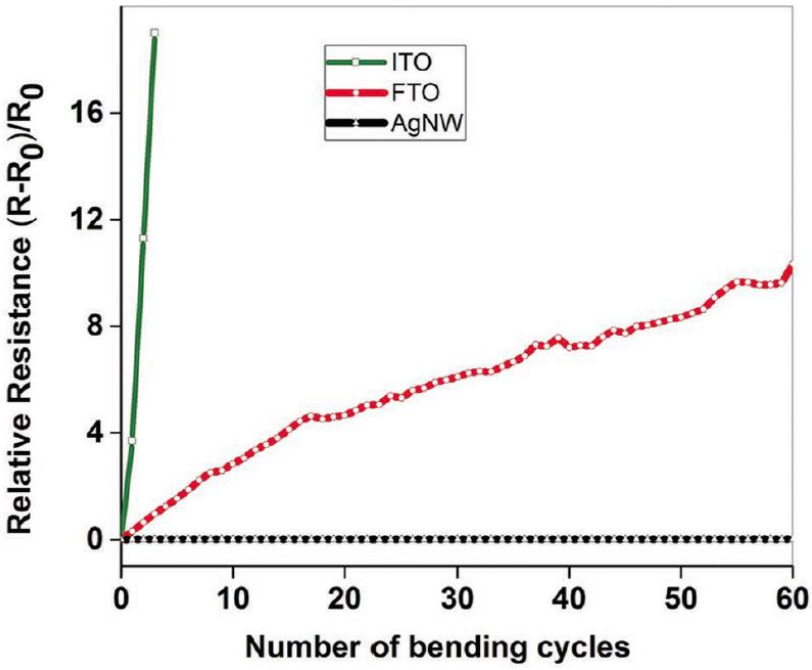

Fig. 1.16 Change in resistance of different materials, used as TCs, after several bending cycles [67,69]. In red the resistance ratio associated to an ITO film that degrades very quickly as the sample is bent. The FTO film shows instead a more smoothen degradation in comparison with ITO. The elasticity of the Ag NWNs is confirmed with an unchanged resistance after several bending cycles.

Studies on the mechanical properties with networks sprayed over flexible substrates have revealed incredible stretching abilities. Ag NW networks deposited over on Polydimethylsiloxane (PDMS) substrates can handle repeated bending cycles without any degradation in resistance [67,69]. The comparison between ITO, FTO and Ag NWNs shown in Fig. 1.16 demonstrates how the resistance for metallic nanowires does not change after mechanical stress [67,69]. Furthermore, the two conventional materials used nowadays for TCs highlight a

slow degradation of the film after several bending cycles (FTO) or an abrupt rupture after few cycles (ITO). This indicates that ITO and FTO are not suitable for realizing flexible devices. The remarkable characteristics of metallic nanowire networks, mechanical flexibility, high transparency and low sheet resistances, make them ideal candidates for transparent conductor applications. When combined with the ease of processing and scalability, MNWNs can play an important role into the new market of flexible devices.

1.5.2 Nanowire based memory devices

Several reports have highlighted the possibility to use nanowire-based devices for memory applications [70–72]. These studies cover a wide range of materials including oxide nanomaterials, core-shell structure and metallic nanowires. One of the first reports pointing in this direction was published by Kim et al in 2008 [73]. In their work, a NiO nanowire, shown in Fig. 1.17 (a), were contacted using Ti/Au electrodes. An electroforming step at $2.5\,V$, prior to the electrical tests, were performed for the set operation. Subsequent I-V's, shown in Fig. 1.17 (b), were used to prove the unipolar characteristics of the device. It is important to remark that the conditions to set and reset the devices are highly dependent on the geometry and the composition of the active layer. For this particular sample, the reset operation occurs for a reset voltage of $V_{reset} = 0.52\,V$ and a current of $I_{reset} = 230\,\mu A$. The LRS therefore presents a resistance value of approximately $R_{LRS} = 1.62\,k\Omega$. During the second I-V (red curve), the cell is initially in the HRS with a resistance value of $R_{HRS} = 1.38\,M\Omega$ giving a resistance ratio of $R_{ratio} = 8.5 \cdot 10^2$.

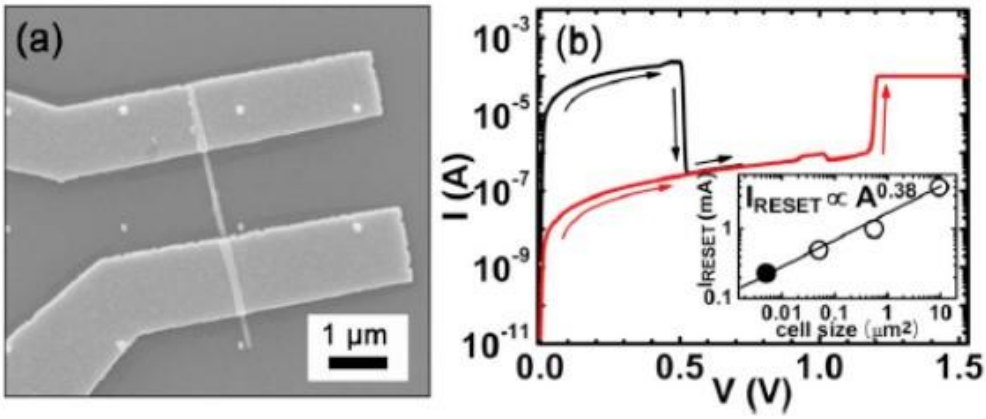

Fig. 1.17 SEM image of NiO nanowire contacted by EBL (a). In (b) the I-V's show the unipolar resistive switching between high and low resistance state [74].

In order to explain the switching between the two states, the variable diameter model was used. Due to the applied voltage, a CF grows within the oxide layer bridging the core of the NW enabling the LRS conduction. The reset operation occurs when enough heat is generated by the current to break the CF switching to the HRS. Following this publication, many other reports have demonstrated the possibility to use nanowires coated with oxide layers as active layer [75] or even metallic nanowires [76]. A fascinating alternative approach for memory device is represented by core-shell (CS) nanowires. Thanks to their structures they can combine the excellent conductivity of metallic nanowires with the switching properties of oxide materials. In a recent report [77], Manning et al. demonstrated a non-polar resistive switching behaviour using $AgTiO_2$ core-shell nanowires.

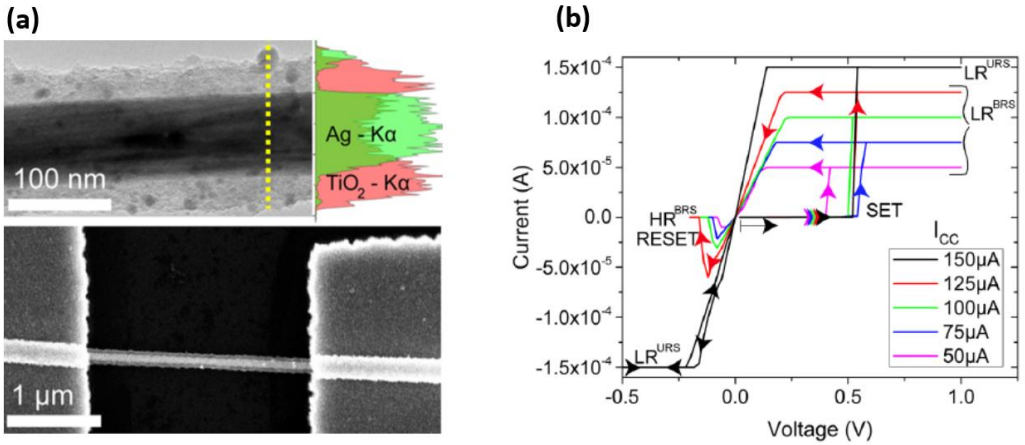

Fig. 1.18 In (a) TEM image of a $AgTiO_2$ nanowire with the EDX signal that shows the distribution of Ag and TiO_2 Kα signal along the nanowire. A SEM image shows the NW device contacted by Ag electrodes. In (b) I-V's that show non-polar resistive switching. Unipolar and bipolar switching can be obtained changing the I_{cc} during the set operation [77].

A full characterization of the sample can be found in Fig. 1.18 (a) [77]. The Transmission Electron Microscope (TEM) image shows the structure of the CS nanowire and highlights the sharp interface between the two different materials. The chemical analysis is performed through an Electron Diffraction X-ray (EDX) characterization and shows the peaks associated with the Ag and the TiO_2 along the perpendicular dashed line. The second image in Fig. 1.18 (a) shows instead the electrical device contacted through an Electron Beam Lithography (EBL) step with Ag electrodes. In Fig. 1.18 (b) representative I-V curves demonstrate the non-polar behaviour. In fact it is possible to note how the device shows, according to different SET operations, unipolar or bipolar switching properties. The transition between HRS and LRS is explained with an approach similar to the variable-gap model introduced in the section 1.3. The TiO_2 shell is considered as the active layer in which Ag ions can diffuse and form a CF as shown in Fig. 1.19 (a-d). Depending on the voltage polarity, two CFs can be grown within the two interfaces formed by the Ag electrodes and the TiO_2 layers. The non-polarity of the device can be also explained with the formation of CFs. The plot of the conductance vs the current compliance shown in Fig. 1.19 (f) identify the different regimes. For very low I_{cc}, less than $10\ nA$, a volatile switching behavior can be associated to the formation

of a weak filament within the interfaces. In this state the device, due to the poor strengthening effect of the current, cannot retain the information. Further increase of the I_{cc} will bring the device within an intermediate region where the sample acts as a bipolar switch. The compliance used for the set operation is sufficient to create a CF that bridges the electrodes with the internal core of the NW setting the device in the LRS. However, the CF is not sufficiently stable within the active layer as demonstrated from the poor retention time ($< 10\ s$). A negative voltage is then sufficient to switch the device back into the HRS granting the bipolar characteristic behaviour. Lastly, for very high compliances ($< 150\ \mu A$), the created filament can be associated to a permanent condition in which the system presents a unipolar behaviour. In this state, the device can switch to the HRS thanks to Joule heating effect taking place in voltage sweeps without compliance. The extremely high retention time, bigger than $10^7\ s$, also proves the stability of the state achievable within the unipolar regime.

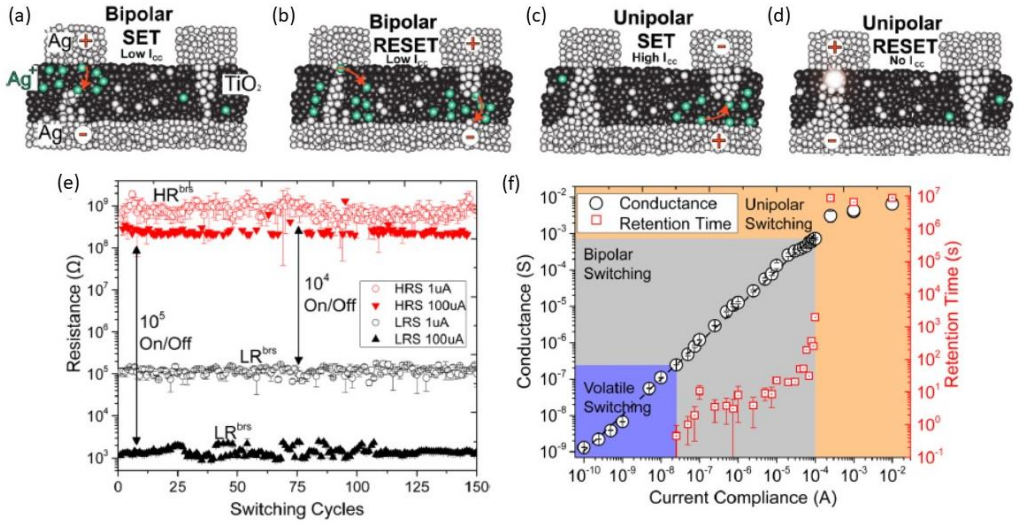

Fig. 1.19 Formation and dissolution of the CF within bipolar (a-b) and unipolar (c-d) regime. In order to test its endurance, the device was switched between the HRS and LRS over different cycles (e). In (f) the conductance is plotted versus the current compliance used for the set operation. Three different operational modes are reported. The retention time is also calculated for the different regimes [77].

In terms of integration within memory devices, core-shell nanowires present several remarkable qualities. The main advantage is the richness of states accessible with one single device. Merely changing the current compliance during the set operation three different conduction mechanisms can be obtained: (i) volatile devices for currents below $10\ nA$, (ii) bipolar behaviour for currents that range between $10\ nA$ and $100\ \mu A$ and (iii) for currents $< 150\ \mu A$, unipolar characteristics. Write/read voltages are usually quite low, well below $1\ V$, helping to reduce the energy per bit required to store information. The resistance ratio is another important parameter to consider in memory devices and, as shown in Fig. 1.18 (e), depending on the compliance, different ratios can be obtained. Remarkably a ratio of $R_{ratio} = 10^4$ can be achieved using the device as a bipolar switch or $R_{ratio} = 10^5$ in the unipolar regime.

1.5.3 Neuromorphic applications

Another promising application, perhaps the most fascinating one, consists of realizing artificial synaptic devices with the goal to mimic human brain behavior. The Blue Brain project [78], SpiNNaker program [79] or the True North chip [80] from IBM are only a few examples of projects initiated to develop a platform capable of processing information as the brain does. Cross-bars arrays of memory units, mostly SDRAM, are conventionally used as skeleton networks to replicate simple I/O operations. With this approach, very dense structures with 53×10^{10} neurons and 1.37×10^{14} synapses [79,80], can be achieved. In terms of numbers, a human brain has roughly 100 billion of neurons connected through 1000 trillion of synapses. But despite the numbers reached so far with CMOS structures, the main limitation arises from the fact that these architectures often require thousands or even megawatts of energy to process information [80]. It is therefore in this contest, that novel memristors offer unique properties that could potentially help to create synaptic devices. The bottom line idea is to replace CMOS arrays with MIM memristor cells in order to exploit their plasticity properties. The capabilities to store information with different retention times,

high $2D$ scalability, multilevel resistances, high switching speed and low power consumption are examples of the improvements that memristor bring towards the ultimate goal of brain-like or neuromorphic computation [81].

One of the first reports exploring the potentiality of nanowire networks as neuromorphic devices was introduced by Gimzewski et al in 2012 [82]. The importance of this publication arises from the fact that the authors aim at mimicking the brain functionality using different approaches. Instead of focusing the attention on conventional crossbar structures, a completely new platform, based on NWNs, is used for the purpose. It is possible to note that the two systems, networks and brains, share a large number of similarities. Starting from their structures resemblance, Fig. 1.20 shows a culture of hippocampal neurons [83] and an Ag NW network treated with $AgNO_3$ [84].

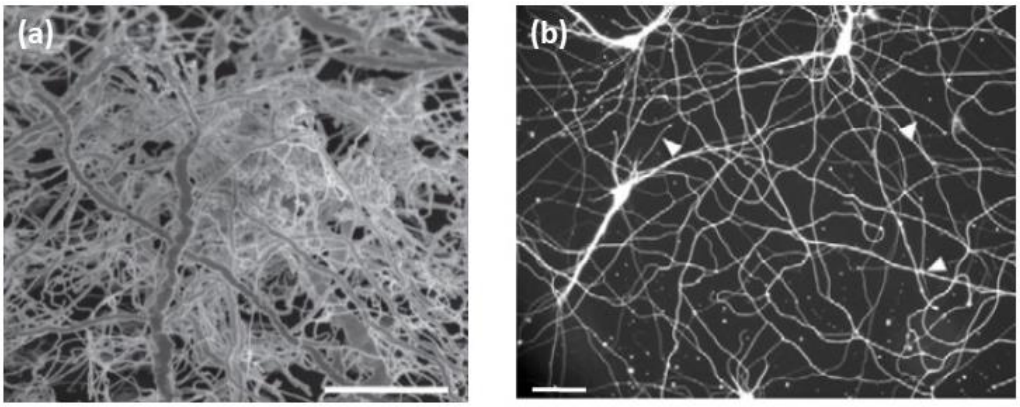

Fig. 1.20 Similarities between NWNs shown in (a) scale bar $10\ \mu m$ and neuronal networks in (b) with a $50\ \mu m$ scale bar [83,84].

At first sight, it might be quite complicated to distinguish between the two systems without further details. However, for completeness, the SEM image (a) associated to an Ag NW network (left side) has a scale bar of $10\ \mu m$ while for the neuronal network in (b) is $50\ \mu m$ (right side). The comparison proposed in Fig. 1.20 highlights the similarities from a topological point of view. However, many other similarities in how these systems propagate electrical signals can be found.

Within the brain, pulse signals travel through the neurons. A typical neuron, sketched in Fig. 1.21, consists of a soma (cell body), dendrites, and an axon [85].

Dendrites are thin structures that arise from the cell body, often extending for hundreds of micrometers and branching multiple times, giving rise to complex structures called "dendritic trees". An axon is a cellular extension, enclosed within myelin sheaths, that enables the travelling of information. The interface between the axon and the dendrites is known as synapses and represents the key component for the transmission of the signal among neurons. Each synapse within the brain has a certain voltage threshold that acts as a barrier beyond which the information can be “fired”.

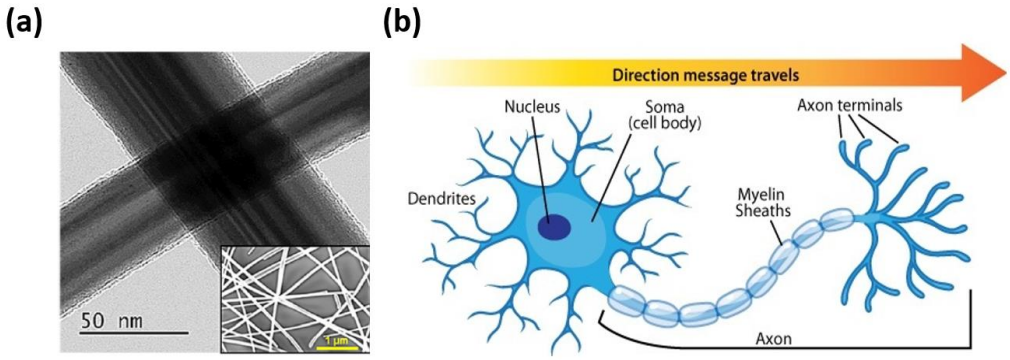

Fig. 1.21 A TEM image of an Ag NWs junction [85] (a) and a sketch of a neuron in (b) [86,87]. In making a paragon, the NWs junctions explicates the neuron functionalities while the actual wires represent the connections that within the brain are made by the axons.

Considering a memristive network made of core-shell nanowires as the synthetic version of a biological neural network, the information travels along the network through the internal core of the nanowires. However, junctions as the one shown in Fig. 1.21 (a) are the crucial components that make possible the comparison between networks and brains. A junction can acts as a MIM device in which the memristor behavior comes from the active insulating layer interposed between the wires that comprise the junction. The memory effect is associated with the motion of ions that creates CFs within the active layer. As discussed in section 1.2.2 different conduction mechanisms are possible by choosing the appropriate materials. With this in mind, it is possible to make an analogy between junctions within a NW network and synapses within the brain. A wide range of possible conduction mechanism allow the memristive junction to act as the synapses do.

Unipolar, bipolar, complementary switches or even rectifying behavior are achievable with memdevices which not only opens up the possibility to mimic synaptic behavior but to implement additional features or functionalities [34,84]. For example, if the voltage applied to the cell is sufficient to switch to the LRS, the electrical signal can travel through the core of the wire and reach the next junction just as in neurons.

Another important characteristic of the brain is the plasticity associated with the learning mechanism. According to the theory introduced by Hebb [88,89], during the learning process the information is stored within the brain thanks to the strengthening mechanism of neurons. Each neuron has a determinate barrier or weight associated to it. It has been proved that, during the learning process, the barriers of the neurons carrying the information is lowered [87]. At the same time, the barrier of the neurons not involved in the process will increase further helping the learning process. In the same way junctions within networks can replicate this behavior as shown in Fig. 1.22 for the case of an Ag NW network chemically treated. A triangular shape voltage sweeps $(0 - 5\ V)$ is applied to the network and the current response is shown in (b) [82]. A schematic representation of the network is subsequently shown in Fig. 1.22 (c). The migration of silver sulfide within the junctions carrying the signal causes a strengthening effect that ultimately lower the voltage threshold among the junctions.

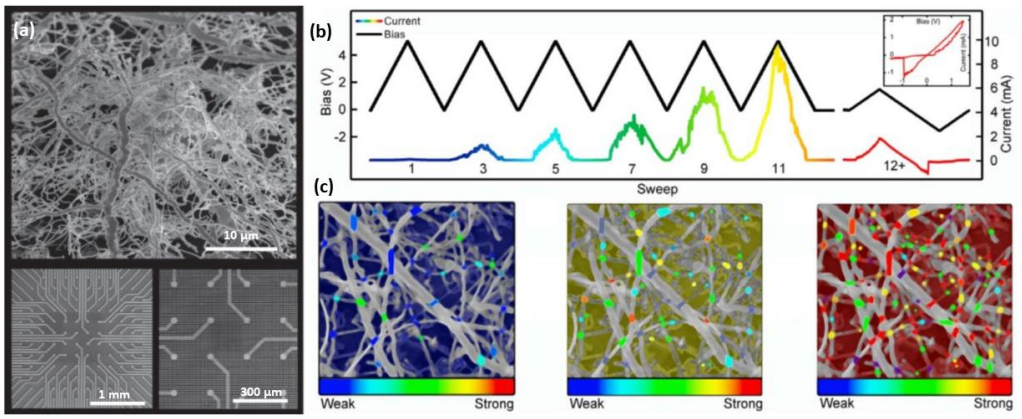

Fig 1.22 SEM images at different magnification of SiO_2 sample containing the Pt electrodes (a) before growing the $AgNO_3$ network [82]. In (b) the electrical signal collected from the network that shows the current evolution as the voltage is supplied to the network. In (c) a schematic representation describing the connectivity evolution within the film.

1.6 Thesis outline

This thesis aims to describe the electrical behaviour of random networks of nanowires with resistive junctions. To do this, the first chapter introduces the motivation for the work, providing a wide view on the state of the art of the fields of resistive switching and nanowire networks as well as recent works on networks incorporating resistive switching junctions. The second chapter focuses in detail on the principle and theory behind the equipment used during this PhD project and describes the experimental methods for the fabrication of the devices and the electrical testing. The third chapter aims to investigate the activation process within random oriented nanowire networks. After a brief introduction, the models used to describe the networks activation will be discussed. The second part of the chapter, provides a first characterization of the electrical properties of Ag random oriented nanowire networks. The main part of the work performed during this project is presented on Chapter 4. A detailed study on the activation process highlights the formation of the “winner-takes-all” path within networks. This path, that spans the entire network, can be considered as the most favourable configuration for signal propagation. Remarkably, the same phenomenon that happens macroscopically can be either seen at the nanometre scale within

junctions with the formation of conductive filaments. This proves that a wide class of nanowire materials, assembled as network or junctions, show self-similar scaling behaviour. The final chapter is based on the study of alternative core-shell structure materials as further step for the implementation of nanowires within devices. The qualities shown by polymer coated nanowire network are further enhanced by exploiting the typical memristive behavior of core-shell structures. In the conclusion, a summary of all the work done during this PhD project is presented followed by the possible future works in this field.

References

1. Siemon, A. *et al.* Realization of Boolean Logic Functionality Using Redox-Based Memristive Devices. (2015).
2. Feynman, R. P. There's Plenty of Room at the Bottom An Invitation to Enter a New Field of Physics, (1959).
3. Collaert, N. Extending Moore ' S Law : Nanowires To the Rescue, (2013).
4. Moore, G. E. Lithography and the future of Moore's Law (2006).
5. Technological Progress - Our World in Data.
6. Intel innovation from the start, (2003)
7. Kothe, D. B. *Science Prospects and Benefits with Exascale Computing,* (2007).
8. R. Kapoor, R. Adner. The lithography ecosystem (2007)
9. ITRS. International Technology Roadmap for Semiconductors, (2015).
10. Nagy, D. *et al.* FinFET versus gate-all-around nanowire FET: Performance, scaling, and variability, (2018).
11. Cavin, R. K., Lugli, P. & Zhirnov, V. V. Science and Engineering Beyond Moore's Law, (2012).
12. Nws, S. *et al.* Imec demonstrates gate-all-around MOSFETs with lateral silicon nanowires at scaled dimensions, (2016).
13. Chua, L. 0. Memristor-The Missing Circuit Element, (1971).
14. Adhikari, S. P., Sah, M. P., Kim, H. & Chua, L. O. Three Fingerprints of Memristor, (2013).
15. Kavehei, O. *et al.* The fourth element: characteristics, modelling and electromagnetic theory of the memristor, (2010).
16. Hickmott, T. W. Low-Frequency Negative Resistance in Thin Anodic Oxide Films, (1962).
17. Strukov, D. B., Snider, G. S., Stewart, D. R. & Williams, R. S. The missing memristor found, (2008).
18. Mazumder, P., Kang, S. M. & Waser, R. Memristors: Devices, models, and applications, (2012).
19. Yang, Y., Sheridan, P. & Lu, W. Complementary resistive switching in tantalum oxide-based resistive memory devices, (2012).
20. Linn, E., Rosezin, R., Kügeler, C. & Waser, R. Complementary resistive switches for passive nanocrossbar memories, (2010).
21. Waser, R., Dittmann, R., Staikov, C. & Szot, K. Redox-based resistive switching memories nanoionic mechanisms, prospects, and challenges, (2009).
22. Singh Meena, J., Min Sze, S., Chand, U. & Tseng, T.-Y. Overview of emerging nonvolatile memory technologies, (2014).
23. Chang, T.-C., Chang, K.-C., Tsai, T.-M., Chu, T.-J. & Sze, S. M. Resistance random access

memory, (2016).

24. Govoreanu, B. *et al.* 10×10nm 2 Hf/HfO x crossbar resistive RAM with excellent performance, reliability and low-energy operation, (2011).
25. Miao, F. *et al.* Anatomy of a nanoscale conduction channel reveals the mechanism of a high-performance memristor, (2011).
26. Tappertzhofen, S., Valov, I. & Waser, R. Quantum conductance and switching kinetics of AgI-based microcrossbar cells, (2012).
27. Jang, H. J., Kirillov, O. A., Jurchescu, O. D. & Richter, C. A. Spin transport in memristive devices, (2012).
28. Yang, J. J. *et al.* High switching endurance in memristive devices, (2010).
29. Akinaga, H. & Shima, H. Resistive Random Access Memory (ReRAM) Based on Metal Oxides, (2010).
30. Russo, U., Kamalanathan, D., Ielmini, D., Lacaita, A. L. & Kozicki, M. N. Study of multilevel programming in Programmable Metallization Cell (PMC) memory, (2009).
31. Valov, I. Interfacial interactions and their impact on redox- based resistive switching memories (ReRAMs) Interfacial interactions and their impact on redox-based resistive switching memories (ReRAMs), (2017).
32. Tsuruoka, T. *et al.* Humidity effects on the redox reactions and ionic transport in a Cu/Ta<inf>2</inf>O<inf>5</inf>/Pt atomic switch structure, (2016).
33. Tappertzhofen, S., Waser, R. & Valov, I. Impact of the Counter-Electrode Material on Redox Processes in Resistive Switching Memories, (2014).
34. Valov, I., Waser, R., Jameson, J. R. & Kozicki, M. N. Electrochemical metallization memories—fundamentals, applications, prospects, (2011).
35. Kim, K. M., Jeong, D. S. & Hwang, C. S. Nanofilamentary resistive switching in binary oxide system; a review on the present status and outlook, (2011).
36. Tappertzhofen, S. *et al.* Modeling of Quantized Conductance Effects in Electrochemical Metallization Cells, (2015).
37. Menzel, S. *et al.* Statistical modeling of electrochemical metallization memory cells, (2014).
38. Balatti, S., Larentis, S., Gilmer, D. C. & Ielmini, D. Multiple Memory States in Resistive Switching Devices Through Controlled Size and Orientation of the Conductive Filament, (2013).
39. Sawa, A. & Meyer, R. *Resistive Switching from fundamentals of nonoionic redox processes to Memristive Device Applications,* (2016).
40. S. Munjal, N. Khare Valence Change Bipolar Resistive Switching Accompanied With Magnetization Switching in CoFe 2 O 4 Thin Film, (2017).
41. Menzel, S., Tappertzhofen, S., Waser, R. & Valov, I. Switching kinetics of electrochemical metallization memory cells, (2013).

42. Valov, I. & Kozicki, M. N. Cation-based resistance change memory, (2013).
43. Tiwari, J. N., Tiwari, R. N. & Kim, K. S. Zero-dimensional, one-dimensional, two-dimensional and three-dimensional nanostructured materials for advanced electrochemical energy devices, (2012).
44. Lee, C. H. *et al.* Room-temperature tunneling behavior of boron nitride nanotubes functionalized with gold quantum dots, (2013).
45. Heiligtag, F. J. & Niederberger, M. The fascinating world of nanoparticle research, (2013).
46. Son, D. I. *et al.* Bistable organic memory device with gold nanoparticles embedded in a conducting poly(N -vinylcarbazole) colloids hybrid, (2011).
47. Kim, S. H. *et al.* Nanoscale Chemical and Electrical Stabilities of Graphene-covered Silver Nanowire Networks for Transparent Conducting Electrodes, (2016).
48. Hecht, D. S., Hu, L. & Irvin, G. Emerging transparent electrodes based on thin films of carbon nanotubes, graphene, and metallic nanostructures, (2011).
49. Agraït, N., Yeyati, A. L. & van Ruitenbeek, J. M. Quantum properties of atomic-sized conductors, (2003).
50. Kuchibhatla, S. V. N. T., Karakoti, A. S., Bera, D. & Seal, S. One dimensional nanostructured materials, (2007).
51. Ye, S. *et al.* How Copper Nanowires Grow and How To Control Their Properties, (2016).
52. Noy, A. & Artyukhin, A. B. Bionanoelectronics with 1D materials, (2009).
53. An, L. & Friedrich, C. R. Measurement of contact resistance of multiwall carbon nanotubes by electrical contact using a focused ion beam, (2012).
54. Tenent, R. C. *et al.* Ultrasmooth, Large-Area, High-Uniformity, Conductive Transparent Single-Walled-Carbon-Nanotube Films for Photovoltaics Produced by Ultrasonic Spraying, (2009).
55. Fagas, G. *et al.* Component design and testing for a miniaturised autonomous sensor based on a nanowire materials platform, (2014).
56. Ye, S., Rathmell, A. R., Chen, Z., Stewart, I. E. & Wiley, B. J. Metal nanowire networks: The next generation of transparent conductors, (2014).
57. De, S. & Coleman, J. N. The effects of percolation in nanostructured transparent conductors, (2017).
58. Sannicolo, T. *et al.* Metallic Nanowire-Based Transparent Electrodes for Next Generation Flexible Devices: a Review, (2016).
59. An, L. & Friedrich, C. R. Measurement of contact resistance of multiwall carbon nanotubes by electrical contact using a focused ion beam, (2012).
60. Bellew, A. T., Manning, H. G., Gomes Da Rocha, C., Ferreira, M. S. & Boland, J. J. Resistance of Single Ag Nanowire Junctions and Their Role in the Conductivity of Nanowire Networks, (2015).
61. Chen, J. Z., Ahn, H., Yen, S. C. & Tsai, Y. J. Thermally induced percolational transition and

thermal stability of silver nanowire networks studied by THz spectroscopy, (2014).

62. Rathmell, A. R. & Wiley, B. J. The Synthesis and Coating of Long , Thin Copper Nanowires to Make Flexible , Transparent Conducting Films on Plastic Substrates, (2011).
63. Fei Guo, C. & Ren, Z. Flexible transparent conductors based on metal nanowire networks, (2015).
64. Han, S. *et al.* Fast plasmonic laser nanowelding for a Cu-nanowire percolation network for flexible transparent conductors and stretchable electronics, (2014).
65. Garnett, E. C. *et al.* Self-limited plasmonic welding of silver nanowire junctions, (2012).
66. Liu, Y. *et al.* Capillary-Force-Induced Cold Welding in Silver-Nanowire-Based Flexible Transparent, (2017).
67. Langley, D. *et al.* Flexible transparent conductive materials based on silver nanowire networks: A review, (2013).
68. Lagrange, M. *et al.* Optimization of silver nanowire-based transparent electrodes: effects of density, size and thermal annealing, (2015).
69. Langley, D. P. *et al.* Silver nanowire networks: Physical properties and potential integration in solar cells, (2014).
70. Johnson, S. L., Sundararajan, a, Hunley, D. P. & Strachan, D. R. Memristive switching of single-component metallic nanowires, (2010).
71. O 'kelly, C., Fairfield, J. A. & Boland, J. J. A Single Nanoscale Junction with Programmable Multilevel Memory, (2014).
72. Li, Q. *et al.* Flexible transparent memory cell: bipolar resistive switching via indium–tin oxide nanowire networks on a poly(dimethylsiloxane) substrate, (2016).
73. Kim, S. I., Lee, J. H., Chang, Y. W. & Yoo, K. H. Reversible resistive switching behaviors in NiO nanowires, (2010).
74. Kim, S. I., Lee, J. H., Chang, Y. W., Hwang, S. S. & Yoo, K.-H. Reversible resistive switching behaviors in NiO nanowires Scaling behaviors for resistive memory switching in NiO nanowire devices Reversible resistive switching behaviors in NiO nanowires, (2008).
75. Liang, K.-D. *et al.* Single CuO x Nanowire Memristor: Forming-Free Resistive Switching Behavior, (2014).
76. Bellew, A. T., Bell, A. P., McCarthy, E. K., Fairfield, J. A. & Boland, J. J. Programmability of nanowire networks, (2014).
77. Manning, H. G., Biswas, S., Holmes, J. D. & Boland, J. J. Nonpolar Resistive Switching in Ag@TiO 2 Core−Shell Nanowires, (2017).
78. Jasinski, "The Blue Brain Project", (2004).
79. Furber, S. B., Galluppi, F., Temple, S. & Plana, L. A. The SpiNNaker project, (2014).
80. Cassidy, A. S. *et al.* 28-1: TrueNorth: a High-Performance, Low-Power Neurosynaptic Processor for Multi-Sensory Perception, Action, and Cognition, (2016).
81. Adam, G. C. *et al.* 3-D Memristor Crossbars for Analog and Neuromorphic Computing

Applications, (2017).

82. Avizienis, A. V *et al.* Neuromorphic Atomic Switch Networks, (2012).
83. C. Fassier et al. Microtubule-targeting drugs rescue axonal swellings in cortical neurons from spastin knockout mice, (2013).
84. Demis, E. C. *et al.* Atomic switch networks—nanoarchitectonic design of a complex system for natural computing, (2015).
85. Sperl, M., Chang, A., Weber, N. & Hü, A. Hebbian learning in the agglomeration of conducting particles, (1999).
86. Sannicolo, T. *et al.* Direct Imaging of the Onset of Electrical Conduction in Silver Nanowire Networks by Infrared Thermography: Evidence of Geometrical Quantized Percolation (2016).
87. C.Ramos *et al.* On spike-timing-dependent-plasticity, memristive devices, and building a self-learning visual cortex, (2011).
88. D. Soudry *et al.* Hebbian Learning Rules with Memristors, (2013).
89. Cantley, K. D., Subramaniam, A., Stiegler, H. J., Chapman, R. A. & Vogel, E. M. Hebbian learning in spiking neural networks with nanocrystalline silicon TFTs and memristive synapses, (2011).

Chapter 2

Equipment and methods

A variety of equipment and techniques used during this PhD project to fabricate and analyse samples are described in this chapter. At the beginning a brief explanation of the theory and the operating principles introduces the readers to the one of the most used tool in this research, the electron microscope. Following, all the fabrication steps and the techniques used to realize devices are described before concluding with a description of the electrical test setup utilized for the characterization of the devices in this thesis.

All the work for this PhD project was completed and made possible thanks to the facilities within the Advanced Microscopy Laboratory (AML) and Centre for Research on Adaptive Nanostructures and Nanodevices (CRANN).

2.1 Microscopy

The word microscope is derived from the Greek mikros (small) and skopeo (look at). From the dawn of science there has been an interest in being able to look at smaller and smaller details of the world around us. One of the earliest instruments for seeing "very small" objects was made by Antony van Leeuwenhoek [1], also known as the father of microbiology. His first attempt consisted of a powerful convex lens and an adjustable object capable to magnify objects up to $400\times$. Some 200 years later, in 1873, Ernst Abbe in his publication [2] provided the scientific basis for conventional light microscopes. Abbe predicted that the maximum resolving power of visible light, according to $d = 0.612\,\lambda/NA$, was

limited to $200\ nm$ at best, where d is the optical resolution, λ is the wavelength of the light and NA represents the numerical aperture. However, the real breakthrough was made by De Broglie in 1924 with his hypothesis of wave-particle duality [3]. De Broglie proposed that particles have wave-like behaviour with an associated wavelength that can be calculated as $\lambda = h/mv$, which can be significantly below that of the optical light. Here h is the Planck's constant and m and v are respectively the mass and velocity of the particle. De Broglie's discovery paved the way for further upgrade in resolution thanks to the development of the electron microscopes. Considering for example to have an electron with $1000\ eV$ energy, according to the relation introduce earlier it has a wavelength of approximately $12\ \text{Å}$. Exploiting these dramatically reduced wavelengths, electron microscopies can achieve spatial resolutions that are unreachable with conventional light microscopes.

2.1.1 Scanning Electron Microscopy SEM

Scanning electron microscope (SEM) is a very powerful tool used worldwide in nanoscience field. Thanks to its versatility users are able to resolve objects on nanometre scale and/or to fabricate devices with an incredible spatial resolution. Depending on the energy of the incident electron, SEMs can operate in scanning mode SEM (Scanning Electron Microscope) or in transmission mode TEM (Transmission Electron Microscope). In addition these microscopes can also be used for chemical analysis with Energy-dispersive X-ray spectroscopy (EDX) or for nanofabrication as Electron Beam Lithography (EBL).

A conventional SEM column is shown in Fig. 2.1 and can be ideally schematized in three different sections. The top part of the chamber generates the electron beam required for the microscope operation. The e^- beam is commonly generated using thermionic or field emission guns (FEG). Tungsten (W) and Lanthanum hexaboride (LaB_6) are widely used as thermionic sources due to their high efficiency and low energy barriers for emission (see table 2.1). On the other hand, field emission sources can produce beams with higher brightness and a more

defined energy spreads in respect to thermionic gun, yielding higher resolution. Table 2.1 summarizes the operation parameters for the different electron sources.

Table 2.1 Comparison between different electron sources. FEG are commonly used as e^- sources due to their higher brightness and well defined energy beam.

	Tungsten	***LaB6***	***Cold FEG***	***Schottky emitter FEG***
Brightness (A/Cm²str)	10^6	10^6	10^9	10^8
Energy spread (eV)	*1-3*	*1-2*	*1*	*0.3*
Lifetime (hrs)	*40-100*	*200-1000*	*>1000*	*>2000*
Column vacuum required (mbar)	$< 10^{-4}$	$< 10^{-6}$	$< 10^{-10}$	$< 10^{-8}$

Due the high brightness and energy resolution *FEGs* are commonly used as sources for electron microscope. Unfortunately, the main disadvantage is their surface sensitivity to contamination and oxidation. In order to prevent such problems high level of vacuum and temperature flashes are required to clean the surface at regular time intervals. An electron gun generates the e^- that after passing through anode and a Wehnelt systems are accelerated and focalised towards the centre of the column. The central section comprises an electromagnetic system made of apertures and condenser lens that further focus and collimate the beam into the direction of the sample. Two scanning coils oriented perpendicularly to each other are used to raster the beam during the imagining process in the x and y directions. Lastly, the final part of the chamber is where the focussed beam interacts with the sample and the transmitted or scattered electrons are collected, after the interaction with the sample. Furthermore, it is important to remark that the final section is isolated from the rest of the chamber via a shutter to allow loading and unloading samples. In doing so, only a small part of the chamber is exposed to the atmosphere decreasing the time to create the vacuum and at the same time minimising contamination. This section of the chamber is also equipped with a detecting system that collects the exiting e^- and enables the visualization of an image of the sample on a computer screen.

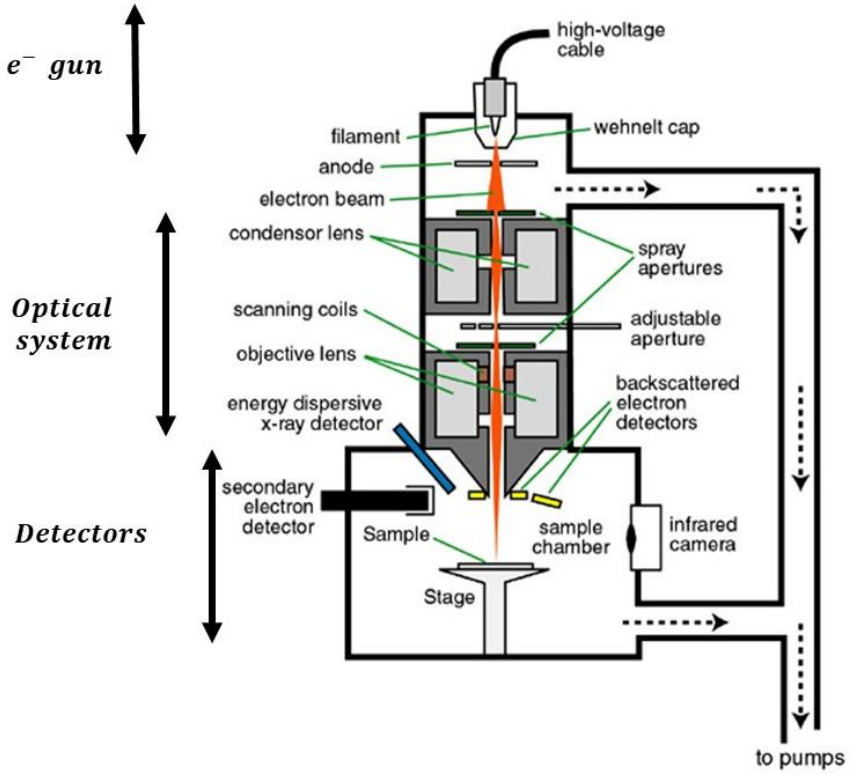

Fig. 2.1 Schematic of a scanning electron microscope (SEM) that highlights the three sections of the chamber [4].

2.1.1.1 Electron-sample interaction

The interaction between the e^- beam and the specimen generates electrons and photons that contain information about the topology and chemical composition of the sample. As a result of the collision, electrons can experience elastic or inelastic scattering events. In the first case, their energy is not affected by the collision, while in the latter case a quantity of energy ΔE is dissipated within the material. SEMs usually create an image of the sample using inelastic scattered electrons. TEMs, on the other hand, can reach incredible spatial resolution collecting the elastically scattered electrons. Photons, usually generated by Bremsstrahlung effect or by recombination events follow the ejection of electron from core levels of the atoms in the sample and so provides information on the composition of the material (see section 2.13).

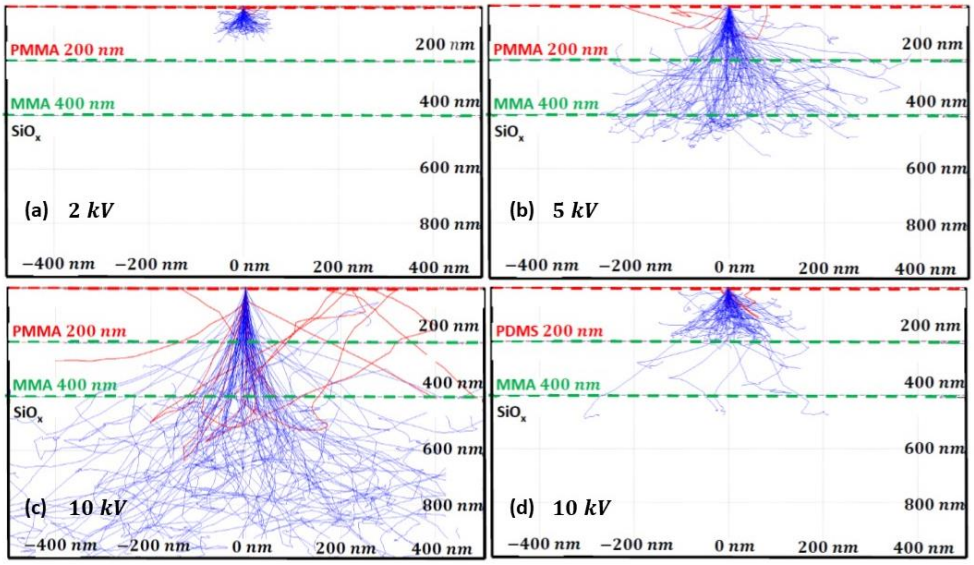

Fig. 2.2 Simulation performed with CASINO software to study the interaction between an electron beam and different layers of materials. The energy is increased going from (a) $2\ kV$ to (c) $10\ kV$ in order to confirm Kanaya-Okayama formula introduced later in this chapter [5]. In (d) the top layer is replaced with a denser material to prove the dependence on the atomic number.

A Monte Carlo simulation is shown in Fig. 2.2 and describes the interaction of the beam and the sample modifying the energies of the incoming electrons. The simulation aims to replicate the same conditions used in the EBL process (see section 2.4). However, it can be easily generalized to different samples and conditions. A $2\ \mu m$ silicon substrate is used as support in the simulation and two resists, poly methyl methacrylate (PMMA) and methyl methacrylate (MMA), are spun onto the substrate forming two $200\ nm$ thick layers. Fig. 2.2 (a-c) points to the fact that higher energy e^- usually result in deeper penetration of the beam within the material. Moreover, the atomic number of the specimen is another important parameter that regulates the interaction. Panels (c-d) have the same incoming e^- energies, the only difference is the replacement of the PMMA layer with a polydimethylsiloxane (PDMS) layer of the same thickness. As can be seen, the vast majority of e^- is stopped by the PMDS layer due to its high density in comparison to the PMMA layer. In this case, the generation of secondary electrons (SEs), shown as red lines, which are extremely important for imaging in SEM mode is also dramatically reduced. Might appears clear referring to Fig. 2.2 (a-b) that for

low kV beam electrons almost no secondary electrons are generated. However, a discrete number of secondary scattering events are generated when the energy is sufficient to create the SEs with sufficient energy to travel within the material. The behaviour is phenomenologically described in the Kanaya-Okayama relationship [5].

$$R_{KO}(\mu m) = 0.0276 \frac{A{E_0}^{1.67}}{\rho Z^{0.89}} \quad \text{Eq. (2.1)}$$

In this model, the penetration range R_{KO} is the maximum distance that electrons, with an initial energy E_0, can travel within a certain specimen. ρ, Z and A are respectively the density, atomic number and atomic mass of the specimen material. The interactions, as can be seen from the simulation reported in Fig. 2.2, create an interaction volume. The "tear drop shape" represents the volume from which the scattered electrons and photons will be emitted. The interaction volume depends mainly on three different factors: energy beam, atomic number/density of the material and the angle between source and sample. Fig. 2.3 lists the different outcomes resulting from the interaction of the beam with the specimen.

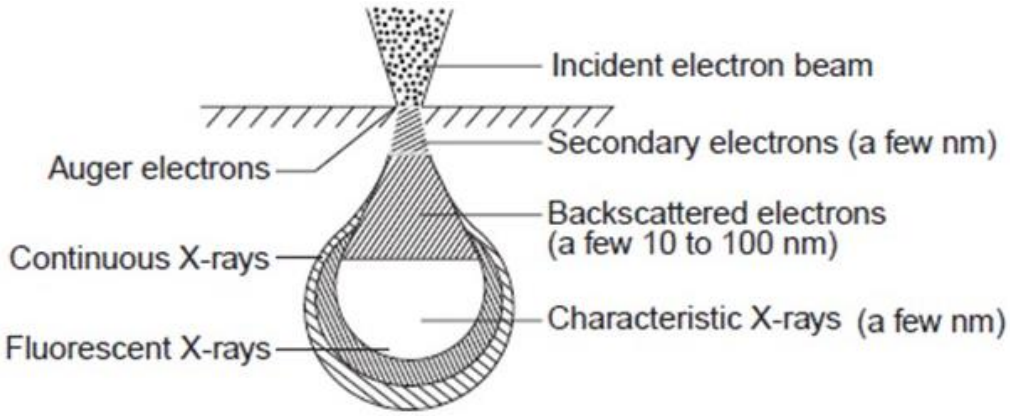

Fig. 2.3 A sketch of the interaction volume and the relative exiting signals in respect to the penetration distance along the material. The working principle of SEMs is based on the collection of the secondary electrons. TEMs reconstruct the image of the sample using the elastically scattered e^-. Several other contributions such as the characteristic X-rays can be either used to have information about the specimen material.

Commonly it is possible to distinguish between electrons or x-ray signals. The secondary electrons as described before are produced by collisions with atoms or

electrons present in the specimen. Backscattered electrons are instead result of an elastic collision with the ion within the material. Moreover, Auger electrons are generated by a recombination process that is described later in this chapter in section 2.1.3. The impinging electrons knock out an electron within the material leaving a vacancy that is filled by an electron present in an outer shell. The energy released in the process can be released as a characteristic X-ray signal or conferred to a third electrons known as Auger electron. This interaction generates a wide spectrum of x-ray signals specifically detailed later discussing EDX technique.

The electrons produced by the beam-sample interaction have to have sufficient energy to be collected as they leave the specimen. The exiting process is often described by the e^- inelastic mean free path (IMFP) curve shown in Fig. 2.4. The IMFP represents the maximum distance that the electrons can travel through a certain specimen before the occurrence of an inelastic scattering event.

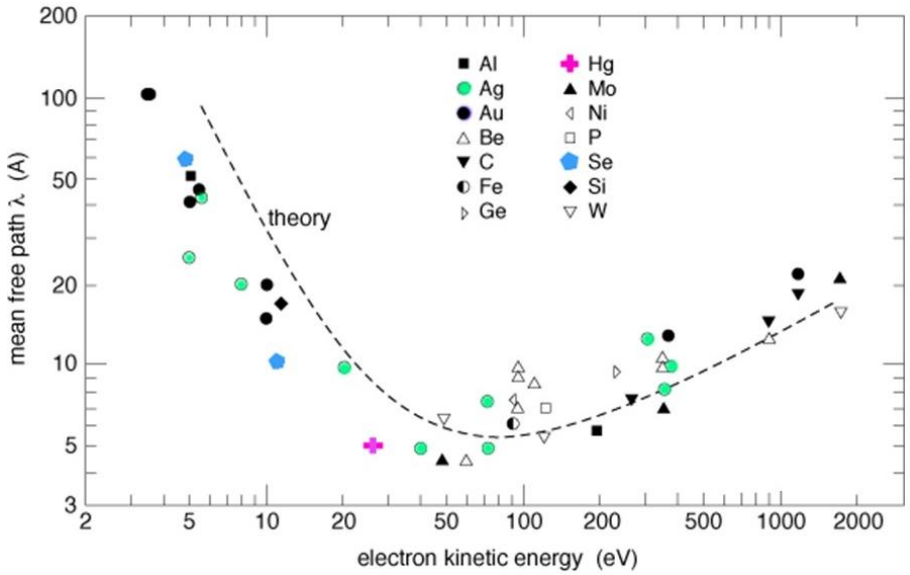

Fig. 2.4 Inelastic mean free path curve for different materials [6]. After the collisions the e^- have energy usually lower than $20\ eV$, therefore, only the electrons scattered in proximity of the surface have sufficient energy to leave the sample and be collected by the detectors.

Electrons that have energies in the range from $10 - 20\ eV$ can only travel few nm within the material. As a consequence, only the electrons produced in proximity of the surface are able to leave the sample and be collected by the detectors.

Moreover, electrons produced far from the surface will remain trapped within the material losing energy by further collisions.

2.1.1.2 PVC Passive Voltage Contrast

Passive Voltage Contrast (PVC) technique is widely used by semiconductors companies to detect electrical failures within integrated circuits. The technique is based on the different level of SEM contrast from electrically floating objects compared to grounded objects on the same sample. During this project, the PVC technique has been used to highlight the activated nanowires within Ag NWNs. The charge, generated by the beams as it scan across the network, is free to leak from the grounded regions but becomes trapped on the floating parts. This creates an accumulation of SEs at the surface of the latter regions and consequently results in the built up of a potential that will prevent electrons to escape from the material. In principle, a material that is negatively biased appears bright due to an increase in the secondary electron yield [7]. Whereas, a positive bias causes a reduction in yield resulting in a dark contrast. The yield of SE σ defined as the ratio between the incoming electrons from the beam and outgoing scattered electrons from the sample is also strongly dependent on the incident angle between the beam and the sample and the beam energy as summarized by Fig. 2.5 [7]. Changing the angle between the surface and the electron gun increases the SE yield as depicted in Fig. 2.5 (a). This is merely related to geometrical considerations, as can be seen from Fig. 2.5 (b), the escaping area is wider in the tilted case.

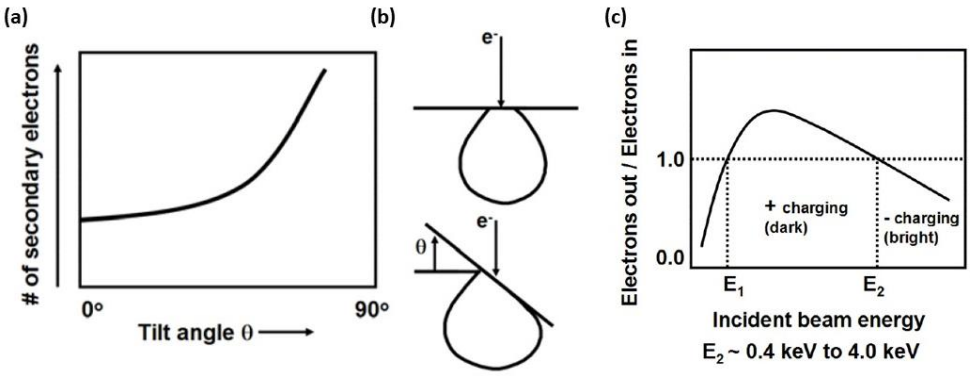

Fig. 2.5 Dependences of the yield defined as the ratio between the incoming and exiting e^- respect the tilting angle (a,b) and the beam energy (c) [8]. The number of incoming e^- is defined by the users setting the aperture of the beam. The out coming are instead related to the beam energy but most importantly their number depend from the IMFP curve shown in Fig. 2.4.

Furthermore, Fig. 2.5 (c) shows how the energy of the beam influences the yield of SE. For very low energy beams with $E < E_1$ the quantity of SE generated is relatively small and the overall contrast of floating objects will appear bright. There is then an energy window $E_1 < E < E_2$ in which σ becomes bigger than 1. In this condition, a large number of SE will be emitted from the sample and the surface will be covered with positive charges resulting in a dark contrast for floating parts. In the final case, for high energies ($E > E_2$), the electrons have enough energy to travel deep within the material. Therefore, the number of SE emitted will be smaller than the incoming electrons. This will lead to yield smaller 1 and a brighter contrast. A demonstration of this behaviour is shown in Fig. 2.6 in which a circuit with a glass passivation layer is used to show different levels of contrast using different energy beams.

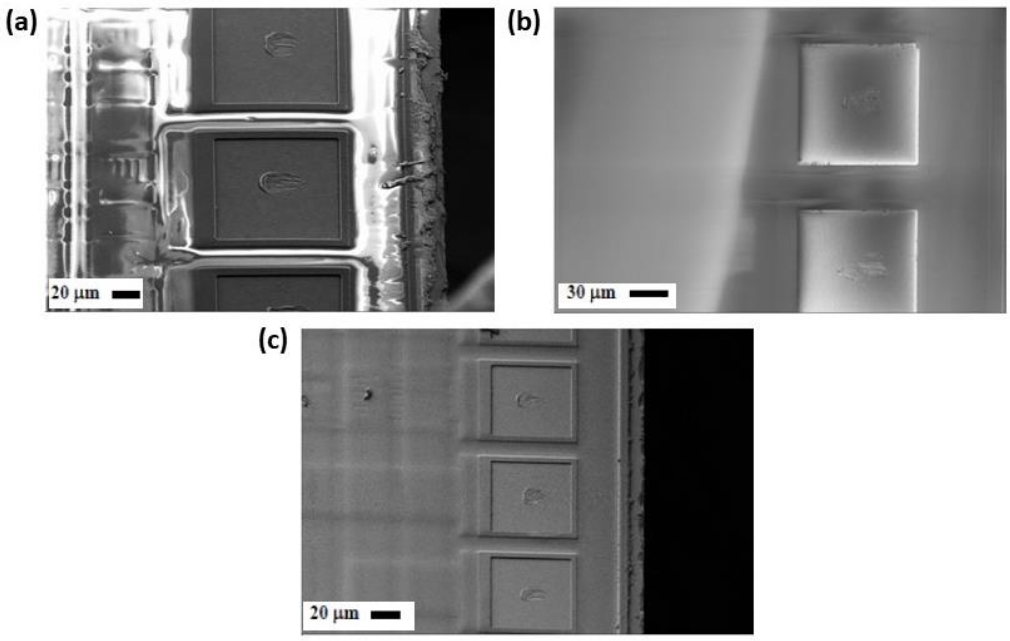

Fig. 2.6 Capabilities of the passive voltage contrast technique. The sample used has the electrodes (square shapes) which are grounded while the surroundings is an insulating glass passivation layer [7]. The three different conditions are linked to the yield described in Fig. 2.5 (c). In Fig. 2.6 (a) a $10\ kV$ energy beam is used to obtain a $\sigma < 1$ obtaining a certain contrast. In Fig. 2.6 (b) a lower energy is instead chosen to have a yield greater than 1 obtaining an opposite contrast. Lastly in Fig. 2.6 (c) the energy is tuned to achieve a condition where $\sigma = 1$ resulting in a more clear and focussed image.

In Fig. 2.6 (a) the acceleration voltage of the beam is $10\ kV$ and referring to Fig. 2.5 (c) the yield $\sigma < 1$. In this condition there is an excess of negative charges. The grounded electrodes are free of charge and therefore no charging is visible on them. The charge on the grounded electrodes is free to leak away and therefore there is no charging effect. On the other hand, the passivation layer traps charges that accumulating on the surface appears brighter.

In Fig. 2.6 (b) the beam energy is $1\ keV$, the yield is larger than 1 and the number of SEs collected by the detector is greater than the incoming e^- beam. In this frame the contrast is the complete opposite with respect to (a). In fact the electrodes in this case show a brighter contrast while the floating one appear darker.

Lastly, in Fig. 2.6 (c), the energy was tuned to have a yield $\sigma = 1$. This condition is achievable with an appropriate beam energy in order to have an energy $E = E_1 =$

E_2. For this particular case the beam energy is $2.5\ keV$, but as proven by Vanderlinde et al [7], it is strongly related to the topography and composition of the studied sample. The energy values are usually determined experimentally as they are material dependent. The energy of the beam is chosen to neutralize the charge on the surface. This leads to clear and well define images even for non-conducting samples. Later, in section 4.4, the same type of analysis will be performed on the NWNs in order to highlight the activated nanowires across the network.

2.1.2 TEM Transmission Electron Microscopy

The second imaging technique used during this project for the characterization of NWs is Transmission Electron Microscopy or TEM. One of the main differences to SEM is that the image is obtained, as the name suggests, using transmitted electrons. For this reason the energy ranges in SEM are quite different from the energies used in TEM. As stated before SEM collects secondary electrons and therefore its energies range from few KeV up to $30\ KeV$. In TEM the electrons have to travel through the material and for this reason higher energies, between $60\ KeV$ and $300\ KeV$, are required. As reported by Tanuma et al. [6] the relative inelastic mean free path, considering Ag as sample material, vary from 60.8 Å to 238.2 Å. Consequently, particular sample preparations are often required in TEM to thin down the thickness of the material to around 150 Å. This allows the electron to travel through the material and after the interaction with the specimen, the transmitted e^- will be collected on a fluorescent screen or redirected to a PC screen. The different working principle of TEM compared to SEM requires a different arrangement of the sample within the column, as shown in Fig. 2.7.

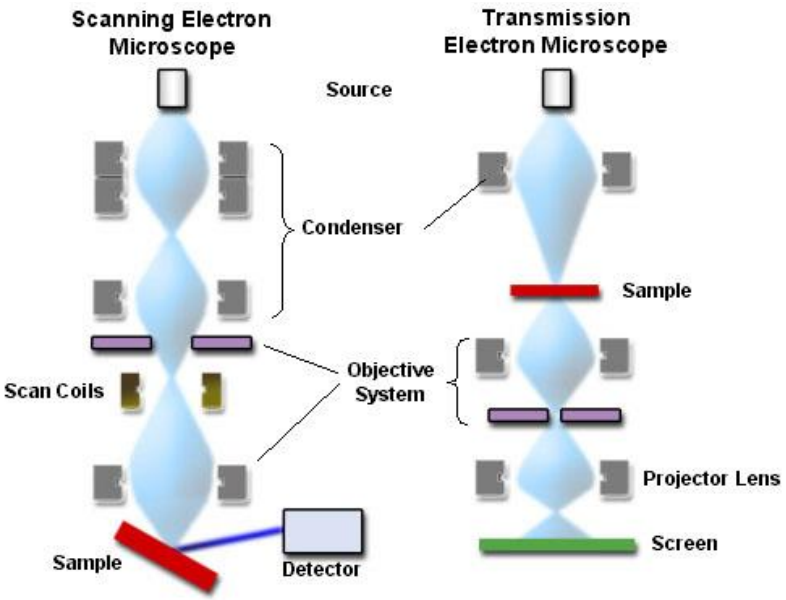

Fig. 2.7 A sketch of the internal configuration of a SEM (a) and a TEM (b). The main difference lies in the position of the sample in respect to the incoming beam.

In SEM the sample is positioned at the bottom of the chamber while in TEM the sample is located between the beam and the screen in order to collect the electrons. Therefore even the reconstruction of the image is different. As described in paragraph 2.1.2.1 in SEM, using SEs, it is possible to reconstruct a quasi $3D$ structure thanks to the depth of the field of the SE. For TEM, it is quite the contrary, the image is instead a $2D$ projection of the sample. However, the resolution of TEM enables users to "see" through the material allowing characterization of the crystalline structure. In terms of magnification, a SEM can magnify up to 1-2 million times with a spatial resolution of several nm while for a TEM the highest accessible magnification is 50 million times granting an extra order of magnitude in resolution $(0.5\ \text{Å})$.

2.1.3 Energy dispersive x-ray spectroscopy

As introduced at the beginning of the chapter, a material exposed to a high energy e-beam emits x-rays. These photons can be produced by two different effects, the Bremsstrahlung effect or by $e^- - hole$ recombination. In the first case, the conversion of the energy of the electron into radiation happens as a result of the

deflection and deceleration within the material. The spectrum generated is a continuous distribution of frequency up to the energy limit of the incident electron energy and commonly represents the background in an EDX spectrum.

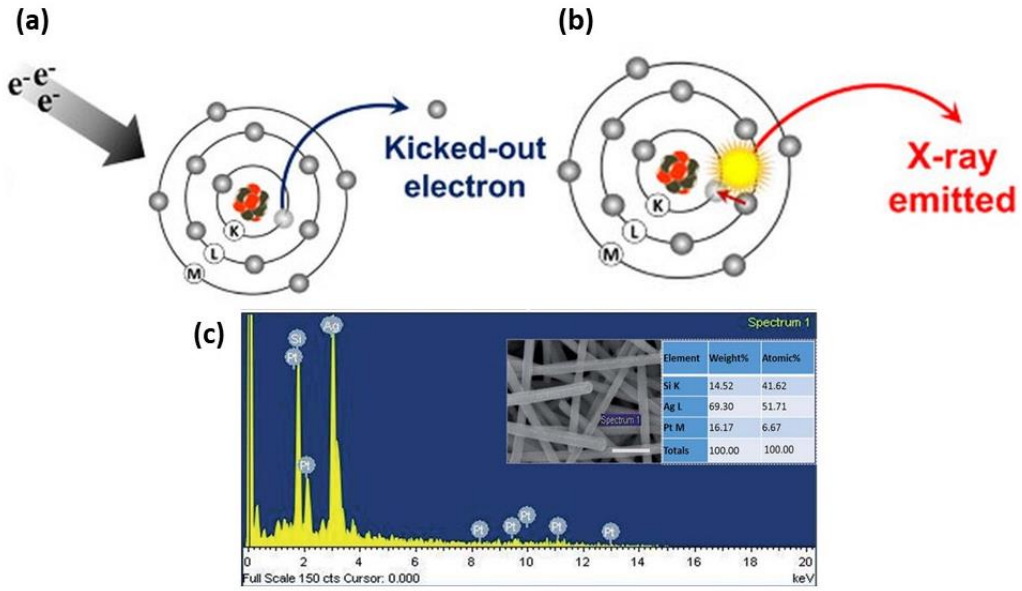

Fig. 2.8 A sketch that describes the interaction between a high electron beam and a specimen. In (a) an electron is kicked out from a K shell while in (b) an electron from an outer shell losses its energy to replace the electrons realising a x-ray photon. In (c) a typical EDX spectrum with the relative peaks related to different materials.

When an e^- beam is used to expose a specimen, inelastic scattering will create holes within inner electron orbital shells. In the recombination process electrons from outer shells fill the vacancies left by the scattering event releasing characteristic x-ray radiation. In order to maintain the conservation of energy, the photon generated by recombination must have an energy equal to the difference between the energies associated with the two states. As shown in Fig. 2.8 (a-b), a recombination between a K shell e^- knocked out by the beam and a L shell e^-that jumps to a lower energetic state. The energy of the exiting photons is $E_{phot} = E_{L-shell} - E_{k-shell}$ and represents a fingerprint energy of the different materials. Through an energy dispersive spectrometer the number and energy of the exiting photons can be counted and used to distinguish between materials as shown in Fig. 2.8 (c).

2.2 Nanofabrication

Today electronics have reached the few atom dimensions thanks to lithography [9–11]. A process that was originally developed in 1820. Nicephore Niepce first introduced lithography using an extremely simple photoresist, a bitumen layer that changes its physical properties after exposure to light [12]. The process itself was quite rough and extremely slow but the basic concept after 200 years remains essentially unchanged. Centuries of progress and billions of dollars have improved the process immensely reducing the time and enhancing the feature resolution.

This PhD project exploits a mix and match approach to realize nano-devices combining UV (Ultra Violet) lithography and Electron Beam Lithography (EBL). These techniques complement each other due to their own specific advantages and limitations. UV lithography is routinely used by semiconductor companies because of its speed and the scalability of the process. On the other hand, EBL requires more time for the writing process but has an incredible resolution and is commonly used to develop proof of concepts devices for research purposes. The process used to realize samples in the following chapters involves an initial step for the $\mu m - mm$ scale features using UV lithography. Secondly, an EBL step is used to make the connection directly onto the nanowire. In conventional lithography a light source, usually within the UV range, is used to expose the photosensitive material. In contrast to EBL, where instead an electron beam is used as a "small pen" to expose the desired part of the sample with a sub μm resolution. However in both cases the process is based on a photosensitive material, usually made of polymeric chains, that after the exposure changes its chemical properties. As summarized in Fig. 2.9 these materials can be divided in positive and negative photoresists. Positive resists have long chains that will break apart as results of the exposure, becoming soluble in particular solvents known as chemical developers. On the other hand, negative photoresists have shorter chains that will crosslink together after the exposure becoming insoluble in the developer. The developer will then dissolve (leave) the exposed part in the case of positive (negative) resists as depicted in Fig. 2.9.

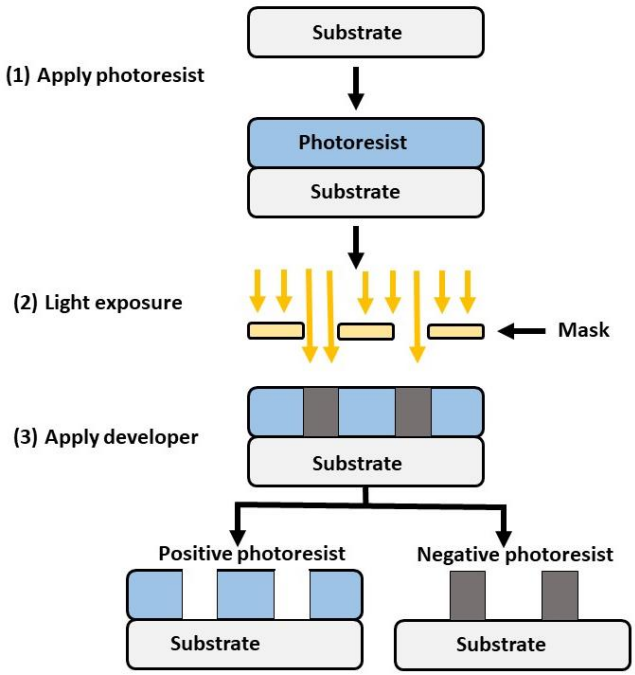

Fig. 2.9 Sketch that shows the main differences between positive and negative photoresist. After the exposure to the light the chemical bonds of the resists change becoming soluble to particular chemicals.

As mentioned before, UV lithography is used commonly by semiconductor companies thanks to its scalability. The strength of this technique comes from the fact that exposures are made with masks directly onto the sample. Very large areas can be exposed in a short period of time increasing the yield of the process. At the same time, the fact that UV lithography is a mask-based technique can be seen as a disadvantage. Nowadays, everything is calibrated to work with $300\ mm$ wafers, starting from the 50 cents plastic wafer holders to the new generation mask aligners which costs millions of euros. Intel have planned to invest $3.3\ B$ euro to move forward to a $450\ mm$ wafer process and to introduce extreme UV (EUV) as a light source to further reduce the spatial resolution [13,14]. The technique does not allow any change or flexibility in the usage. Possibilities that are instead given by EBL, a mask less technique that does not present any limitation on the exposed pattern. Sub-10 nm [15] resolutions are achievable thanks to the e^- wavelength. Unfortunately, a remarkable downside is the lengthy exposure and writing times. Firstly, the pattern needed for the exposure has to be designed using computer-aided-design software. After this, the exposure is performed on each single sample

making the entire process extremely time consuming. For this reason EBL is commonly used as research technique but not considered for mass production.

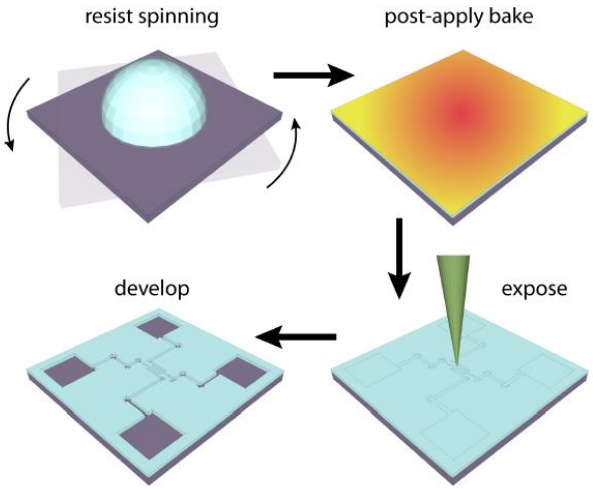

Fig. 2.10 Work-flow used to realize device through EBL. Initially a resist is spun on the SiO_2 substrate. A bake step is needed to cure the resist that subsequently will be exposed to the e- beam. Develop is then performed to remove the exposed part and prepare the sample for the metal deposition.

Fig. 2.10 describes the work-flow for UV lithography and EBL processes. Following, all the steps and recipes used for fabrication purpose are reported in detail. In the first instance a photoresist is spun onto Si substrate. A pre-bake step is required to reduce the solvent content and to harden the solvent avoiding contamination or sticking to the mask if present. The exposure is performed by shining UV light or an e^- beam onto the sample and lastly developers are used to remove the unprocessed resist.

2.2.1 Single and Crossed Nanowire Fabrication

UV lithography is used to realize the main electrodes shown in Fig. 2.11 while the connections made to nanowires are instead fabricated using EBL. In the latter case, high levels of precision are required since even a small misalignment of a few nanometres could result in an uncontacted device. For this reason, the SEM

column is equipped with a shutter that controls the exposure by quickly blanking or un-blanking the beam. Furthermore, prior to the exposure angle and position corrections are routinely performed to properly align the sample. Finally, using the alignment markers shown in the insets of Fig. 2.11 a final calibration is made before the exposure.

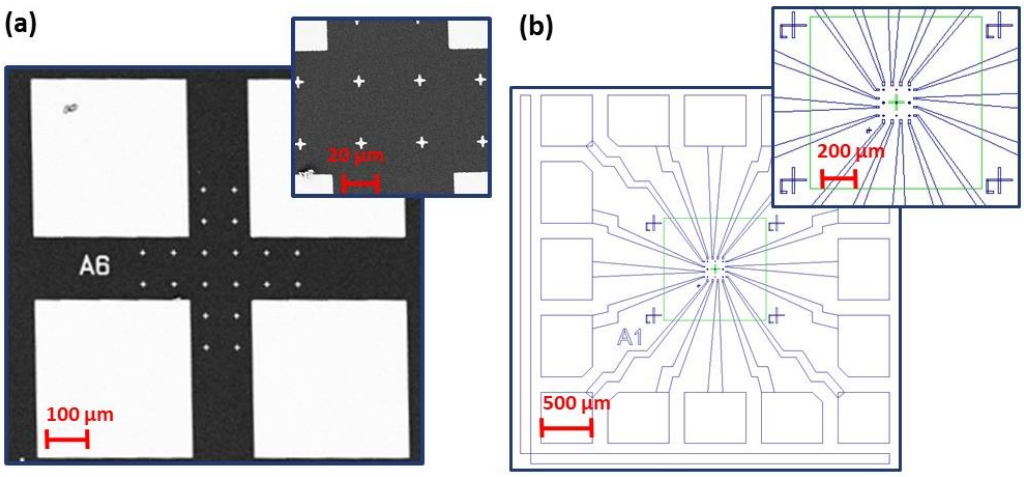

Fig. 2.11 In (a) *SEM* images that shows the Tarek mask with as inset a zoom of the region used to contact the nanowires. In (b) an image taken from the software used to design the electrode onto the sample. As before, a zoom can be seen as inset showing the alignment markers used to align the sample before the exposure.

UV Lithography Procedure

The standard procedure described below was routinely used to clean Si/SiO_2 substrates before any further process. Starting from the blank wafer, a $2x2\ cm^2$ chip is obtained by hand-cleaving or using Disco Automatic Dicing Saw DAD 3220. A sonication step is subsequently performed in acetone for 3 minutes, using a sonicator bath Elmasonic *P120H* at $37\ kHz - 580\ W$, to remove impurities from the chip. The substrates are then rinsed with isopropanol (IPA) and dried with a nitrogen gun. An extra pre-bake step at 150 ℃ for 1 minute is performed prior to spinning resist to remove adsorbed water molecules. A BREWER Spin Coater 200 Model is used to spin the positive photoresist $S\ 18 - 13$ onto the SiO_2. In order to obtain a uniform coverage of the surface the rpm are

increased in a stepwise way [16]. This is a critical step to obtain well defined and sharp features that will be used during the EBL exposure. An inhomogeneous resist layer could lead to an unfocused sample with consequent blurring effects of the resulting pattern compromising the device. Through an OAI UV mask aligner equipped with a Hg lamp the exposure is performed with a dose of $66\ mJ/cm^2$ for $5{,}5\ s$. Two masks with different layouts, shown in Fig. 2.11, were purchased from Delta Mask [17]. In principle, both the masks are designed for single wire devices but depending on the applications one will suit better than the other. The large working area between the main electrodes makes the tarek mask, in Fig. 2.11 (a), ideal for single wire or junction device. On the other side, the cryo mask Fig. 2.11 (b), is a more versatile version thanks to its 16 contacting pads that enable simultaneous contact to 4 or more nanowires, thereby optimizing the EBL writing time.

Table 2.2 UV lithography procedure used to obtain the main electrodes structure in Fig. 2.11 (a)

UV lithography procedure
1. Prebake at 150 ℃ to remove water molecules from the Si substrate 2. Spin $\mathrm{S18-13}$ positive resist at $5000\ rpm$ for $45\ s$ with $5\ s$ ramp at $500\ rpm$ 3. Soft bake at 115 ℃ for $75\ s$ 4. Expose to $365\ nm$ light for $5.5\ s$ (dose $66\ mJ/cm^2$) 5. Developing process using $\mathrm{MF319\ (Shipley)}$ for $45\ s$ and deionized H_2O to stop the process

After the exposure the sample is developed in a $\mathrm{MF319\ (Shipley)}$ solution to remove the unwanted S18-13. In doing so, the exposed parts will be removed and filled through a metal deposition. A TEMESCAL E-Beam Evaporator FC-2000 is routinely used to evaporate thin layers of metals such as Ti, Au, and Cu to produce the desired electrodes. A Ti/Au - $5/35nm$ deposition is usually used to establish the main electrodes on the chip. The Ti layer acts as adhesion layer between silicon

substrate and the deposited Au electrode. Ultimately, the lift-off process removes the unwanted resist by placing the sample into acetone for 12 hours.

EBL Procedure

A low concentrated solution containing nanowires is dropcast onto the UV-pre patterned substrate. A B-130 Leica optical microscope is used to locate the position of the nanowires with respect to the alignment marks, allowing the design of the electrical contacts through the Raith Multibeam software. Once the layout for the electrodes is completed the sample is ready for the exposure. A double layer resist technique is used to improve the resolution of the final structures [18]; this process was also used to avoid sticking effects at the interface between the drawn pattern and the resist. A Zeiss SEM supra is used to draw the desired pattern onto the chip for device fabrication. The interface software enables users to modify different parameters such as acceleration voltage, dose and apertures to improve the exposure process. The entire process used for the EBL is summarized in table 2.3.

Table 2.3 Procedure used for the EBL process. A double layer resists approach is used to improve the resulting features of the samples.

EBL Procedure
1. Prebake at $150℃$ to remove water molecules from the Si substrate 2. Spin MMA at $6000\ rpm$ with $120\ s$ bake at $180℃$ 3. Spin PMMA at $3000\ rpm$ with $180\ s$ bake at $180℃$ 4. EBL parameters: $10kV$ accelerating voltage, $30\mu m$ apertures, $8\ mm$ working distance and $130\ \mu A/cm^2$ *dose* 5. Metal evaporation performed with *Temescal FC2000 Metal Evaporation system* depositing $200\ nm$ of Ag 6. Developing process using *MIBK:IPA 1:3* solution for $45\ s$ and deionized H_2O to stop the process.

2.2.2 Nanowire Network Fabrication

As reported in the first chapter, a wide variety of approaches have been developed to deposit randomly oriented NWNs [19,20]. Techniques such as drop casting, bar coating or spin coating are not suitable since the randomness of networks is not ideal. In the first case, for example, a coffee ring effect is inevitably present after the deposition which compromises the quality of film. Furthermore, bar or spin coating will instead present preferential alignment due to shear forces. Spray coating has been highlighted from several reports [19] since it enables the creation of uniform randomness across the whole substrate. It is also a very common way to create network meshes and represents a very quick and easy deposition method. Moreover, the spraying mechanism technique is highly scalable and does not require any type of pre/post bake. Thanks to these qualities spray coating is used as the main technique across the entire project to realize nanowire network films. A dedicated spray robot equipped with a standard airbrush gun, shown in Fig. 2.12, is used to deposit the solution over a large area.

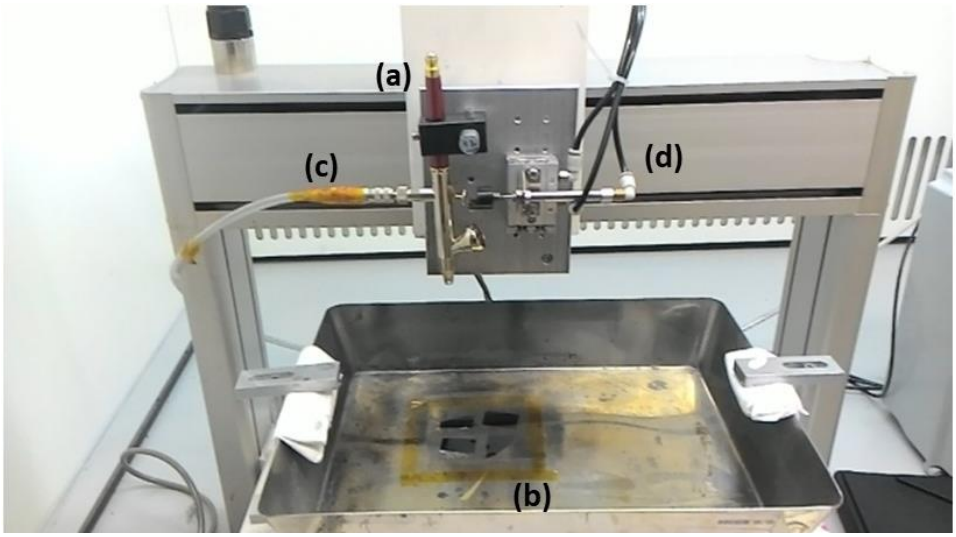

Fig. 2.12 Optical image of the robot capable of *10x10 cm* spray area. The spray-gun is shown in the picture as (a) while the actual samples placed before the deposition are in (b). In (c) the air inlet and in (d) the trigger used to open the valve and atomize the NWs solution.

The area selected is approximately $10\ x\ 10\ cm^2$ and in order to get a uniform coverage of the surface several ml of solution are sprayed. A SiO_2 wafer is diced and clean as reported earlier in section 2.2 and then attached to the holder with Kapton tape. The solution, containing IPA and nanowires, is inserted in the inlet and subsequently the trigger is pressed against the valve releasing N_2. Due to the high pressure the solution is atomised and sprayed towards the samples. At first, in order to optimize the deposition, several transmittance measurements were performed by spraying different amounts of solution. The standard procedure used to spray networks contains $150\ \mu l$ of Ag nanowire dispersed in $22.5\ ml$ of isopropanol (IPA). An example of transmittance experiment, using a quartz slide as substrate, is reported in Fig. 2.13 and the resulting transmittance within the visible spectrum is reported in table 2.4.

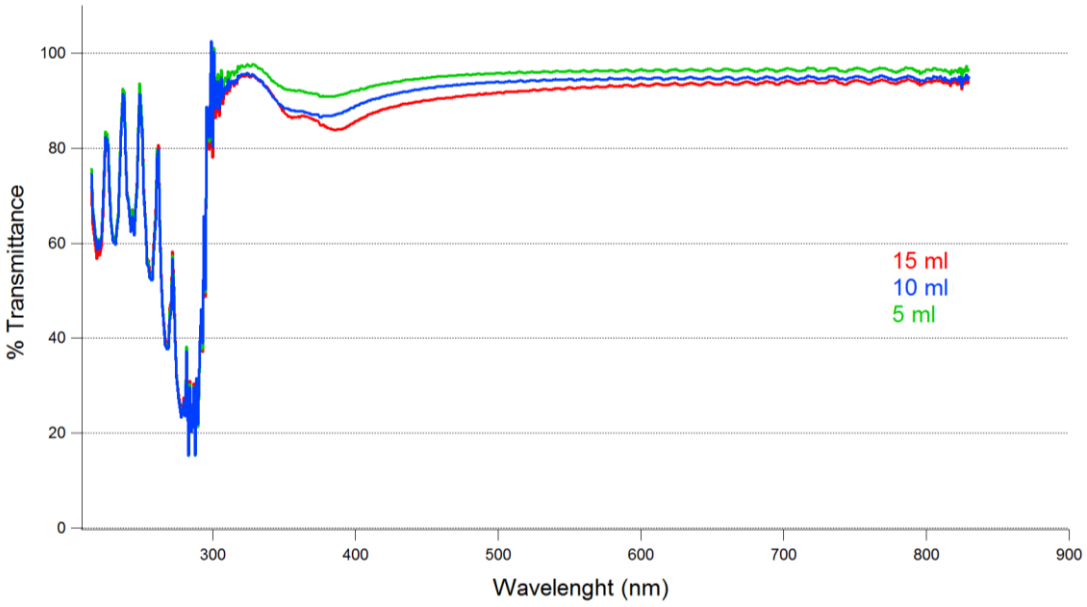

Fig. 2.13 Transmittance spectrum performed to relate the total transmittance of the sample in respect to the solution sprayed. The experiments were performed using a Perkin Elmer system.

Referring to the standards introduced in the first chapter in section 1.4.1 it is possible to note how the transmittance value match the optical requirements for transparent conductors applications [21].

Table 2.4 Transmittance values with regards to the total amount of solution sprayed.

Sprayed solution	% Transmittance (at 450 nm)
5 ml	*94%*
10 ml	*92.3%*
15 ml	*89.7%*

2.2.3 Electrode Deposition

Once the randomly oriented network is deposited onto the substrate, a metal evaporation is used to deposit the electrodes. The shadow mask based process is described in Fig. 2.14.

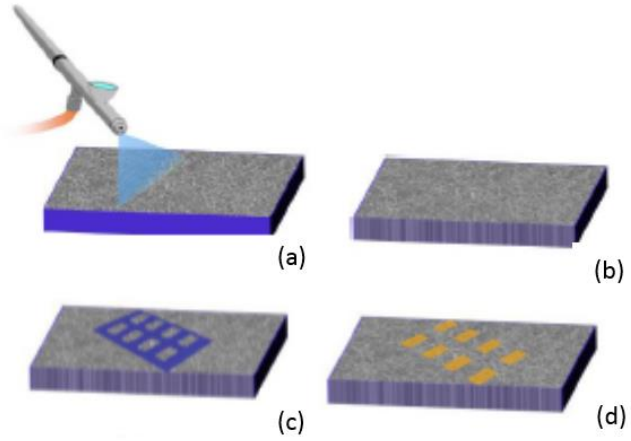

Fig. 2.14 Sketch of spray deposition technique (a-b) and electrode deposition using a shadow mask (c-d).

After the spraying process, shown in Fig. 2.14 (a-b), different shadow masks purchased from Delta Mask [17] are used to create the electrodes onto the network (Fig. 2.14 (c)). A Ti-Au metal deposition is performed using a Temescal FC2000 Metal Evaporation system. As before, a $5\,nm$ Ti layer acts as an adhesion layer with the SiO_2. The second deposition step, with $35\,nm$ of Au, covers the Ag nanowires improving the electrical contact between the network and the electrodes. The shadow mask used for the electrodes deposition has different

types of sizes ranging from $10\ \mu m$ to $1\ mm$ that were used during this study. A SEM image of an actual sample, a sketch and an optical image of the NWN are reported in Fig. 2.15 in which d represents the distance that separates the electrodes.

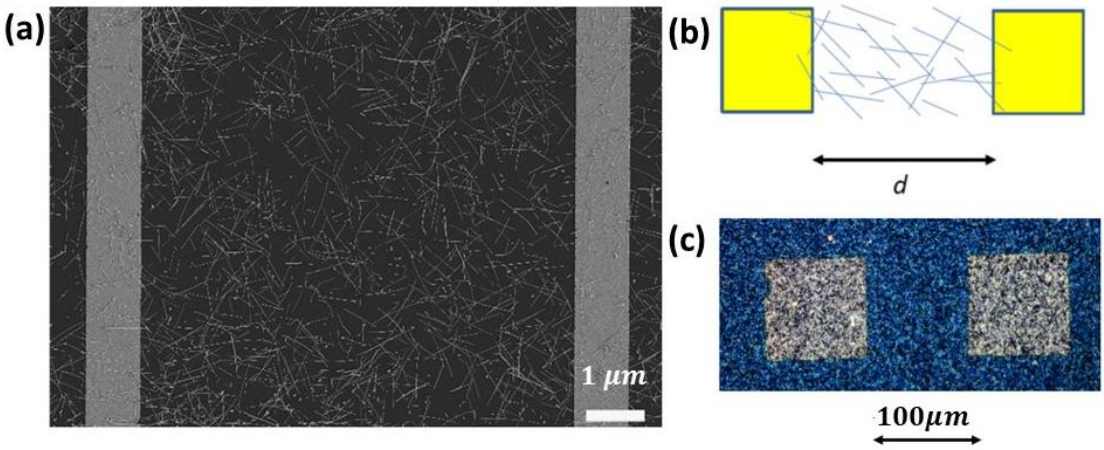

Fig. 2.15 In (a) a SEM image of an Ag NWNs with an electrode distance equal to $d = 7\ \mu m$ [22]. In (b) a sketch of a network and in (c) an optical image of an Ag NW network in which $d = 100\ \mu m$.

2.3 Nanowires

During the course of this project, several types of NWs have been used to tests the performances and the electrical behaviour of their corresponding networks. Ag NW ink purchased from Seashell technologies, was extensively used across the entire PhD duration to analyse the electrical response of NWNs. The main batch used for the realization of networks is the AgNW-60 that presents an average diameter of $60\ nm$. It is important to remark that through the experimental sections whenever referring to Ag NWs the batch to be considered is AgNW-60. If a different type of NWs is used it will be highlighted in the text.

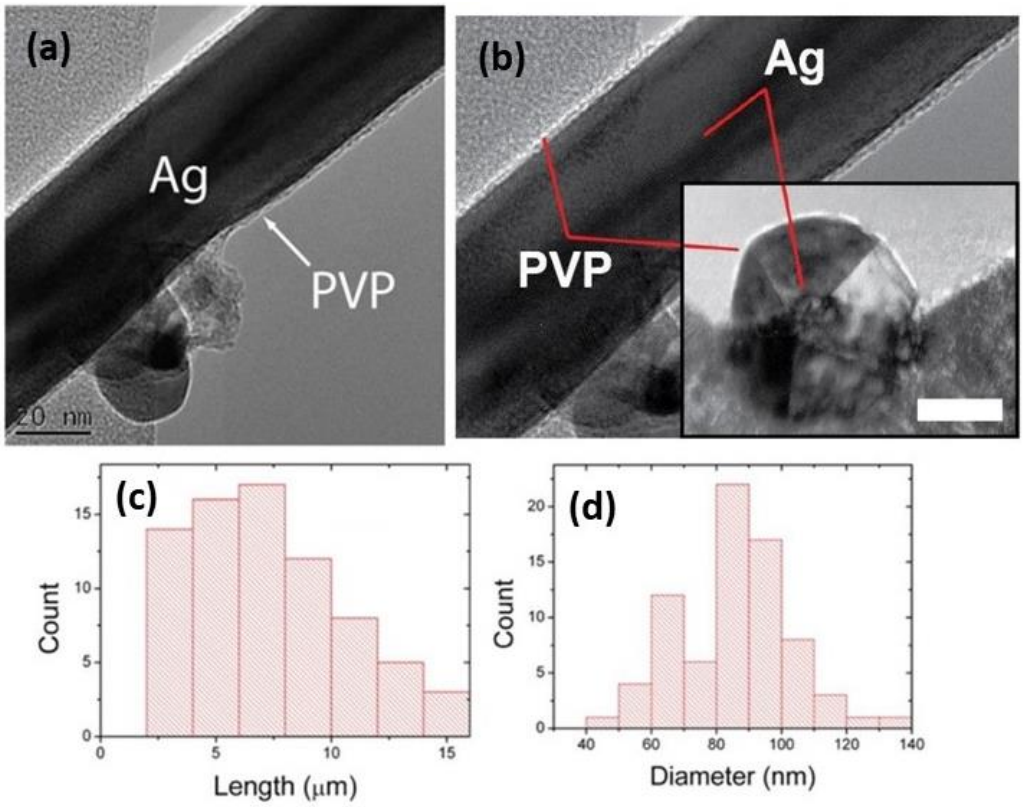

Fig. 2.16 *TEM* images of Ag NW where the contrast between Ag and PVP is clearly visible. In both the images the scale bar is $20\ nm$ while in the inset of (b) a TEM cross section image shows the pentagonally twinned structure of the Ag NWs. In (c) and (d) two histograms showing the length and the diameter respectively. The PVP coating layer is roughly $2\ nm$.

NWs as received are usually dispersed within an isopropanol (IPA) or water solution. However, as can be seen from the TEM images in Fig. 2.16 (a-b) Ag NWs are coated with a polyvinylpyrrolidone (PVP) layer. In the first place the role of these surrounding shells enable the growth of the Ag NWs during the synthesis process but it is also used to prevent NWs agglomeration. In Fig. 2.16 (c-d) two histograms show the length and diameter of the NWs obtained from statistical analysis performed on SEM images.

Moreover, from the TEM images it is possible to determine the thickness of the coating layer that fluctuates around $1\ nm$ and $2\ nm$. This might seem like a small variation, but from an electrical point of view it can lead to inconsistent results. Since the activation mechanism involves the formation of CF within MIM devices shown in section 1.3, a variation of a nanometre can dramatically influence the

activation voltage of the cell. This effect can create several problems from a modelling point of view. Therefore, to overcome this problem in all the simulations the thickness of the PVP, that is a critical parameter to describe the activation, is considered as a Gaussian distribution of thicknesses.

The second part of the project is instead focused at the study of different NWs materials to test different conduction mechanisms. The same considerations can be also made for other types of nanowire among which Cu, Ni or even other types of core-shell nanowires realised by our collaborators in Cork University. Examples of different NWs used during the PhD can be found in Fig. 2.17. In all the cases the external insulating layer is present and usually ranges from 2 to $10\ nm$ depending from the diameter of the NWs. The core-shell nanowire Ag@TiO_2 presented in Fig. 2.17 (a) has an external TiO_2 layer grown in solution [23] with thicknesses that fluctuates around $12\ nm$. In the latter case Fig. 2.17 (b-c), Ni/Cu with their respective oxides, the insulating layer is due to an oxidation process that naturally takes place when the NWs are exposed to the atmosphere.

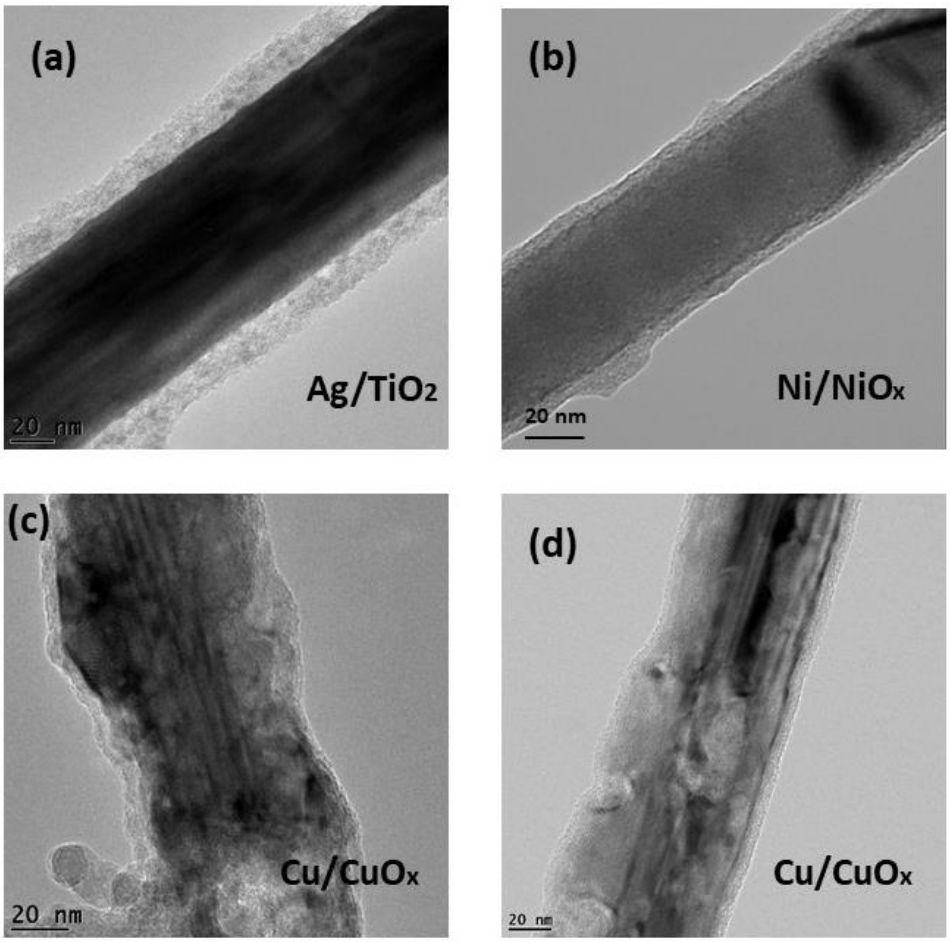

Fig. 2.17 *TEM* images of $Ag@TiO_2$ (a), $Ni@NiO_x$ (b) and $Cu@CuO_x$ (c-d). The $AgTiO_2$ NWs (a) produced through a thioglycolic acid mediated process have an average length of several μm and a coating thickness of $14.6\ nm$ [23]. Ni NWs (b) purchased from Nanomaterials [24] have an average diameter of $80\ nm$ and a length of $9.4\ \mu m$ [25]. The Cu NWs in (c) and (d) have an average length of $20\ \mu m$ and a diameter equal to $52\ nm$ [26].

It is interesting to note how the Cu NWs, synthetized by our collaborators in Duke University, undergo a smoothen process. In Fig. 2.17 (c) the drop-casted nanowires present a very rough surface that over the time (15 days) has been smoothened by a naturally oxidation process Fig. 2.17 (d).

2.4 Electrical measurements setup

Probing the characteristics of fabricated devices required the use of an electrical measurement unit. Two different setups were used for the acquisition of the results during this project. The first one, shown in Fig. 2.18 (a), is a Karl Suss PM-8 probe station paired with a Keithley 4200-S Source Measure Unit (SMU).

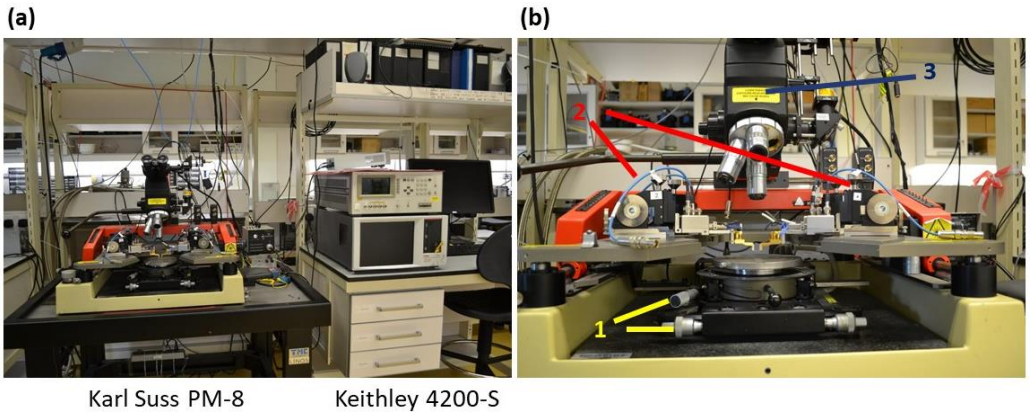

Fig. 2.18 The setup used to perform the electrical characterization of devices. In (a) the Karl Suss probe station on the left side and the Keithley on the right side. In (b) a zoom of the probe station shows the x,y manipulators in (1), the micromanipulators used to contact the samples (2) and the optical system (3).

The probe station, equipped with 4 Cascade Microtech micromanipulators, enable users to contact the electrodes on the Si substrates through Pt probe with a nominal diameter of $30\ \mu m$. A stage manipulator gives the possibility to quickly move across the samples while the fine adjustments are performed with micrometres equipped over each micromanipulator. A magnifying lens is used to carefully drive the probes onto the sample. All the connections between the Keithley 4200-S Source Measure Unit (SMU) and the physical devices are made with triaxial cables to reduce the noise level. Two current pre-amplifiers are also installed onto the Keithley 4200-S reducing the noise level to femto-ampere range. The Keithley software installed on the computer allows different sourcing methods supplying either voltage or current. It is therefore possible to set

parameters such as voltage/current steps, integration time to design different electrical tests.

The second system used is a cascade microtech REL-3200 probe station (Fig. 2.19) coupled with a Keithley 2450 source unit and a Keithley 2000 multimeter. Also in this setup, micromanipulators are used to contact the sample. The electrical connections are made with coaxial cables instead. Through GPBs, instruments are connected to the computer where a LabVIEW software is used to control the parameters for the measurements. Due to lower sensitivity of the 2450 source unit in respect to the 4200-S this system has a limited range of current and the noise level within the pico-ampere range.

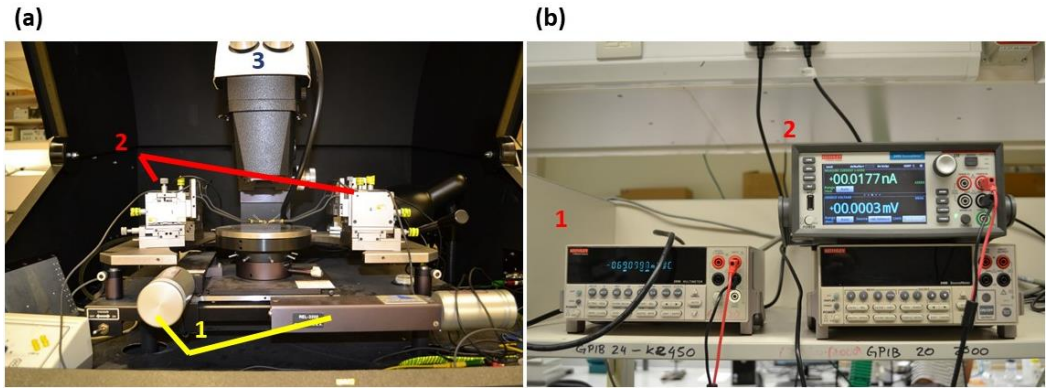

Fig. 2.19 The second system used to electrical tests the samples. Fig. 2.19 (a) shows probe station where the x,y manipulators are highlighted as 1, the micromanipulators as 2 and the optical system 3. The electrical setup shown in (b) is composed by a Keithley 2450 source unit 1 and a Keithley 2000 multimeter 2.

Electrical measurements can be performed using two different configurations. The first one, and perhaps the most common is the two point configuration. In this case the voltage (or current) is supplied to the device under test (DUT) and the signal collected is influenced by the connections of the entire circuit. In the second case a four point configuration also known as Kelvin probe method is used to obtain the resistance of the DUT neglecting all the electrical connections. In this case, the current is sourced as normal through the outer electrodes; the second pair of electrodes measures the voltage drop due to the sample only. This method is commonly used to eliminate the contribution of the connections and accurately measure the resistance of the DUT.

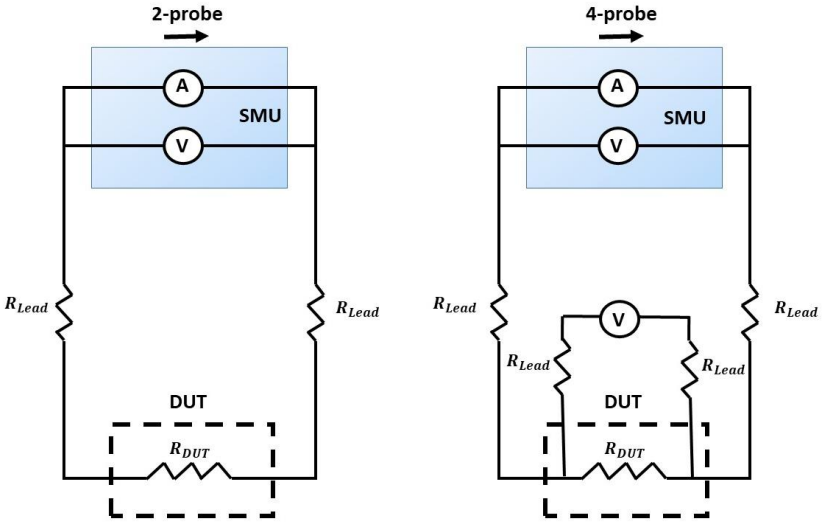

Fig. 2.20 Two (a) and four (b) points measurements. The first approach is used to run quick tests and obtain results in which the contribution of the cabling does not affect the output of the measurements. On the other hand, the second technique is widely used to perform more sensitive experiments when even a small difference in resistance drastically affects the results.

In the vast majority of the cases the two point approach is used to perform the biggest part of the electrical investigation on devices. Four point is instead utilized when an elevate grade of accuracy is required, for example in determine the junction resistance between NWs or the resistivity. In this case even a different of tenths of Ω can affect the results obtained from the electrical characterization.

2.5 Conclusion

This chapter has been used to introduce the readers to the working principles of the many techniques used in this thesis. The Scanning electron microscopy represents the main tool used that thanks to its ductility enables us to perform imaging and fabrication. Within the second part of the chapter all the fabrication details to realize contacts on single nanowires as well as large networks have both been described concluding the chapter with the setup used to characterize electrically devices. The next chapter is the first of three experimental chapters in this thesis, and introduce the measurement performed on Ag NWNs to understand the activation process.

References

1. Lane, N. The unseen world: reflections on Leeuwenhoek, (2015).
2. Abbe, E. Ueber einen neuen Beleuchtungsapparat am Mikroskop, (1873).
3. de Broglie, L. The reinterpretation of wave mechanics, (1970).
4. Suryanarayana, C. Microstructure: An Introduction, (2017)
5. Kanaya, K. & Okayama, S. Penetration and energy-loss theory of electrons in solid targets, (1972).
6. Tanuma, S., Powell, C. J. & Penn, D. R. Calculations of electron inelastic mean free paths, (2005).
7. Vanderlinde, W. Scanning Electron Microscopy. 559–573
8. Z. Gemmill, L. Durbha, S. Jaconson, G. Gao, K. weaver. SEM and FIB Passive Voltage Contrast, (2017).
9. C.Edwards, Lithography the biggest roadblock to Moore's Law, (2011).
10. Totzeck, M., Ulrich, W., Göhnermeier, A. & Kaiser, W. Pushing deep ultraviolet lithography to its limits, (2007).
11. Bjorkholm, J. E. EUV Lithography—The Successor to Optical Lithography?, (1998).
12. World, T. H. E. & Photograph, S. F. Re-discovery of the world's first photograph, (1952).
13. Mojarad, N., Gobrecht, J. & Ekinci, Y. Beyond EUV lithography: a comparative study of efficient photoresists' performance, (2015).
14. Younkin, T. R. Extreme-ultraviolet secondary electron blur at the 22-nm half pitch node, (2011).
15. Pi, S., Lin, P. & Xia, Q. Fabrication of sub-10nm metal nanowire arrays with sub-1nm critical dimension control, (2016).
16. Azadi, M. & Lopez, G. G. Spin Curves for MicroChem S1800 (1805, 1813, 1818) Series Positive Resist, (2016).
17. http://www.deltamask.nl/frames.html.
18. Gangnaik, A. S., Georgiev, Y. M. & Holmes, J. D. New Generation Electron Beam Resists: A Review,(2017).
19. Scardaci, V., Coull, R. & Coleman, J. N. Spray deposition of Silver Nanowire transparent conductive networks, (2012).
20. Langley, D. *et al.* Flexible transparent conductive materials based on silver nanowire networks: A review, (2013).
21. Scardaci, V., Coull, R., Lyons, P. E., Rickard, D. & Coleman, J. N. Spray deposition of highly transparent, low-resistance networks of silver nanowires over large areas, (2011).
22. Manning, H. G. *et al.* Emergence of winner-takes-all connectivity paths in random nanowire networks, (2018).
23. Manning, H. G., Biswas, S., Holmes, J. D. & Boland, J. J. Nonpolar Resistive Switching in

Ag@TiO 2 Core−Shell Nanowires, (2017).

24. https://nanomaterials.iolitec.de/en.

25. Nirmalraj, P. N. *et al.* Manipulating Connectivity and Electrical Conductivity in Metallic Nanowire Networks, (2012).

26. Rathmell, A. R. & Wiley, B. J. The synthesis and coating of long, thin copper nanowires to make flexible, transparent conducting films on plastic substrates, (2011).

Chapter 3

Activation process

As mentioned in the first chapter, the interest into $1D$ materials and especially for disordered networks has been limited especially with the advent of $2D$ materials. This limited interest is in part due to the fact that networks are often considered by the scientific community as a "bunch of resistors in series and parallel". Starting from this premise they are considered primarily for transparent conductor applications, so that reports on MNWNs have mainly focus on the optimization of the sheet resistance and transparency of the film [1–4], through the optimization of the network junction resistance. However, the true potential of networks has not been realised. The aim of this PhD project is to shine some light on the activation phenomena from a single junction point of view and to extrapolate this behaviour to the network itself. In doing this, we are going to prove that the activation of networks is a very complex process that involves different mechanisms. On top of that, we will first demonstrate that networks of different materials always scale in the same way and exhibit multilevel resistance states or memory levels with different retention times associated with them [5].

This chapter introduces the state-of-art activation processes for NWNs focusing on the most relevant examples. Following that, models and the assumption necessary to describe the activation of the NWNs from a theoretical point of view will be discussed. Moreover, the second part of this chapter will describe in details the approach used during this PhD project to combine the experiments and simulations results to describe the electrical activation of random NWNs. Finally, the formation of conductive filaments within the junctions of the networks will be discussed in terms of retention time and temperature dependency.

3.1 State-of-art

The state-of-the-art NWNs processing is mostly based on the bulk optimization of the sheet resistance of the films. This chapter aims instead to focus attention on the activation mechanism that has not been investigated before and through which we control the activation of parts of the network rather than its whole. Reports of Nirmalraj et al [6] and Sannicolo et al [7] have been chosen to set the background discussion on NWN activation which our work is based. The most relevant work made by Nirmalraj et al studies the activation of Ag and Ni NWN's introducing a very simple model that describes the activation as a cascade process. Due to a soft electrical breakdown, parts of the network activate under the application of an electric field. In doing so, the connectivity of Ag NWNs can be modulated obtaining a film with a tuneable sheet resistance.

The activation occurs through partial activation of the network area that presents an average radius $R_c = aV^{\alpha}$ as shown by the results shown in Fig. 3.1. V represents the voltage applied to the film for a short period of the time ($\sim 2\ s$), while a and α are fitting parameters. However, once the radius of the activated regions overcomes the separation between the electrodes, the network switches to the ON state. The power law behaviour is proven by a combination of experimental results obtained through Conductive Atomic Force Microscopy (CAFM) tests and simulations [6].

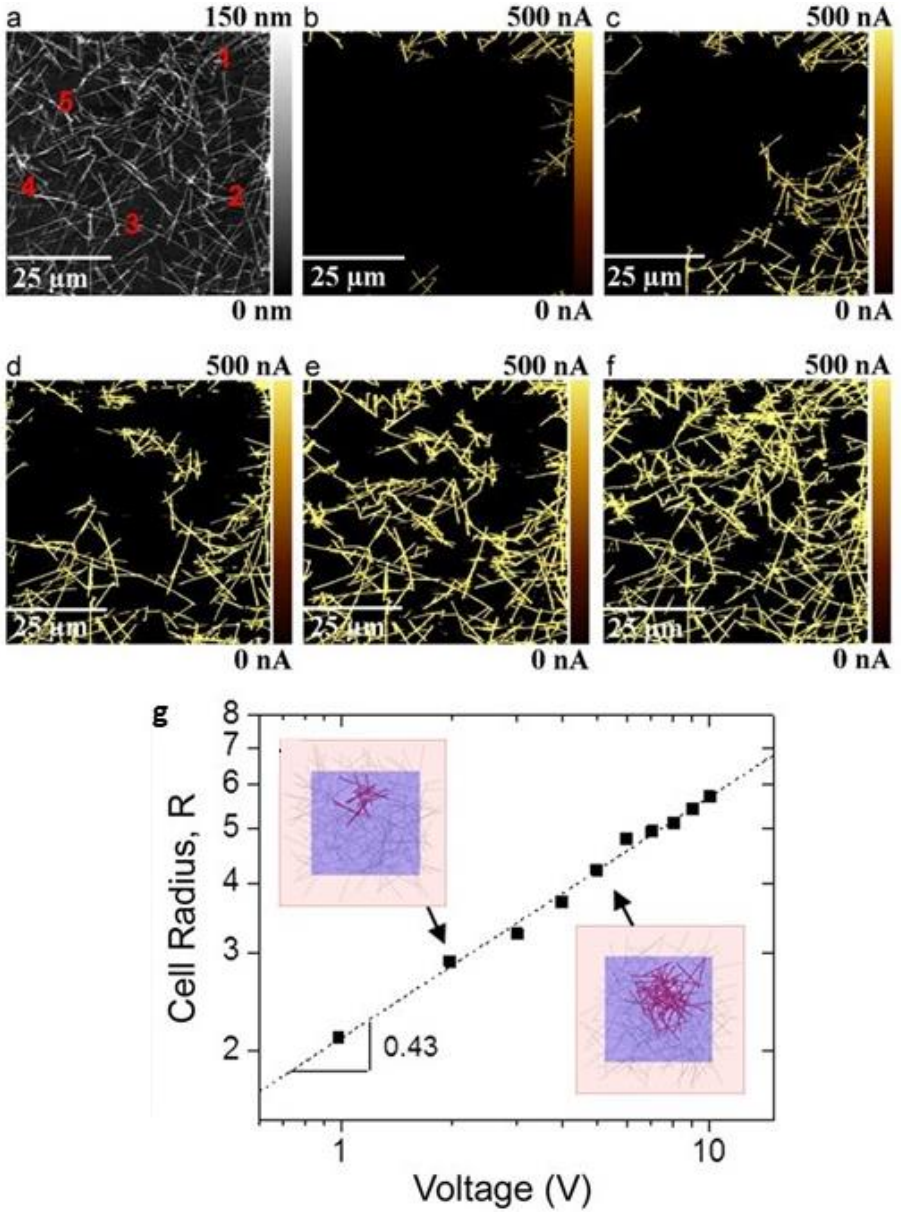

Fig. 3.1 In (a) a topography image of an Ag NW network. In (b-f) the tip of an AFM is used to activate areas of the network while in (g) a plot that shows the dependence between the radius of the cell in respect to the voltage applied [6]**.**

Fig. 3.1 shows in panels (b-f) the CAFM images performed on an Ag nanowire network. The conductive tip of an AFM is used in this study to selectively activate parts of the film applying a potential between the tip and the film. Fig. 3.1 (a) shows a topography image of the network as deposited. The numbers highlighted in red represent the tip-sample area contacted with the AFM tip along the different panels. In Fig. 3.1 (b) the tip interacts with the sample at point 1 in Fig. 3.1 (a). A voltage pulse of $6\ V$ is applied to the network for $2\ s$, and subsequently,

the imaging is performed with a low bias of $200\ mV$. The same procedure was then applied to the following points until the full optimization of the network is obtained in Fig. 3.1 (f). Using the model discussed, the simulation result in Fig. 3.1 (g) shows the power law trend that subsists between the radius of the activated area R_c and the voltage applied through the AFM tip to the sample. A second technique, Passive Voltage Contrast (PVC) [8], is used to further prove how the network under an electrical stress activates in a controlled way. Fig. 3.2 (a) shows the electrical measurements performed over a $50 \times 50\ \mu m$ Ag NW network [6]. In the inset of Fig 3.2 (a) the I-V curve shows explicitly this process; the system initially is in the OFF state (HRS- High Resistance State), but once the voltage reaches $0.9\ V$, the activation takes place and the system globally switches to the ON state (LRS – Low Resistance State). After the activation, it is possible to modulate the conductivity of the network driving the voltage without any current compliance. The passive voltage contrast image (cf. Fig 3.2 b) shows clearly the path created due to the I-V sweeps. As discussed in section 2.1.2.2, the nanowires that present a darker contrast are the activated ones due to the electrical voltage applied across the network.

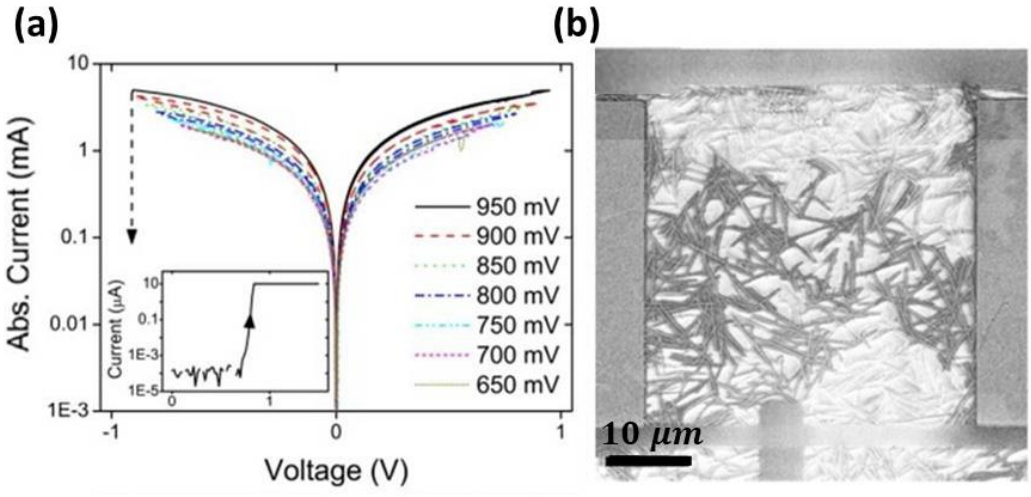

Fig. 3.2 Conductivity evolution of Ag NW network sequentially increasing the maximum voltage (a) with the activation as inset. In (b) a SEM image using passive voltage contrast technique to highlight the NWs electrically activated during the voltage sweeps [6]. It is also possible to note on the top and bottom part of the image (b) two FIB cuts used to confine the network.

Another important report by Sannicolo et al [7] visualizes the formation of different electrical paths within Ag NWNs using a Lock-in Thermography (LiT) technique. This technique is commonly used to detect the electrical faults within electrical parts or circuits monitoring the thermal response under electrical stress. With an accurate calibration of the apparatus to collect the thermal spectrum, it is possible to physically visualize the formation of different Electrical Percolating Paths (EPPs) within networks. In this study, wider networks, usually several mm wide, are spray-deposited as described in section 2.2 and contacted with Ag paste. A TEM image of an as-deposited junction is shown in Fig. 3.3 (a) and clearly shows the two different materials, the external PVP layer of few nm and the internal Ag core with a $45\ nm$ diameter.

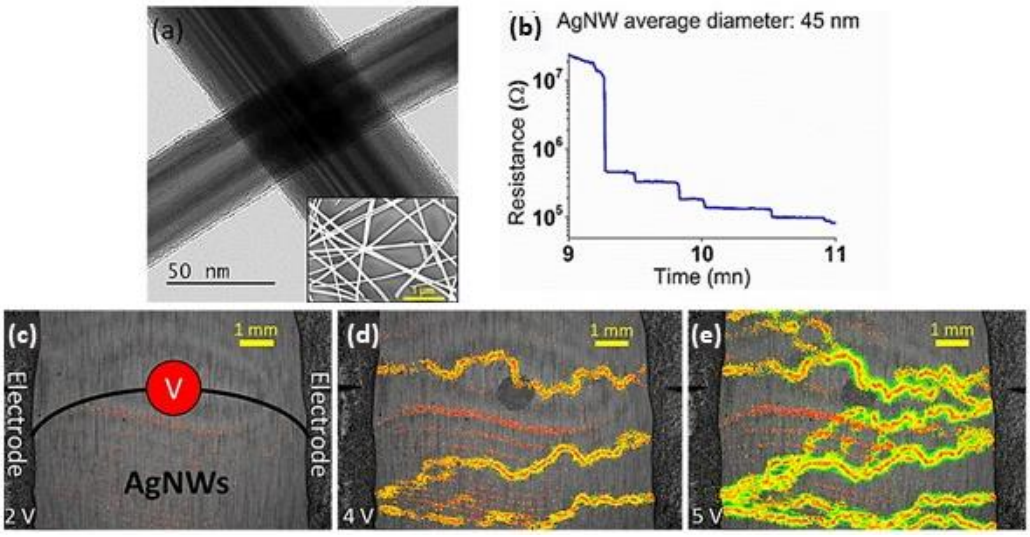

Fig. 3.3 In (a) a TEM image of a junction made of Ag nanowires while in (b) the activation of the network is followed by the resistance behaviour over time. The LIT technique is used in (c-e) to highlight the formation of percolating paths within the film [7]**.**

Fig. 3.3 (b) shows the resistance behaviour during the activation of the film, while in Fig. 3.3 (c-e) the formation of the electrical paths in the network is highlighted through the thermal trace of the NWs carrying the current. Specifically, in Fig. 3.3 (c) it is possible to recognize the formation of the initial path at $2\ V$. As the voltage applied increases, several other paths start to emerge until the full optimization of the film is reached. Fig. 3.3 (b) shows, through the resistance behaviour, the

evolution of the conductivity of the film. Remarkably, it is possible to see several steps in the resistance curves, which according to the authors are related to the quantized percolation paths. Following Landauer theory of quantum electron transport [9], it is possible to see this behaviour when the charge carriers are confined in small constrictions resulting in conductance levels that are multiples of the quantum unit of conductance $\Gamma_0 = 2\,e^2/h$. This is basically related to the short Fermi wavelength and conductance restrictions in NW junctions that naturally lead to quantization effects.

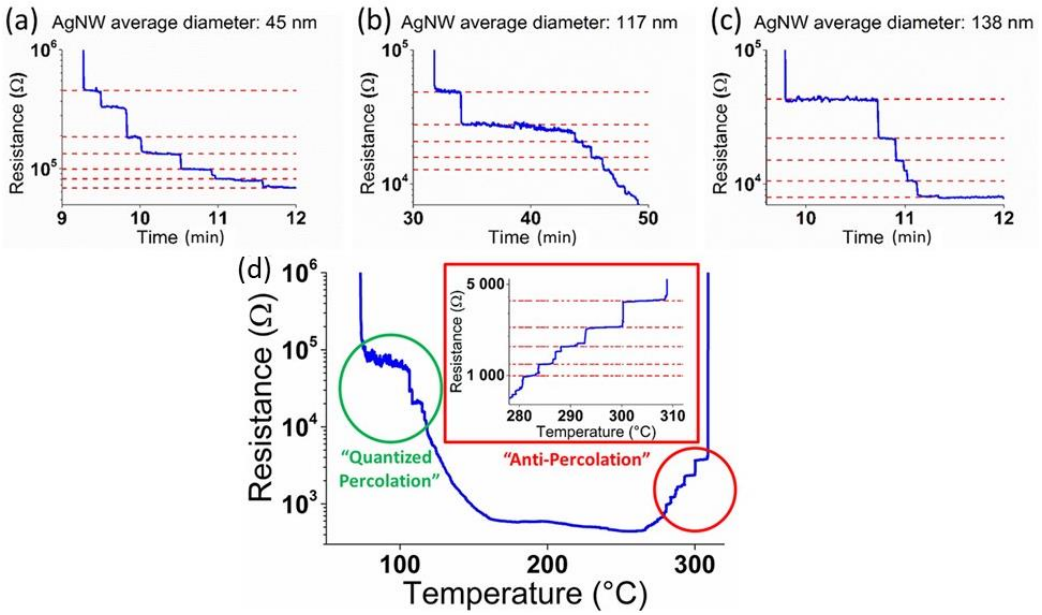

Fig. 3.4 The same approach used in Fig. 3.3 (b) is used to prove that the quantization occurring within networks is independent from the diameter of the NW used (a-c) used to realize the networks [7]. In (d) the behaviour of the resistance when the temperature of the substrate is ramped up causing the anti-percolation of the film [7].

Fig. 3.4 (d) shows also an anti-percolation process. The resistance is measured by applying a constant voltage to the network while ramping the substrate temperature up to 300°C degrees. Once again the trace shows several steps due to the thermal welding of the junctions highlighted in green. This optimization process lasts for a wide range of temperature until approximately 270°C degrees the resistance starts to increase again due to degradation of the NWs. Remarkably,

even in the anti-percolation case, the stepwise is observable and as highlighted on the inset of Fig. 3.4 (d).

Exploiting these types of behaviour we will show in this chapter that through a proper activation it is possible to obtain films that provide tuneable conductivity.

3.2 Proposed model for the activation

In 1973, Kirkpatrick used the Effective Medium Theory (EMT) to describe the transport properties of an inhomogeneous propagating medium [10]. With this theory, it is possible to describe and solve a wide range of physical problems such as transport of water or current through randomly oriented systems or even the heat or pressure propagation within mediums. Additionally, Kirkpatrick introduced a model to describe the transport within a random resistor network near and far from the percolation density limit [10]. Exploiting this, we propose a combination of the Kirkpatrick's EMT with Green's functions to characterize the conduction mechanism within NWNs of different materials [10]. The contribution of the intrawire resistances will be taken in considerations in the calculation of the sheet resistance improving considerably the match between the experimental results and simulations.

3.2.1 Junction Dominate Assumption (JDA)

The simplest approach to simulate the behaviour of disordered resistive networks is to use the Junction Dominate Assumption (JDA) [11]. This is a model that enables the calculation of the sheet resistance of a randomly oriented network neglecting the contribution of the intrawire resistance. This assumption can provide reasonable results for materials that have sufficiently high junction resistances such as carbon nanotubes (see table 3.1). For systems such as metallic nanowires, this condition is not valid anymore since the intrawire resistance is comparable or

even larger than the junction resistance itself. The estimation of the sheet resistance of the film is therefore systematically underestimated using JDA.

Table 3.1 Resistance values for junction and intrawire contributions associated to different materials. The inner resistance is calculated at room temperature with a fixed diameter $d = 50\ nm$ and length of the wire $l = 10\mu m$.

Material	Resistivity $(n\Omega \cdot m)$	Junction resistance	Intrawire resistance (Ω)	Reference
C	$5.22 \cdot 10^5$	$50\ k\Omega$	2.6×10^6	[12]
Ag	15.9	$11\ \Omega$	81	[13]
Cu	16.8	$205\ \Omega$	85	[14]
Ni	62	$705\ \Omega$	315	[15]

3.2.2 Multi-Nodal Representation (MNR)

In order to mitigate against the limitation of the JDA, a second way to calculate the sheet resistance is the Multi-Nodal representation (MNR) [11]. This alternative method aims to incorporate the contributions of the intrawire resistance. Thanks to a direct comparison between the experimental results and the simulations, this more complete procedure developed by our colleagues led by Ferreira (TCD) enabled the digitalization of the networks directly from SEM images to have a direct correspondence between experimental and simulation results. After the initial mapping step is performed the simulation through the MNR can be run to calculate the sheet resistance of the network. Therefore, it is essential that networks are not too dense but with enough wires to allow percolation between the electrodes as shown in Fig. 3.5 (a). Knowing the conductivity of the nanowire material, length and diameter of the wires, it is possible to calculate the sheet resistance and through the simulation make a direct comparison with the experimental results. The workflow is summarized in Fig. 3.5, an Ag nanowire network is used to perform the electrical measurements [13]. The same network is then digitalized from SEM images and simulations are run to extrapolate the resistance of the film. In Fig. 3.5 (c) the simulated sheet resistance R_S is plotted

with respect to the junction resistance R_j. The following parameters were used to perform the simulation. The Ag NW resistivity $\rho = 22.6 \pm 2.3\ n\Omega m$ is obtained from four-point measurement (see section 2.4) while length and diameter are directly extrapolated from the SEM images. The horizontal black line represents the sheet resistance $R_S = 42.9\ \Omega/sq$ acquired from the experiments for the network shown in (a). Note from Fig. 3.5 (c) that the R_S obtained from the JDA results (blue line) is lower compared to the MNR prediction (green line). The intersection between the experimental and simulated R_S shows how the JDA model tends to overestimate the junction resistance. The two values of R_j identified from the green circle for the MNR and orange square for JDA are respectively $52.91\ \Omega$ and $96.9\ \Omega$. Values that, according to the junctions resistance distribution presented in [16], confirm the fact that JDA overestimate R_j. Both the JDA and MNR can be considered as tools that enable the description of the junctions and if correctly implemented can enable the characterization of the activation process within networks. Depending on the type of the material used, one model will suit better than the other. An easy distinction can be made on the validity of the assumptions that have to be made in both approaches. For example, a network created using carbon nanotube can be easily described by JDA. In fact, CNTs are ballistic conductor and performance is dominated by the network junctions. On the other hand, MNR will describes more effectively networks made of nanowires with a low junction resistance and particularly networks that are being optimised through a controlled reduction of these junction resistances. There is an intermediate region, i.e. for Cu or Ni nanowires, where both the JDA and the MNR can be used.

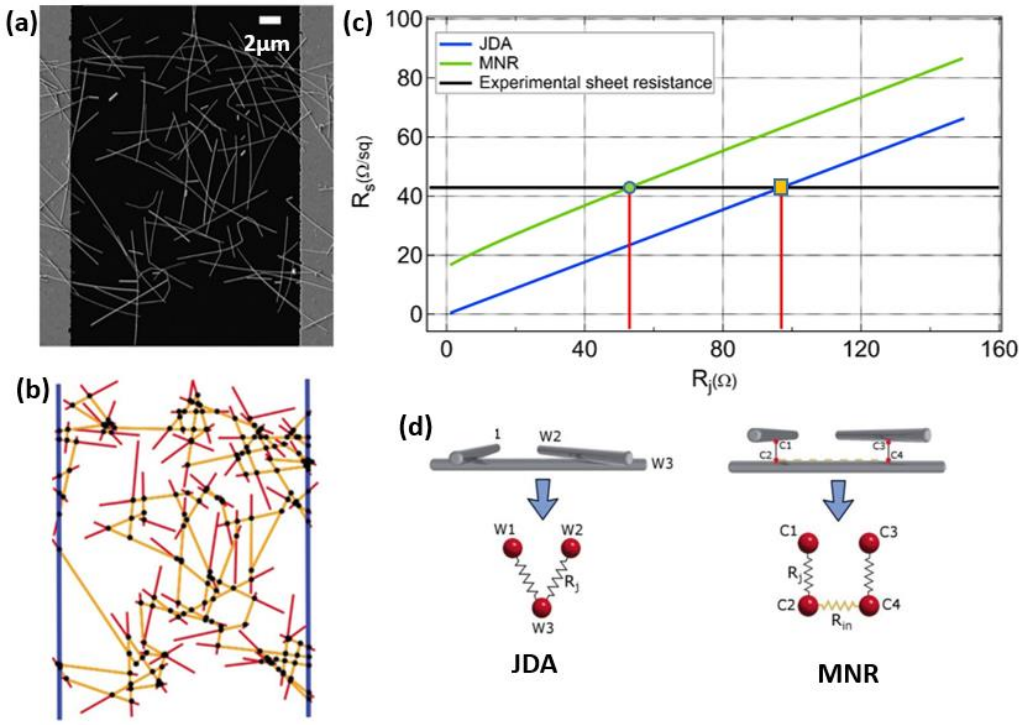

Fig. 3.5 SEM image of an Ag NWN (a) and the relative digitalization of the same network (b). Fig 3.5 (c) shows the comparison between the JDA and MNR in terms of the sheet resistance. The plot highlights the fact that the JDA systemically underestimate the simulated sheet resistance. On the other hand, the value obtained from the experiments (black line) helps to understand how the JDA tends to overestimate the junction resistance in order to compensate the sheet resistance. The circle and square that cross the experimental data line indicates the estimated junction obtained from the JDA and MNR respectively. Fig 3.5 (d) schematizes the junction mapping for the JDA and MNR modelling used to describe NWNs [13].

The further step required to describes the activation of NWN is to implement the JDA or MNR into the model for the simulations. This can be done linking the two representation introduced so far (JDA and MNR) and the two models, capacitance and memristor, used to describe the different activation conditions. It will be proven that in the initial stage of the activation, when most of the junctions are in the OFF state, the JDA describes in detail the activation steps. However, when the network became partially activated the JDA is not able to follow the film evolution and the MNR provides a better description.

3.2.3 Capacitance model

As introduced earlier, SEM images of the networks are used to create a digitized mapped network in which the simulations are run. Each junction, or edge, within the network is converted into a matrix where each node is represented by a capacitor that initially is in the OFF state. The capacitance associated with a junction connecting nodes n and m within the network can be calculated as $C_{n,m}^{0} = \varepsilon_r \varepsilon_0 A/d$ where ε_r and ε_0 are the permittivities of the dielectric and air, respectively, A is the area of the plates and d is the distance between the metallic plates. Considering for example an Ag@PVP nanowire, the parameters used for the simulation are therefore the electrical permittivity of the PVP $\varepsilon_r = 2{,}5$ and geometrical factors extrapolated from SEM and TEM images [11]. The distance d can be easily considered as two times the thickness of the coating layer shown in Fig. 2.16. The contacting area between two nanowires can be calculated assuming an ideal square area projected by the two touching NWs. The diameter, from the SEM images, ranges from $60 - 80\ nm$ giving C_0 values $10 - 18\ attoFarads\ (aF)$. Initially, all the capacitors present within the network are in the OFF state. During the simulation, a potential V is applied to the whole network. A charge Q will build up due to the potential onto the capacitors close to the sourcing electrode. If the charge Q_i on a generic node is high enough the considered capacitance switches to the ON state. The charge is subsequently free to flow through the activated junction inducing a certain number of avalanche events. The charge Q is incremented by ΔQ in the second iteration only when all the transition between the ON and OFF state ceases within the first iteration. Once an electrical path is formed between the electrodes the simulation can be stopped or eventually proceeds to allow further junctions activation within the network.

3.2.4 Memristive model

The second model utilized to describe the activation of the networks is the memristive model. It has parallels with the capacitor model but also considers

current flow and the evolution of the conductance of the network. To start, the initial preparation step (digitalization of the real network) is always performed thanks to the SEM image enabling a direct comparison between the experiments and simulations. Even in this case a matrix is formed as described in the capacitive model but this time Kirchhoff equations are instead used to distribute the voltage across the network. The main difference lies in the fact that each node is replaced by a memristor cell rather than a capacitor. The metal-insulating-metal (MIM) interface is created between the internal core of the nanowires and coating shell that acts as an insulator. Depending on the material used as coating, a wide range of properties can emerge. Within the memristive model, the activation process of the junctions is described by the formation of the conductive filaments (CFs) within the insulating layer. The variable-gap model, discussed in section 1.4, helps to understand the different mechanisms regulating the charge motion through junctions. A combination of tunnelling and ionic current, as depicted in Fig 1.11 (a), is responsible for the current flow and the activation of the junctions. Furthermore, during the simulation, the same iteration scheme is used for the memristive model. At first, a charge Q is injected through the electrode and is distributed across the network thanks to the junction matrix. Once the system reaches a steady condition where no more junctions are activated for that particular charge the next iteration injects more charge. The formation of an electrical path between the electrodes usually coincides with the end of the simulation. However, as for the capacitance models, a further injection of charge may cause additional junctions or paths to connect to this main path further lowering the total resistance of the film.

The memristive model provides a broader scope to describe the evolution of networks, we show in chapter 4 that the capacitance model describes well the initial stage of the activation. On the other hand, once the main path is selected within the network the capacitance model partially lose its effectiveness. This reflects the fact that the junctions, considered as capacitors, abruptly switch from OFF to ON states forbidding any tunability of the resistance. Once in the ON state the junction become resistor that can flow charge. On the other hand, the

memristive approach fails at the initial stage due to the high resistances of the junctions at the early stage of the activation.

3.3 Electrical characterization

This section points to illustrate all the different experimental approaches used in this study to understand the activation in NWNs. The first part is mainly based on the application of voltage sweeps to the film. In the second part we show how the application of current sweep help to see the problem from a different perspective understanding the mechanism beyond the current transport across NWs.

3.3.1 Activation study – sourcing voltage

One of the first experiment performed on an Ag NW network AgNW-60 is shown in Fig. 3.6. The electrical characteristic of the network ($d = 1000\ \mu m$) is tested by applying voltage dual sweeps with a positive bias following the scheme $0\ V \rightarrow V_{max} \rightarrow 0\ V$. The negative bias part is omitted in this study because the PVP layer between nanowires does not allow any switching effect [17]. For this reason, in describing the evolution of the activation in network we limit our investigations only using one voltage polarity.

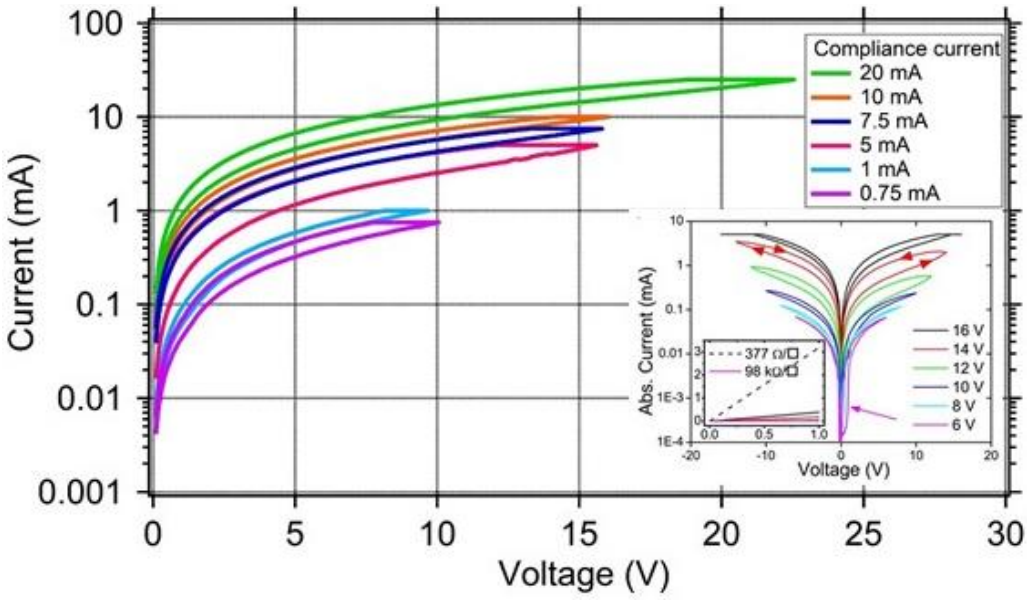

Fig. 3.6 Direct comparison between the results shown in [6] and experimental results obtained on another network sample of the same size.

Fig. 3.6 shows the electrical behavior and the consequent evolution of an Ag NWN. From a quick comparison with the results presented by Nirmalraj et al [6], reported in Fig. 3.6 as inset, one can identify the same non-linearity in the current evolution. The major difference between the two experimental approaches relies on the use of a compliance current while sweeping the voltage. In the studies performed by Nirmalraj et al [6], after an activation step, the conductivity of the network was manipulated by increasing the voltage applied to the device. However, in our case the use of the compliance acts in a similar way modulating the total resistance of the system. Therefore, consistently with the hypothesis introduced by Nirmalraj et al [6] in this regime we think that the conductivity evolution is dictated by the joining of the closest junctions and wires to the main conducting path.

Constant applied voltage

A second type of experiments designed to further analyse the resistance evolution of Ag NW networks is shown in Fig. 3.7. A constant voltage is applied to the sample and the current is collected over a large time interval. Specifically, $10.5\ V$ were supplied to a network with $d = 1000\ \mu m$ through silver paste contacts for 22 hours in order to test the activation in different conditions. Instead to increase the

electrical stress supplied to the system we decide to maintain constant the stimulus applied to the network monitoring its response over the time.

Therefore, referring to the current trace shown in Fig. 3.7, we have an initial condition in which the network is in the OFF state and no electrical connection is formed through the film. After two hours of constant voltage applied the current starts to flow and the system globally switches to the ON state with an abrupt jump in the current of four orders of magnitudes. At this particular point, we think that the main electrical path is formed between the electrodes enabling the conduction within the film. However, following the evolution of the current in Fig. 3.7 can be noted how a steady state is still far from being reached. The electrical optimization of the network, strengthening of the main path and joining of the closest junctions, requires over seven hours to be completed. In this particular situation, the conductance state of the film is not perturbed by the electrical stress applied for a long period of time. The steady state condition is interrupted around 16th hour by a sudden jump in the current (see inset in linear scale) that is most likely due to the electrical activation of an inactivated area close to the main path.

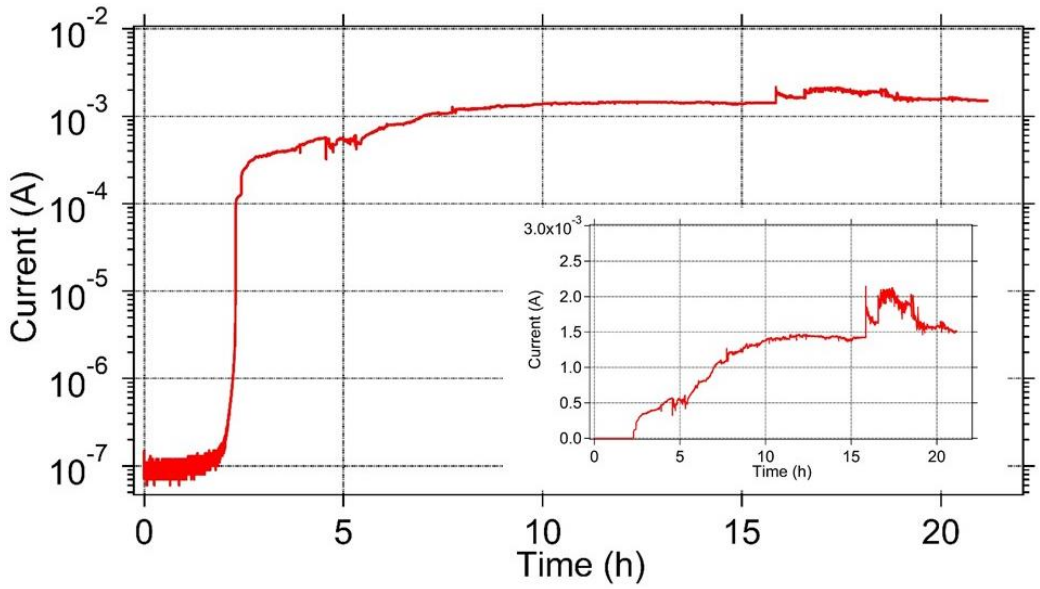

Fig. 3.7 Long time activation of a $1000\ \mu m$ Ag NW network with the application of a constant voltage of $10.5\ V$. The sample is contacted through Ag paste contacts [11]. The current scale is changed to linear in the inset to better show the presence of the peak around 16 hours.

In terms of physical interpretation, this behaviour in which areas of the network suddenly activates due to the electrical stress resemble the activation process as described by Nirmalraj et al [6]. However, following the approach proposed by O'Callaghan et al [11], we can extrapolate information regard the activation process analysing a portion of the current trace of Fig. 3.7. Inspired by the work proposed by Avizienis et al [18] on Ag_2S NWNs, we perform the Fourier transform of the current signal shown in Fig. 3.8 (a) (portion of the current trace of Fig 3.7) obtaining information about the connectivity evolution of the film. The motion of the Ag ions induced by the potential applied creates conductive filaments within the junctions that act as an atomic switch across the entire network. The formation of atomic switch junctions expands the degree of correlation in current fluctuations producing a $1/f$ behavior that can be associated with the joining of neighbour NWs to the main electrical path exactly we hypothesized earlier.

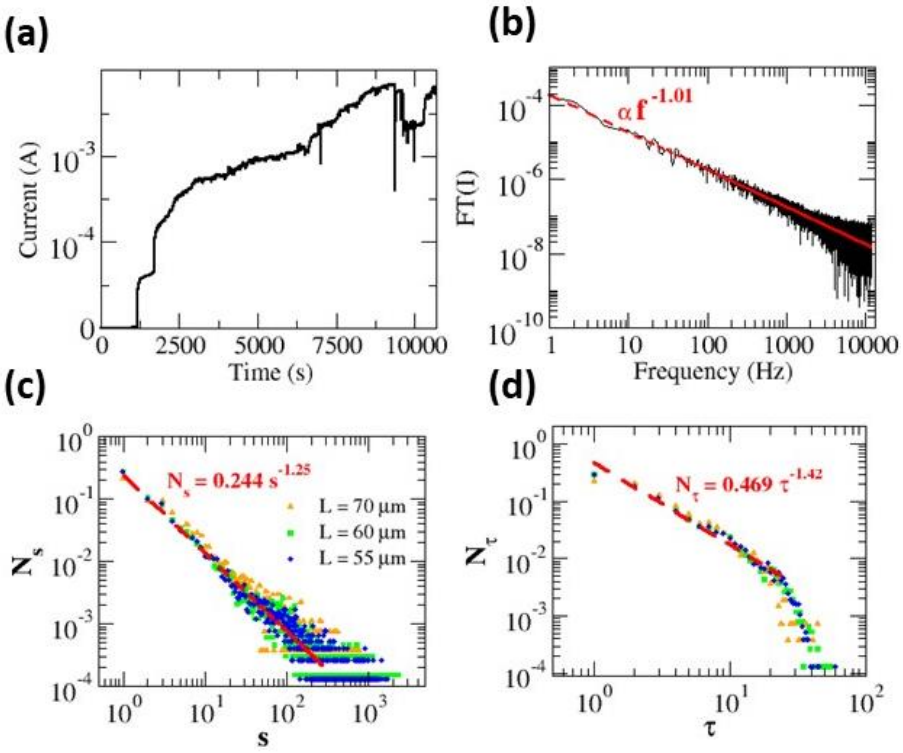

Fig. 3.8 The current signals shown in (a) is a portion of the I-V curve shown in Fig. 3.7 obtained from a $1\,mm$ network submitted to a constant $10.5\,V$. Through a Fourier transformation the signal is converted in a frequency spectrum that as described by Avizienis et al [18] can be used to describe the connectivity evolution within networks. The fit done shows a power law behaviour with an exponent very close to 1. In (c-d) the probability of an activation event in respect to the avalanche duration τ and the avalanche size s [11].

Moreover, addressing the problem using the capacitance model, we are able to describe the probability of an activation (avalanche) event with respect to the size event s (number of junctions involved) and the avalanche time τ respectively. In the scheme used we define an event when a capacitor, under the effect of the voltage, passes from the initial OFF state to the ON state. Therefore, injected into the network a ΔQ of charge (minimum charge step used in the simulation) it is possible to have 0 event when no capacitors are broken down, an event when only one capacitor activates and so on. Therefore, looking at the results presented in Fig. 3.8 (c-d) we see that the probability, N_S or N_τ, is higher considering the activation of small areas (small s in Fig.3.8 (c)) but it decreases very rapidly on events involving the activation of wider regions (large s). Similarly, considering the

integration time τ as the time required to complete an iteration within the simulation, we have a higher probability for events requiring few iterations while event that requires more iterations are very unlikely to happen.

3.3.2 From macro to microscale.

Although the activation at network scale can be described with the capacitance model there are still several aspects of the activation that we are not taking in consideration. So far, the activation has been considered as a cascade event where large portions of the network activate simultaneously under electrical stress. However, the experimental evidences reported by Sannicolo et al [7] point to a different activation mechanism. In fact, when sufficient current flows within networks the percolation occurs through several EPPs. Fairfield et al [19] have demonstrated how the electrical formation of paths within networks is deeply influenced by the shape of the electrodes. However, intuitively one can expect the formation of paths perpendicular to the electrodes. Even from a macroscopic point of view, in nature, the same phenomenon happens when lightning strikes, water flow within a pipe system or capacitors breakdown [20]. Considering, for example the latter case, when the built-in pressure (i.e. electrical pressure) is sufficiently high to cause the electrical breakdown of the insulating layer interposed between the electrodes became conductive. It is then possible to think that the same process occurs within NWNs and for this reason, a similar approach will be used in the experiments. The compliance current is increased in a stepwise way to unveil the mechanism beyond the activation stage. The limiting effect of the compliance helps to visualize the formation of electrical paths within the film in a more controlled way. A typical experiment that covers a wide range of I_{cc} levels required for the activation is shown in Fig. 3.11.

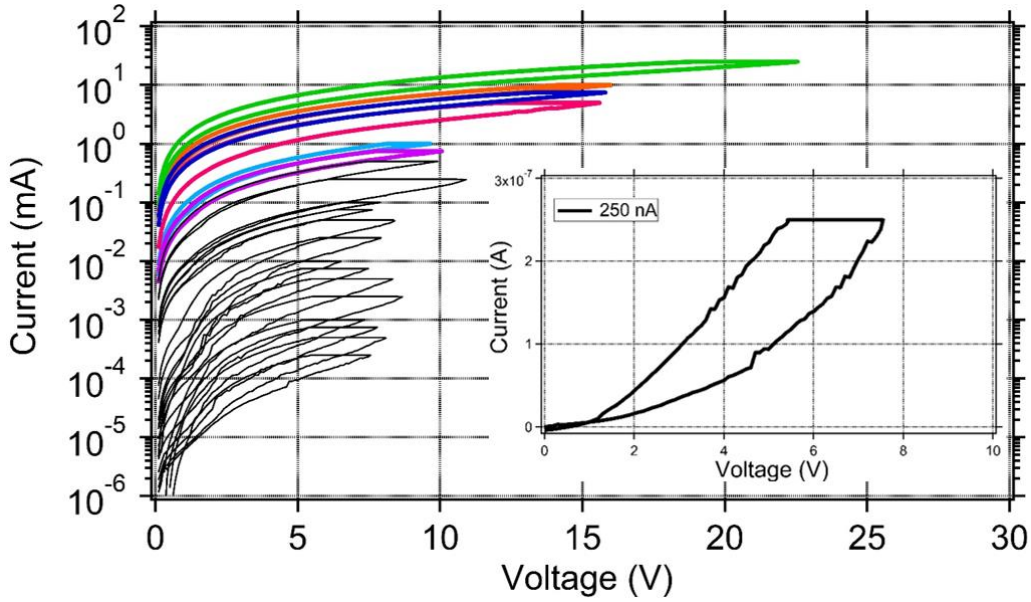

Fig. 3.9 Activation curve performed over the entire range of compliances. The initial activation of the network at $I_{cc} = 250\ nA$ is shown as inset.

The first activation of the network ($d = 1000\ \mu m$), shown as inset in Fig. 3.9, is performed using an $I_{cc} = 250\ nA$. As can be noted from the current level, initially the system is in the OFF state. The application of an increasing voltage causes a non-linear current response suggesting a behaviour that differs from a linear Ohmic behaviour. Further increases in the compliance lead to more stable states that behave according to Ohm's law. In fact, as can be seen in Fig. 3.9, the electrical response of networks is determined by the different current compliances used to activate the device.

Current sweeps

Following this, a different approach using current sweeps has been used to unveil the activation mechanism partially described by the results presented so far. The initial idea was to replicate the same experimental approach used with the voltage sweep but using current sweeps instead [21]. One example of a current dual sweep experiment performed on a $50 \times 50\ \mu m$ network is shown in Fig. 3.10. In hindsight, one can consider this experiment as the turning point of the entire project helping to understand how the activation takes place within networks.

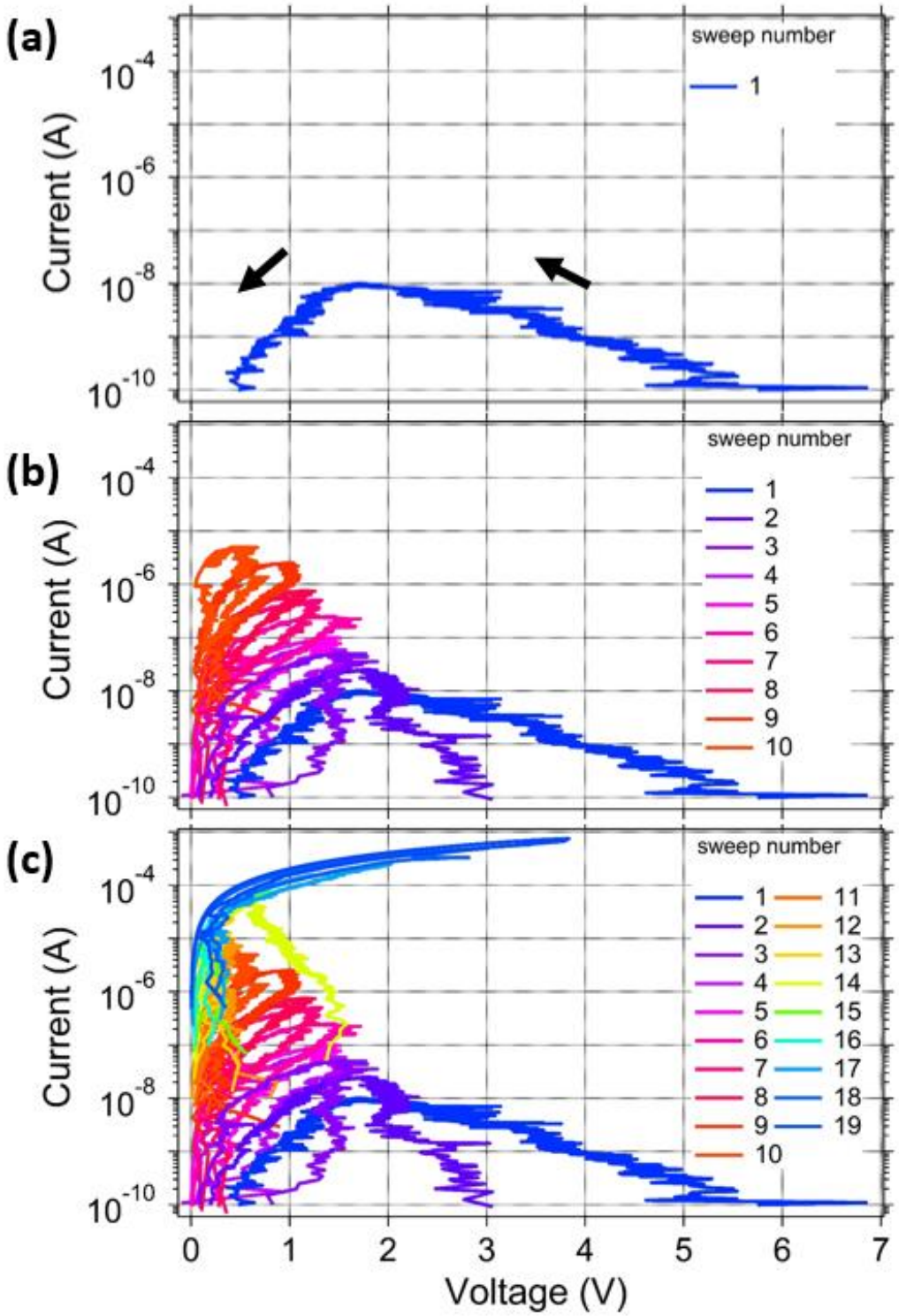

Fig. 3.10 Dual current sweep performed over an Ag NW network with $d = 50\ \mu m$. In (a) the first curve represents the initial dual sweep from $10^{-10}A$ up to $10^{-8}A$ performed on the sample. The arrows point the direction of the current sweep across all the measurements. The maximum current value is further increased for the following sweeps along the different panels (b-c).

Prior to a discussion of Fig. 3.10, it is important to highlight the fact that in order to electrically activate the sample, an initial voltage sweep with very low I_{cc}, usually $10\ pA$, is performed. Without this forming step, the current is not able to flow within the device. This extremely low current is chosen to maintain unaltered the virgin state of the network and to minimize any change in connectivity induced by current flow. Subsequently, successive current sweeps $I_{min} \rightarrow I_{max} \rightarrow I_{min}$ are applied to the sample measuring the voltage across the film. The first current sweep in Fig. 3.10 (a) covers two decades in current $10^{-10} \rightarrow 10^{-8} \rightarrow 10^{-10} A$. Intuitively, resembling the behavior found in Fig. 3.6, one might expect that the voltage follows the applied current. Surprisingly the voltage, as indicated by the arrows in Fig. 3.10 (a), is decreasing even when the current is increased during the sweep. At this stage, this voltage behavior is the first hint that at low compliances something else is happening within the junctions. A new regime, related to a different conduction mechanism that was not unveiled by earlier studies on NWNs. Further increasing I_{max} caused an even further decrease in voltage during the sweeps. However, it can be noted how, during the process for higher applied currents, the area of the loops tends to decrease. This non-ohmic behavior remains unchanged until the 12th sweep (orange trace in Fig. 3.10 (b)), where the voltage response suggests a different conduction mechanism. The voltage traces with $I_{max} > 10^{-5} A$ are characterized by an ohmic regime in which the voltage is directly proportional to the current. Furthermore, the area of the curves (i.e. 13th-14th sweeps) starts to increase again, pointing to the fact that the conductivity of the film is evolving once again. For current greater than $10^{-4} A$ there is a strong I-V linearity that most likely corresponds to the full optimization of the network.

Collectively these data presents the first evidence that the conduction process in Ag NW networks is based on two different mechanisms. The first mechanism, for low current supplied, shows that current and voltage are inversely proportional. Following on from the discussion in section 1.3, it is possible to speculate that the activation in this regime is totally modulated by a conductive filament (CF) that grows within the PVP layer between wires changing the resistance of the whole system [5]. For this reason, it is plausible to consider that tunnelling-based processes

occurring at the single junction level modulating the entire sheet resistance of the film. The second mechanism, for higher current compliance $I_{cc} > 10^{-5}A$ is instead a pure ohmic behaviour. The current and the voltage are directly proportional and the subsequent sweeps will contribute to further decrease the total resistance of the system due to the co-opting of the nearby junctions and wires to create branched and parallel paths [5].

Current steps

In order to shine additional light on the transport types we designed a different experiment in which the current is increased through current steps or staircase while recording the voltage across the network. In doing this we want to fully cover the entire current spectrum (from pA to mA) defining the different conduction mechanisms. The relative voltage trace acquired from a $200\ \mu m$ Ag NW network is shown in Fig. 3.11.

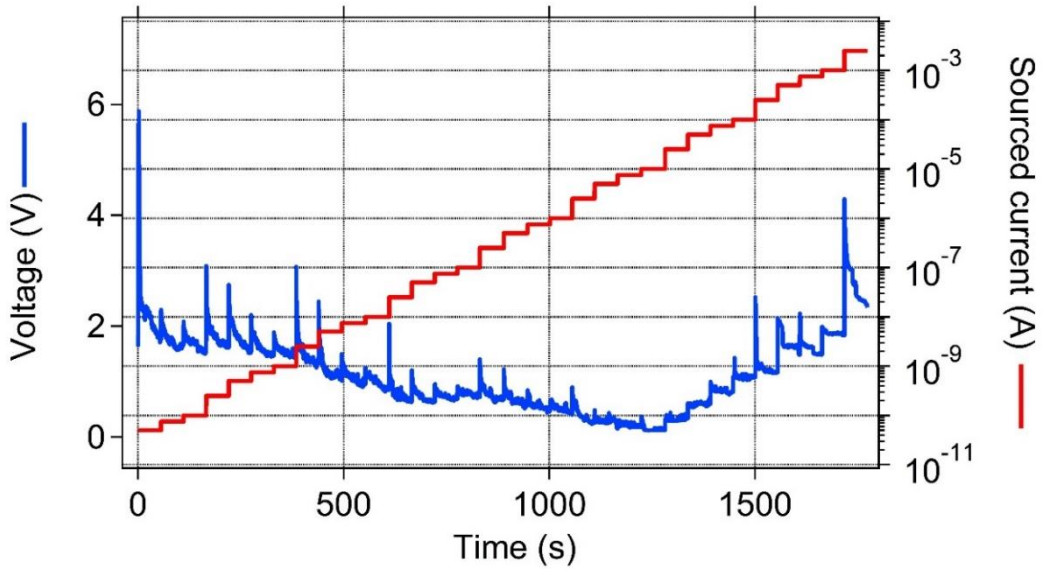

Fig. 3.11 Current step measurement performed on an Ag NW network with $d = 200\ \mu m$. A current (in red) is forced to flow in the network in a stepwise way while the voltage (in blue) is collected.

In the first region, for sourced current $I_s < 1\ \mu A$, an inverse proportionality is found between voltage (blue trace) and current. The second part, for $I_s > 10\ \mu A$,

shows a linear dependency that indicates an ohmic behaviour. This trend confirms the hypothesis introduced earlier in which the activation process involves two distinct conduction mechanisms. Moreover, Fig. 3.11 gives further insights into the current ranges of the two regimes. A net separation occurs within tenths of μA current sourced range; the voltage suddenly reaches its minimum value and the system switches between the two regimes. Although the voltage trace shows in Fig. 3.11 is obtained from a $200\ \mu m$ Ag NWnetwork we have found that networks with different sizes behave similarly to what shown in Fig 3.11. At this point we will use the curve in Fig. 3.11 as an example to describe step-by-step the evolution of the network along the activation process.

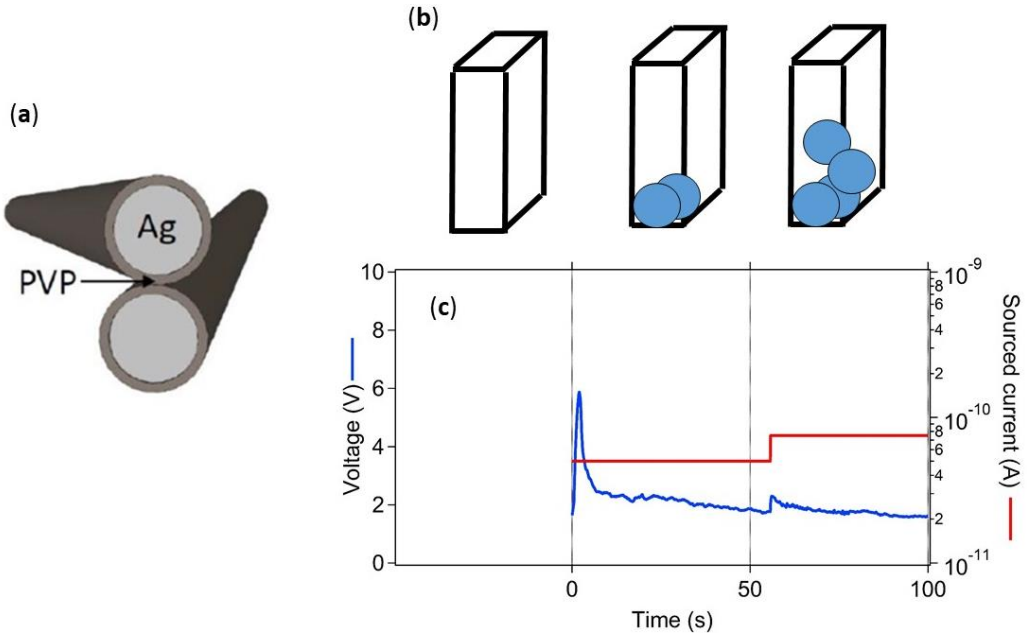

Fig. 3.12 In (a) a sketch depicts an Ag NW junction that along with the schematization in (b) help to understand the voltage signal shown in (c). Each junctions of the network can be considered as a box that as the current passes through hosts the CFs enabling the conduction at a larger scale. The current (in red) is forced in the network $d = 200\ \mu m$ while the voltage (in blue) is collected. Initially the junctions within the network are in the OFF state and the CF is not present. As the current is stepped up a certain number of Ag ions will be formed building the CF as sketched in Fig 3.12 (b).

The sketch in Fig. 3.12 (a) helps visualizing the process at the early stage during the application of the current step to the network. Initially, for $t = 0\ s$ (see Fig.

3.12 b-c), the network, as well as its junctions, is in the OFF state. Following the approach of the variable gap model introduced in section 1.3 [22], it is possible to consider the junctions across the network as boxes in which a CF can grow in response to an electrical stress. As long as current is forced into the system, a certain amount of energy is supplied to the network. This energy calculated as $V \times I \times t$ is used by the system to create CFs within the "activated" junctions. V represents the voltage acquired, I is the sourced current and t is the time expressed in seconds. Thanks to the Joule heating, the local temperature increases and therefore the kinetics of atomic diffusion increases favouring the CF formation. Knowing that the current applied remains constant within a step, the energy injected into the network will follow the same characteristic shape of the voltage. Therefore, a huge quantity of energy is initially absorbed, but after a certain amount of time t, it reaches an equilibrium state. The reason for this particular behaviour can be found in a publication done by Gao et al [23]. In their work a MIM system is used to show the formation of a CF within the insulating layer through Ag_2S clusters that switch the cell to the ON state. In the same way, in our case the energy is used to create the filaments through chemical reactions within the junctions. This requires a large amount of energy as the current is increased highlighted by a voltage spike. The system reaches then an equilibrium state in which all the CFs within the junctions are stable. This resulting state is characterized by a well-defined conductance state that remains unperturbed (it is decaying slowly) as long as the electrical stimulus is maintained. The following change that occurs for $t = 60s$ (see Fig. 3.12 (c)) with the application of the second current step, introduces additional energy into the network. Energy that is redistributed across the whole network further decreases the tunnelling gap within all the activated junctions decreasing the overall resistance of the film. Can be noted how the voltage spike associated to the second jump in current is smaller if compared to the previous one Fig 3.12 (b-c). This is simply due to the fact that in the first case the system was in its virgin state while during the second jump less energy is required to proceed with the formation of the pre-existing CFs. In other words, larger spikes usually correspond to larger changes in the resistance of the

film. This can be understood thinking in terms of the variable gap model [22] where the overall resistance is associated to two different contributions. An ohmic part due to the conduction within the CF and a tunnelling part related to the remaining gap left within the junction. Approaching in fact the condition in which the electrical path is fully optimized the voltage spikes are practically absent in the voltage trace as shown in Fig. 3.11 (around $1250\ s$) or Fig. 3.13. When the current pass from $7.5\ \mu A$ to $10\ \mu A$ all the junctions of the network present in the main electrical path become fully optimized and the relative voltage trace is practically flat.

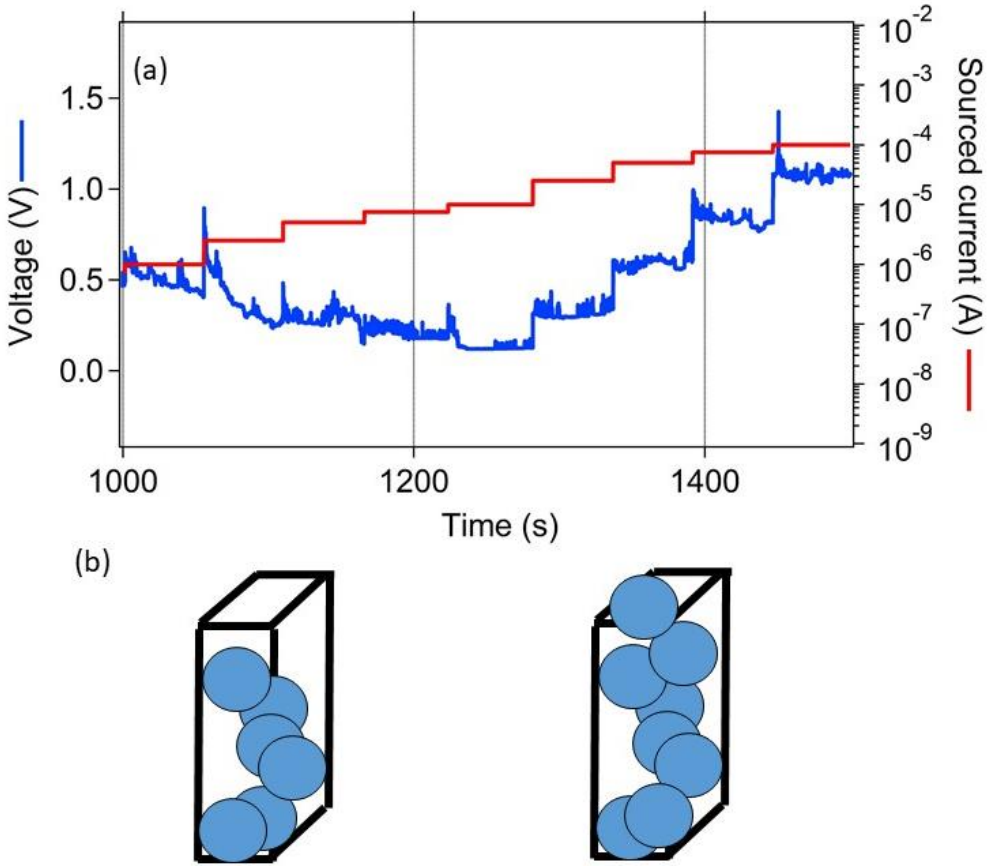

Fig. 3.13 Following the scheme used in Fig. 3.12 the increase of the applied current causes a progressive growth of the CF within the junctions embedded in the network. Specifically, in Fig. 3.13 (a) a portion of the voltage signal of Fig. 3.11 is used to show the conduction mechanism change. For $t < 1200\ s$ in (a) the voltage is decreasing while increasing the current meaning that the energy supplied to the system is used to close the tunnelling gap as shown in (b). At roughly $t = 1250\ s$, the current step used completes the filament and the overall film behaves following the Ohm's law as indicated by the voltage trend.

Despite further strengthening of the junctions, i.e. multiple CFs within the same junction, might contribute to lowering the total resistance, it is worth considering that the resistance is decreasing for few other orders of magnitude in the current. Besides, after a few current steps associated with a practically unchanged voltage, several voltage spikes can be noted. Once again, this is an indication of the fact that the network after the optimization of the main path is again spending energy widening the main path by the joining of the closest junctions to the main path. Moreover, on closer examination, one can be see that the amplitude of the peaks is not uniform across the duration of the experiment. This resembles the activation mechanism discussed at the beginning of the chapter matching quite well with the activation process described by Nirmalraj et al [6] in which larger spikes correspond to larger areas of the film being activated.

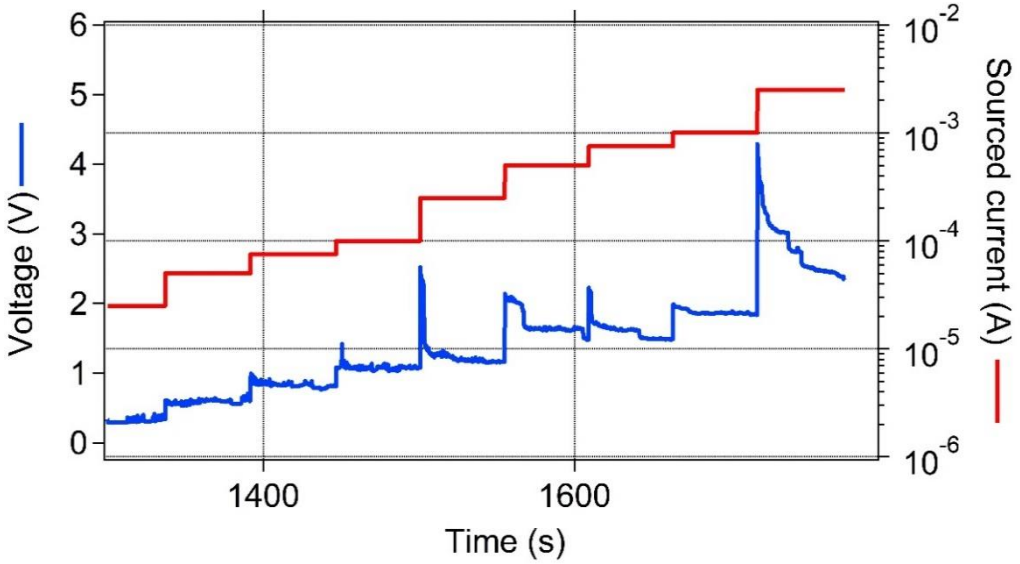

Fig. 3.14 Plot of the voltage vs time for $I > 1\ \mu A$ supplied to the system. As can be seen in this region the voltage increases following the increase of the current showing an ohmic behaviour.

In the latter part of the activation curve shown in Fig. 3.11 for current greater than $10\ \mu A$ the voltage evolves following the Ohm's law. Here, it is reasonable to think that the voltage spikes are due to the activation of parts of the sample that were not activated until that point, which suddenly became conductive. This

corroborates the evidence reported by Nirmalraj et al [6] and our hypothesis according to which the network firstly activates through an electrical main path. After the optimization of the initial path the nearest NWs join the main path further reducing the resistance of the entire film.

To proceed with the activation study, Fig. 3.15 makes a comparison between networks with different dimensions.

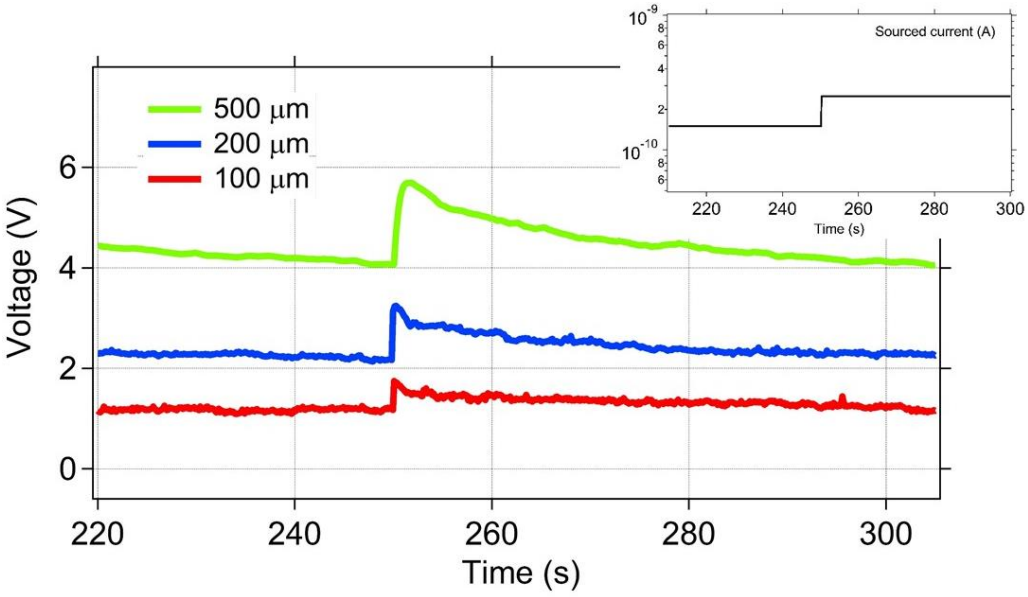

Fig. 3.15 As highlighted in the text, the voltage trend due to a current step is highly influenced by the dimensions of the samples and consequently the number of junctions between the electrodes. The three different traces here shows the response of the system to the same current step. Larger devices have in general a wider voltage response that most likely is due the higher energy required to proceed with the activation creating longer filaments all over the network. The inset shows the current step $(100 \rightarrow 250\, pA)$ applied to networks with $d = 500, 200$ and $100\ \mu m$ respectively in green blue and red traces.

Fig. 3.15 shows the voltage signals acquired for three different network sizes; the blue trace is the voltage behavior of the $200\ \mu m$ network already shown in Fig. 3.11. The voltage behavior of a network with $d = 500\ \mu m$ is shown in green while the curve associated to a smaller network with $d = 100\ \mu m$ is highlighted in red. The current step considered in this particular case is $100 \rightarrow 250\, pA$ that,

according to the current ranges discussed earlier, corresponds to the very beginning of the activation. It is important to remark in this case that a direct comparison is possible since the concentration for all the different samples is maintained constant. Can be noted how larger networks require a larger voltage, and consequently energy, for the activation process merely because of the number of junctions used to connect the electrodes. Furthermore, the shape of the peaks gives some information about the dynamics of the activation. The peak associated to the $100\ \mu m$ sample appears much narrower in respect to the $500\ \mu m$ one, indicating that the redistribution of the voltage across the network requires a certain time after one current step. It also indicates that networks, especially the larger one, have the capabilities to absorb in a more efficient way the current blast due to an electrical stress.

Current steps on single junction devices

In order to verify the voltage behaviour at single junction level the same kind of current step experiments are performed on the highlighted (red square) single junction device shown in Fig. 3.16.

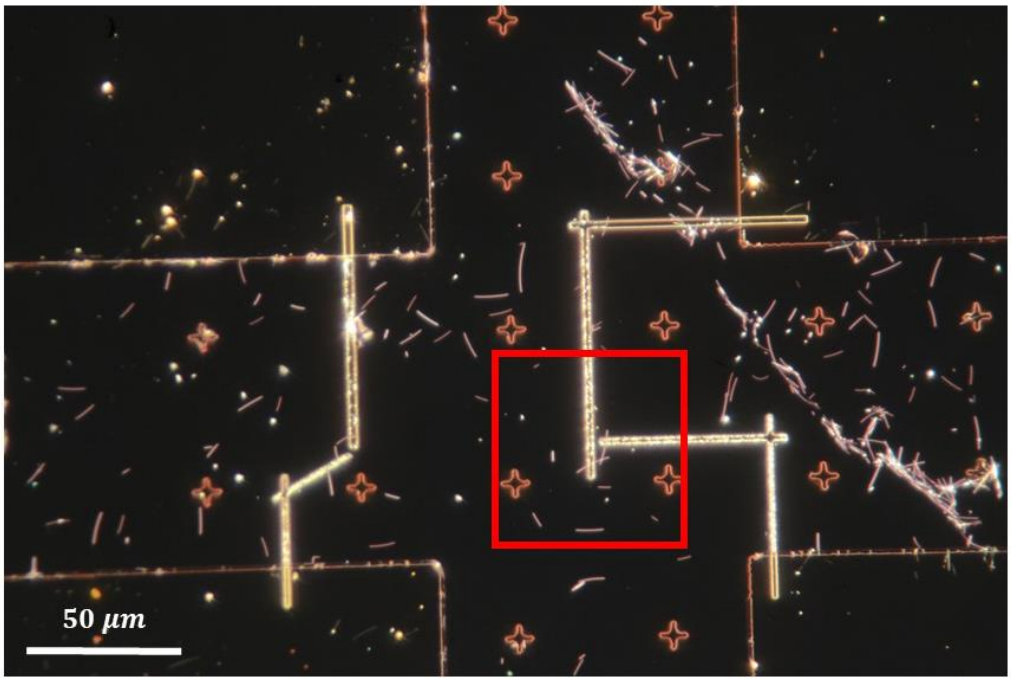

Fig. 3.16 Optical picture of the single junction device realized with Ag NWs used to study the voltage response of a confined system to the current step experiment performed for several networks. The procedure to fabricate the sample can be found in section 2.4.

The electrical response of the sample is comparable with the characteristic obtained for networks. The first thing to note when comparing network (see Fig. 3.11) and junction results is the voltage behaviour. For networks, independent of their dimensions, the voltage drops initially until it gets to the turning point where the conduction mechanism switches.

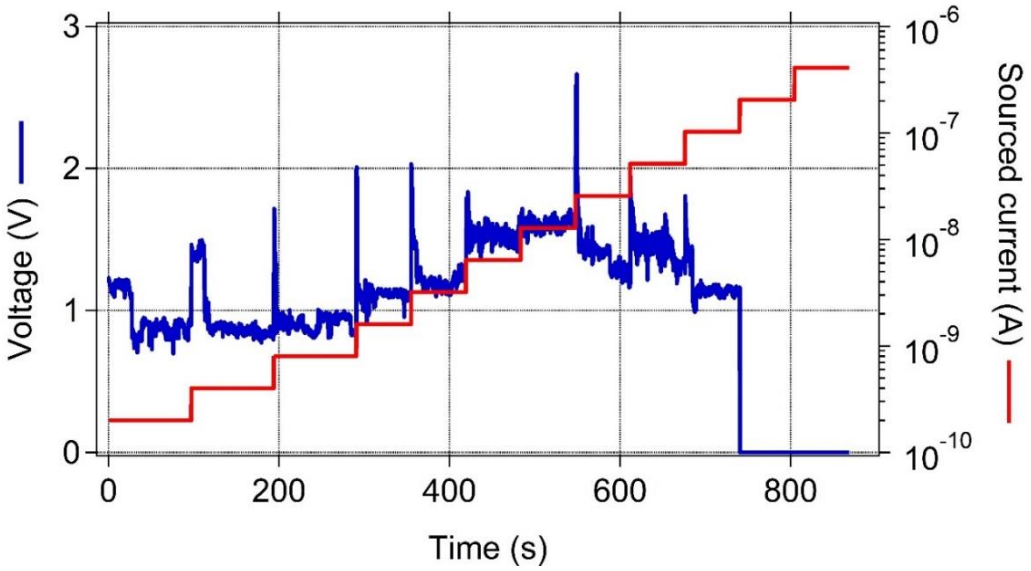

Fig. 3.17 Current step measurements on crossed Ag nanowires. During the experiment, the current applied was doubled in each step. The conductance value was extrapolated with a linear fit on the flat part of the voltage trace after the equilibrium condition for that particular step is achieved. In the last few steps, when the current jumps between $100\ nA$ and $250\ nA$ an abrupt jump of the voltage suggest the switching to the ON state. Furthermore, with such a current the CF has been built within the PVP active layer and the two inner Ag nanowires are electrically connected. This almost instantaneous jump proves that the formation of CFs within single junction devices actually behaves as a switch.

But, as can be seen in Fig. 3.17, the voltage at first increases disagreeing with the behaviour found for networks. Further increases of the current sourced to the system will cause a reduction in the measured voltage (after $550\ s$) until the switching point where the mechanism changes. This process is much striking in the case of single junctions as can be seen from the plot shown in Fig. 3.18 where the voltage axis is converted into the logarithmic scale.

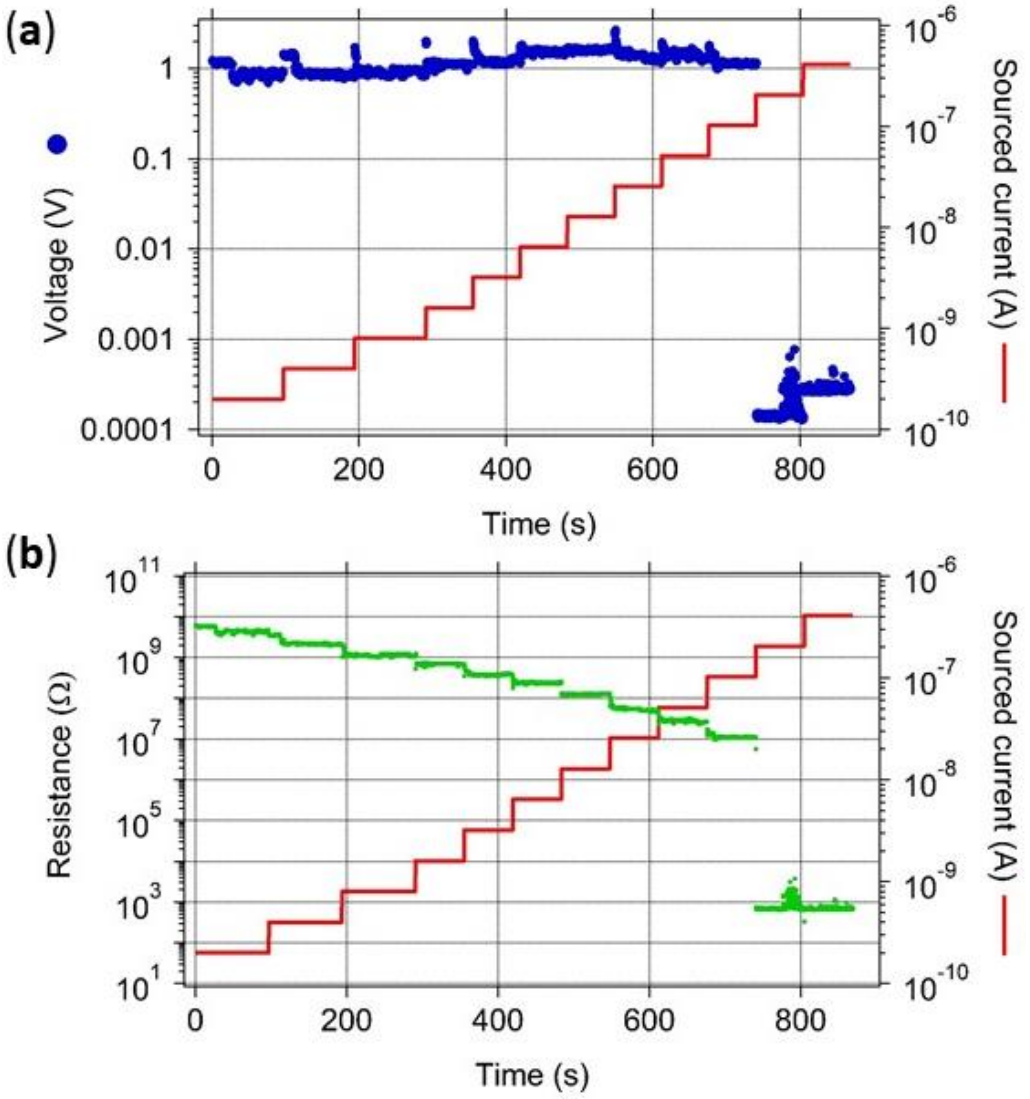

Fig. 3.18 In (a) the voltage curve already presented in Fig. 3.17 is plotted in logarithmic scale to focus the attention on the last part of the trace. In fact, as can be either seen from the plot of the resistance in (b) there is a huge jump in resistance due to the fact that the junction has been completely activated. Furthermore, can be either noted that the device once reached the LRS does not change its resistance increasing the current applied. This means that the CF bridges the two internal Ag cores and a further increase of current will induces the electrical breakdown of the device.

An abrupt jump, of almost four orders of magnitudes, can be seen in the voltage response. Moreover, the same trend is confirmed by the resistance behaviour in Fig. 3.18 (b). Although a direct comparison with the applied current is not possible due to the different current range, it is possible to note that for this particular device, the system experiencing a current jump between $100\ nA$ and $250\ nA$

(around 700 s). Such current stimulus is sufficient to create a filament within the PVP layer and close the junction gap. Once the CF is formed within the device, it behaves as a resistor as proven by the following current steps applied. A further increase of current causes, in the majority of the cases, the electrical failure of the devices due to electromigration [24]. Electromigration makes it difficult to strengthen the CF formed so that the conductance tunability that is available from networks is lost. Note that, comparing with Fig. 3.11, as expected the behaviour related to the joining of other junctions and strengthening effect are not present in the case of single junctions.

3.4 Further characterization

Having elucidated the mechanism beyond the activation at junction level, a wide range of tests are performed to understand the real capabilities associated with NWNs. Firstly, a study about the ability to store information within the junctions is introduced. Following, in order to understand the nature of the CF created within the junctions, we did perform several experiments varying the temperature of the networks.

3.4.1 Decay time

As shown, by carefully controlling the activation process, it is possible in some sense to engrave defined conductance states within NWNs. However, we know that these states, especially for low injected current, are extremely unstable. Therefore, here we want to describe the deactivation process in network and single junction devices [25]. A typical experiment performed on a single junction device is shown in Fig. 3.19. Through the usage of different current compliances, voltage dual sweeps are used to drive the device in a particular conductance state. Subsequently, a voltage pulse train low enough to not perturb the conductance state, shown as an inset in Fig. 3.19, is used to monitor the conductance state over the time.

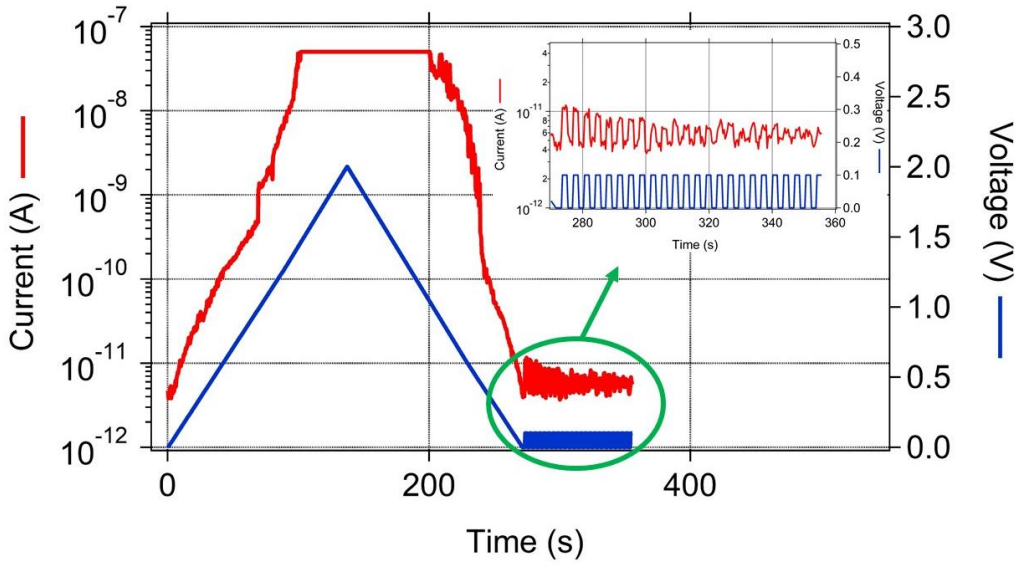

Fig. 3.19 Activation curve with $I_{cc} = 50\ nA$ of a single Ag junction device followed by a voltage train used to test the conductance over the time. The inset shows the voltage pulses in blue and the relative current signal collected in red.

Knowing then the voltage applied as pulses and the relative current level, a conductance can be associated to each pulse. In plotting the conductance values as the time evolves, we are able to extrapolate the decay time (half-life time) at each different compliances level as shown in Fig. 3.20.

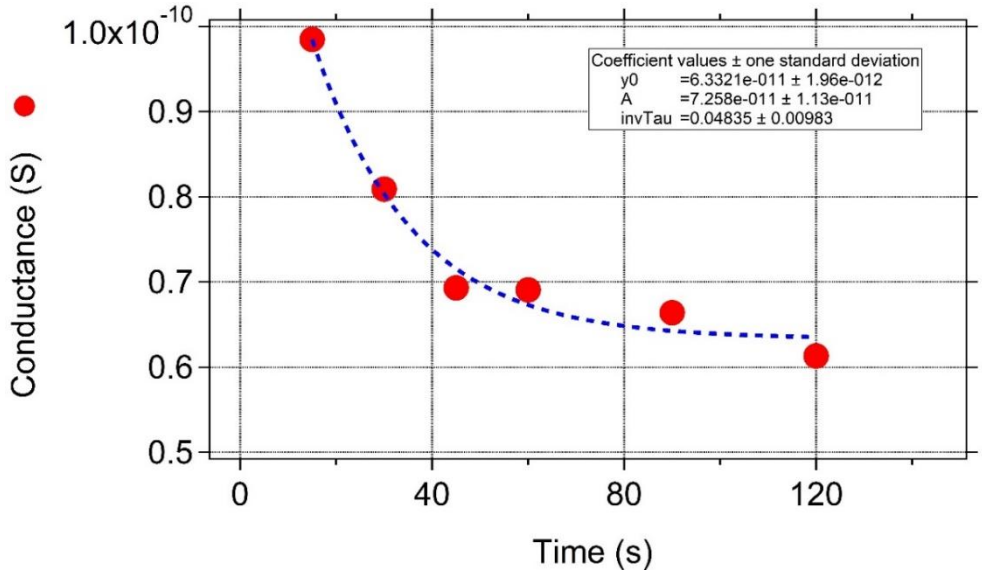

Fig. 3.20 Conductance decay of a single junction device obtained from the experiment shown in Fig. 3.19. Through an exponential fit the decay time can be extrapolated as the I_{cc} changes.

Repeating the same measurements for different I_{cc} enables us to analyse the decay time of the CF formed within a junction as the compliance changes. As expected, the stability of the conductive filament built within the PVP layer depends strongly on the compliance used during the activation. For current levels lower than $100\,nA$ the decay time remains practically unchanged. However, increasing the current helps to create a more stable filament that has a longer decay time. This can be easily explained considering that in the first case the CF is very tenuous but at increased current it becomes much more stable over the time. Furthermore, it is important to remark that during the experiment, a maximum compliance of $1\,\mu A$ is used to prevent the electrical failure of the device. The blue dashed line helps to visualize the decay time trend as the compliance increases. One can extrapolate that for compliances greater than μA the decay time increases exponentially. In this condition, it is very likely that an electrical welding phenomenon occurs and the junction will result permanently activated [26,27].

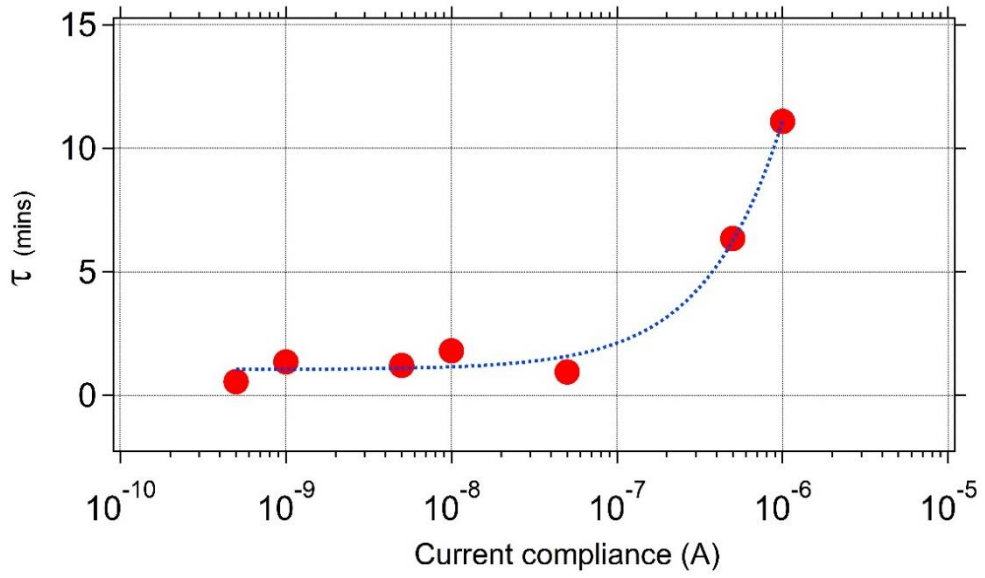

Fig. 3.21 Decay time versus I_{cc} plot obtained from a single Ag junction device. The blue dashed line is eye-driven line that helps to understand how the CF present in the junction became more stable as the current is increased.

The same experiment performed on single junction is subsequently repeated on networks to test the stability on a larger scale. In this case the current supplied to

the sample creates several CFs across the main electrical path within the film therefore we are monitoring the global electrical response of the film. Fig. 3.22 shows the conductance decay measured from a $200\ \mu m$ network for compliances pA to μA ranges.

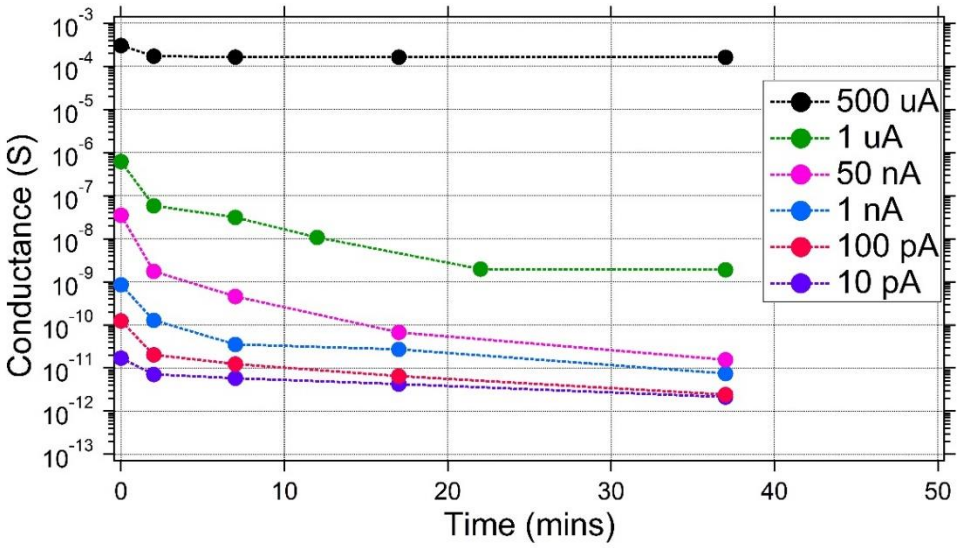

Fig. 3.22 Conductance decay experiments performed on an Ag NW network for different I_{cc}. Increasing the compliance will result in longer decay times that are extrapolated with an exponential fit on each conductance curve. The dashed lines between the experimental points calculated through voltage pulses are eye-guide lines.

Considering the wider dimensions of the system it is worth noting that the time interval over which the conductance was measured is longer than in the single junction case. However, the trend is similar, for low compliances the conductance state degrades very quickly but the increasing compliance causes a strengthening effect reflected by longer decay times.

A direct comparison between the decay time for a $200\ \mu m$ network (in red) and junctions (in black) is shown in Fig. 3.23.

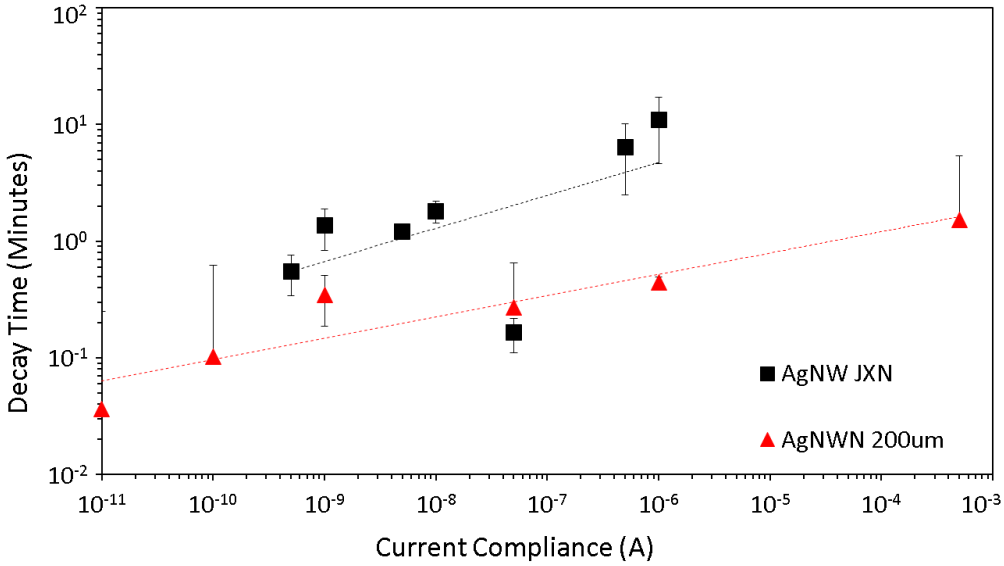

Fig. 3.23 Compassion between the decay times associated to an Ag junction device in black and a $200 \times 200\ \mu m$ Ag NW network in red. Can be noted how for the same values of compliance current the decay time associated to networks is shorter than a single junction device.

The logarithmic plot of the decay against the current compliance highlights the fact that for the same compliance value, the decay time is larger in the case of junctions. This can be associated with the fact that both junctions and networks are experiencing the same amount of current. For junctions, hundreds of nA are sufficient to create a stable filament in the active material. However, in the case of networks, higher currents are usually required to obtain the same grade of stability in terms of CFs. In other words, the current is redistributed within the network granting a much more gradual growth of the filament within the PVP layers.

3.4.2 Temperature dependence

The second investigation on the properties of the filaments formed is inspired by the work published by Oliver et al [28]. In this publication, the nature of the conductive filament electroformed in NiO_x junctions is investigated through variable temperature current-voltage measurement. According to the forming

process experienced by the devices, temperature can lead the system to manifest a metallic or semiconducting behavior. As described in section 1.3, NiO_x nanowire can be considered as unipolar switching memories and conventionally the formation of the CF is associated with the movement of oxygen vacancies within the active layer [29,30]. Oliver et al [28] highlight the possibility to obtain an intermediate semiconducting state between the insulating HRS and metallic LRS. This condition is achievable by activating the device with increasing the compliance in a stepwise way. In some sense, this process is similar to the procedure described earlier for the Ag NW networks. Furthermore, activating the junction with a higher compliance, for instance $10\ \mu A$, creates a filament with metallic behavior. Therefore, in order to understand the nature of the CF formed within the Ag@PVP networks the same approach is performed on a $10\ \times 10\ \mu m$ network at different temperatures. An optical image of the network used for the investigation prior (a) and after (b) the temperature change is shown in Fig. 3.24.

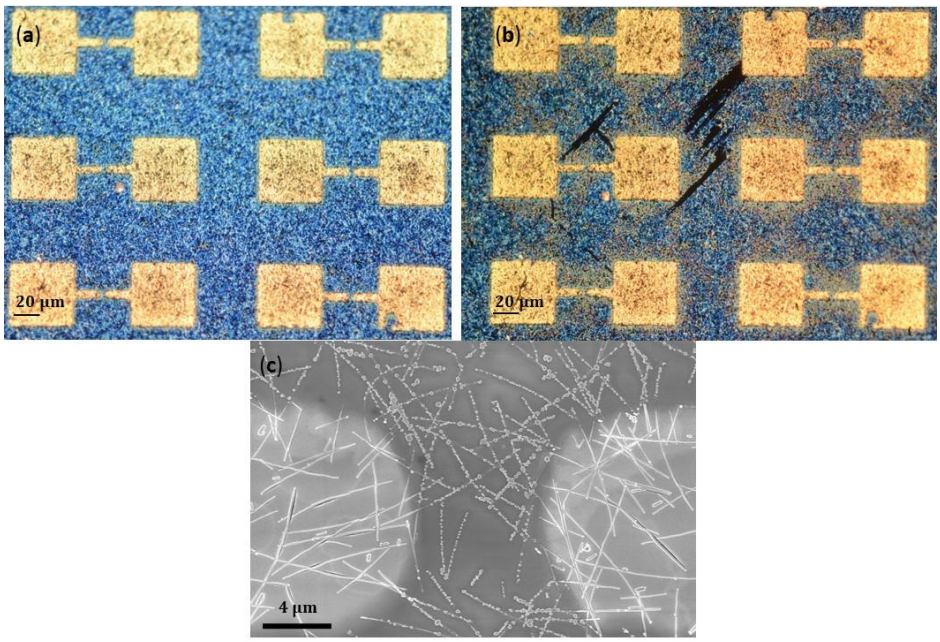

Fig. 3.24 Ag NWN with $d = 10\ \mu m$ used to study the electrical behaviour of the CF varying the temperature of the device. In Fig. 3.24 (a) the sample before the measurements while in (b) the same device after the temperature variation with a minimum temperature of $100\ K$. From a quick comparison of the images (a) and (b) can be noted how the device degrades due to the thermal change (same imaging conditions). On the other hand, the SEM image in (c) further confirms the nanowires deterioration.

The experiment performed follows the same approach introduced by Oliver et al [28]. Initially the sample under vacuum is tested at room temperature. Starting from a $10\ nA$ compliance, the subsequent five voltage sweeps have higher I_{cc}. Once the sweeps are completed, the system is brought to a lower temperatures and the electrical tests are performed in the same way.

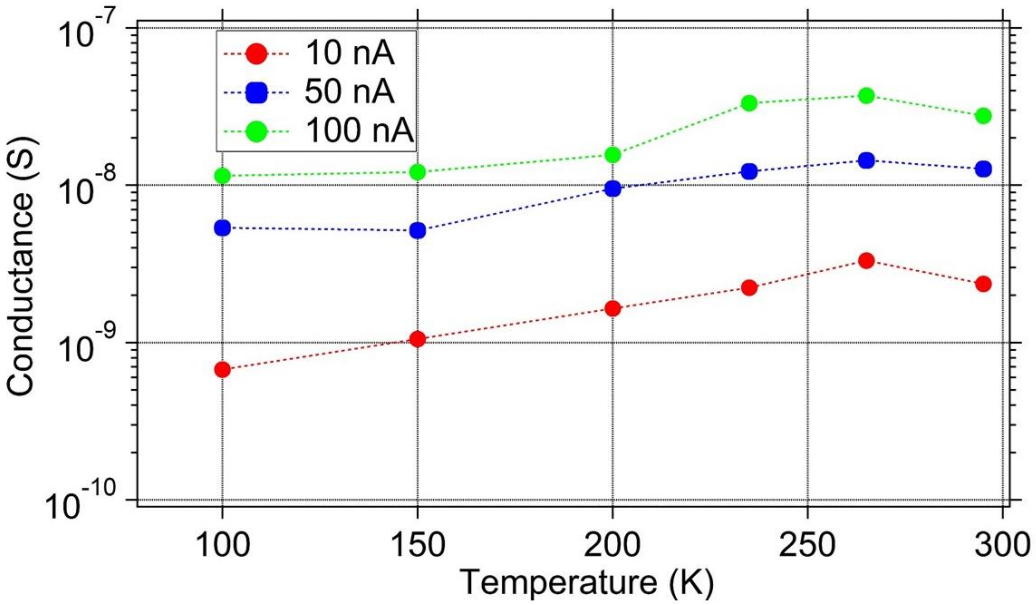

Fig. 3.25 Comparison between the conductance values obtained from the device shown in Fig. 3.24 $(d = 10\ \mu m)$ at different temperatures. The conductance of the film decreases as the temperature decreases pointing to a semiconducting behaviour as previously shown by Oliver et al for Ni device [28].

Fig. 3.25 shows the conductance values extrapolated from the I-V sweeps for different temperatures. From the trend in Fig. 3.25, it can be noted how the conductance decreases as the temperature of the device decreases pointing to a semiconductor-like behaviour. A hypothesis that agrees with what Oliver et al reported [28] in which a slow activation of the device leads to a semiconducting behaviour in case of Ni junctions. However, considering the activation voltage at different temperatures, it is possible to make another important consideration. In fact, in Fig. 3.26, the voltage required to activate the network defined as V_{on} is plot against the temperature and highlights the fact that the activation is a thermal-driven process [31,32].

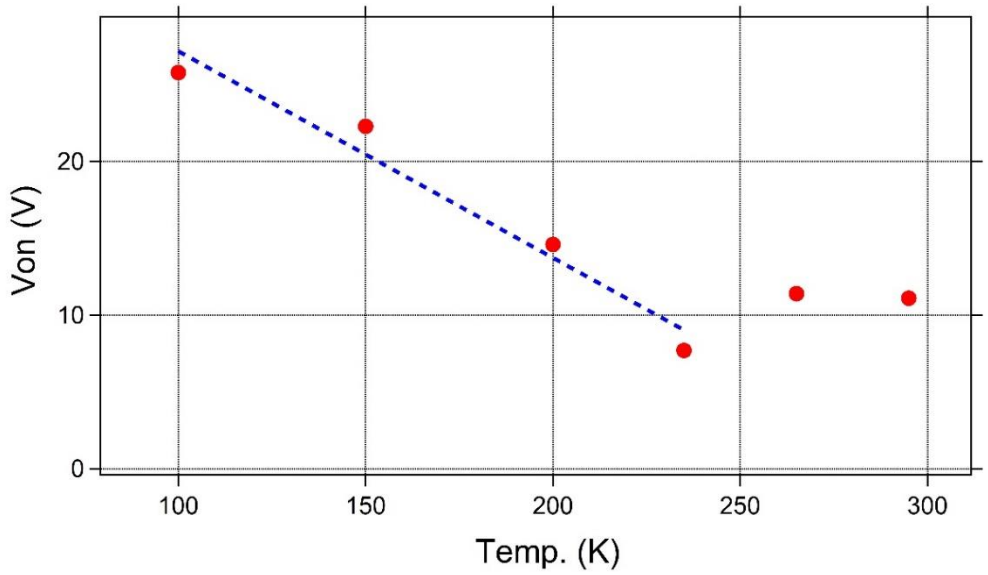

Fig. 3.26 Plot showing the voltage required to switch the network presented in Fig. 3.24 to the ON state as the temperature changes that proves how the activation is a temperature-driven process.

This reflects the fact remarked by several reports in the literature that describe the welding of the junction for different materials as energy is provided to the system [31,33]. Therefore, it is straightforward to consider that a decrease in the temperature deeply influences the activation of the junctions. In fact, referring to Fig. 3.26, the V_{on} remains unchanged until roughly $235\ K$; after that, the thermal energy along with the voltage applied is not sufficient anymore to turn on the network increasing the voltage threshold required for the activation.

3.5 Conclusion

This chapter defines the activation process within NWs and NWNS. Through different experimental approaches we were able to investigate and identify the mechanisms that enable the activation of devices. Utilizing standard voltage sweeps along with the use of current compliances it is possible to modulate the conductivity of the film. Moreover, sourcing current helped to reveal a different conduction mechanism based on tunnelling effect for low compliances. By the increase of the compliances it is possible to reduce the tunnelling gap within the

junctions moving from a tunnelling transport to a new regime ruled by Ohm's law. Further analysis have pointed out that the different conductance state created within NWNs have different decay times associated reflecting a strengthening of the CF as long the current is ramped up. Besides, the measurement performed changing the temperature have demonstrated that the CFs within the junctions have a semiconducting behaviour. Following this, all the work done to shine some light on the activation process will be used in the next chapter to actually visualize the formation of what we define "Winner Takes All" paths (WTA) within devices. A self-similar scaling behaviour that regulates the growth of CFs in junctions and similarly in networks will be either introduced.

References

1. De, S. *et al.* Transparent, Flexible, and Highly Conductive Thin Films Based on Polymer−Nanotube Composites, (2009).
2. Lee, H. S. *et al.* Synthesis of dimension-controlled silver nanowires for highly conductive and transparent nanowire films, (2015).
3. Chen, Z., Ye, S., Stewart, I. E. & Wiley, B. J. Copper Nanowire Networks with Transparent Oxide Shells That Prevent Oxidation without Reducing Transmittance, (2014).
4. Jung-Yong Lee, Stephen T. Connor, Yi Cui and Peter Peumans. Solution-Processed Metal Nanowire Mesh Transparent Electrodes, (2008).
5. Manning, H. G. *et al.* Emergence of winner-takes-all connectivity paths in random nanowire networks, (2018).
6. Nirmalraj, P. N. *et al.* Manipulating connectivity and electrical conductivity in metallic nanowire networks, (2012).
7. Sannicolo, T. *et al.* Direct Imaging of the Onset of Electrical Conduction in Silver Nanowire Networks by Infrared Thermography: Evidence of Geometrical Quantized Percolation, (2016).
8. Z. Gemmill, L. Durbha, S. Jaconson, G. Gao, K. weaver. SEM and FIB Passive Voltage Contrast. *Microelectron,* (2017).
9. Landauer, R. Spatial variation of currents and fields due to localized scatterers in metallic conduction, (1996).
10. Kirkpatrick, S. Percolation and Conduction, (1973).
11. Callaghan, C. O., Rocha, C. G. & Niosi, F. Capacitive and memristive behaviours in metallic nanowire networks, (2018).
12. Hecht, D. S., Hu, L. & Irvin, G. Emerging transparent electrodes based on thin films of carbon nanotubes, graphene, and metallic nanostructures, (2011).
13. Gomes Da Rocha, C. *et al.* Ultimate conductivity performance in metallic nanowire networks, (2015).
14. Huang, Q., Lilley, C. M., Bode, M. & Divan, R. S. Electrical Properties of Cu Nanowires, (2008).
15. Ou, M. N. *et al.* Electrical and thermal transport in single nickel nanowire, (2008).
16. Bellew, A. T., Manning, H. G., Gomes Da Rocha, C., Ferreira, M. S. & Boland, J. J. Resistance of Single Ag Nanowire Junctions and Their Role in the Conductivity of Nanowire Networks, (2015).
17. Bellew, A. T., Bell, A. P., McCarthy, E. K., Fairfield, J. A. & Boland, J. J. Programmability of nanowire networks, (2014).
18. Avizienis, A. V *et al.* Neuromorphic Atomic Switch Networks, (2012).
19. Fairfield, J. A. *et al.* Effective Electrode Length Enhances Electrical Activation of Nanowire

Networks: Experiment and Simulation, (2014).

20. Lane, N. The unseen world: reflections on Leeuwenhoek, (2015).
21. Guoming, W. *et al.* Operation methods of resistive random access memory, (2014).
22. Sawa, A. & Meyer, R. Resistive Switching from fundamentals of nonoionic redox processes to Memristive Device Application, (2016).
23. Gao, S., Song, C., Chen, C., Zeng, F. & Pan, F. Formation process of conducting filament in planar organic resistive memory, (2013).
24. Khaligh, H. H. & Goldthorpe, I. A. Failure of silver nanowire transparent electrodes under current flow, (2013).
25. Manning, H. G., Biswas, S., Holmes, J. D. & Boland, J. J. Nonpolar Resistive Switching in Ag@TiO 2 Core−Shell Nanowires, (2017).
26. Langley, D. *et al.* Flexible transparent conductive materials based on silver nanowire networks: A review, (2013).
27. Large, M. J. *et al.* Finite-size scaling in silver nanowire films: design considerations for practical devices, (2016).
28. Oliver, S. M. *et al.* Quantum point contacts and resistive switching in Ni/NiO nanowire junctions, (2016).
29. Ting, Y. H. *et al.* Observation of Resistive Switching Behavior in Crossbar Core–Shell Ni/NiO Nanowires Memristor, (2018).
30. He, L. *et al.* Memory and Threshold Resistance Switching in Ni/NiO Core À Shell Nanowires, (2011).
31. Lagrange, M. *et al.* Optimization of silver nanowire-based transparent electrodes: effects of density, size and thermal annealing, (2015).
32. Langley, D. P. *et al.* Silver nanowire networks: Physical properties and potential integration in solar cells, (2014).
33. Garnett, E. C. *et al.* Self-limited plasmonic welding of silver nanowire junctions, (2012).

Chapter 4

Self-similar scaling behaviour

This fourth chapter can be considered as the cornerstone of this thesis. All the information introduced in the previous chapters are used to help unveil the potential of NWNs. For the sake of simplicity, our study focused on the activation process in single junction devices. This leads us to a model, along with the variable gap model [1], that is capable of describing the formation of a CF within a single junction. From the activation of a single junction, we were able to devise a phenomenological model that simulates the transport behaviour of networks comprised of these junctions [2]. This enabled us to identify a self-similar scaling behaviour between junctions and networks. In doing this, all the knowledge obtained from single junctions can be transferred directly to networks and through the scaling law enables the description of the activation of these more complex systems. Moreover, simulations performed by our collaborators led by Dr. Mauro Ferreira (TCD) helped to confirm the presence of conductance plateaus in the $\Gamma \times I_{cc}$ curves that are associated to the formation of electrical paths that we define as "Winner-Takes-All" (WTA) paths. We discovered that the wires must have particular activation properties to enable the formation of preferential paths within networks and that these paths represent the most efficient way to flow current through the film.

In the second part of the chapter, to test for the presence of WTA paths we use the Passive Voltage Contrast (PVC) technique (see section 2.1.2.2) in order to confute the predictions from the simulations. Using PVC, enabled us to distinguish between three different stages of the activation process defined as the transient growth (TG), power law (PL) and the post-power law (PPL) regimes. At the early

stage, in the TG regime, the entire NWN is probed by small leakage currents to identify the most favourable paths. Once the compliance current overcome a particular threshold value, the formation of the WTA path starts in the PL regime until it reaches the full optimization at the first plateau. The system then enters in the PPL region where subsequent electrical paths start to emerge lowering the overall sheet resistance of the film.

The final part of the chapter describes the formation of WTA in terms of energy consumption. Once again, thanks to constant interplay between simulation and experimental results we were able to estimate computational entropy involved that enable us to discuss energy dissipation within networks during the activation process.

4.1 Self-similar scaling behaviour

As stated in the introduction of this chapter, to describe the activation we initially used several experimental data as starting point. In Fig. 4.1 two examples of curves showing the conductance with respect to the current compliance of a single Ag junction device in red and a $500 \times 500\,\mu m$ Ag NW network in blue. The comparison between the two curves highlights the fact that despite the vast difference in the dimensions of the two samples, the conductance for compliances $I_{cc} < 10^{-7}A$ evolves in a similar way. This striking observation of a self-similar scaling behaviour provide an important hint to how to develop a model able to describe the entire macro-scale activation process in NWNs. A second important piece of information comes from the behaviour at current compliance greater than $10^{-7}A$. As the conductance of the junction approaches the quantum conductance point (QCP), it experiences an abrupt jump well below the QCP, which is not seen for the network case. This is related to the capacity of the compliance to limit the formation of the CFs in networks, which is entirely absent in the junction case. The presence of several electrical paths afford the network a greater capacitance that facilitates smooth current flow as the compliance is increased. On the other hand, the formation of a CF within a highly confined single

junction device is a much more fragile process. The CF that bridges between the internal Ag cores with a single junction is relatively unstable and easily perturbed by increased current flow that creates multiple channels within the junction, hence the discontinuous behaviour in Fig. 4.1.

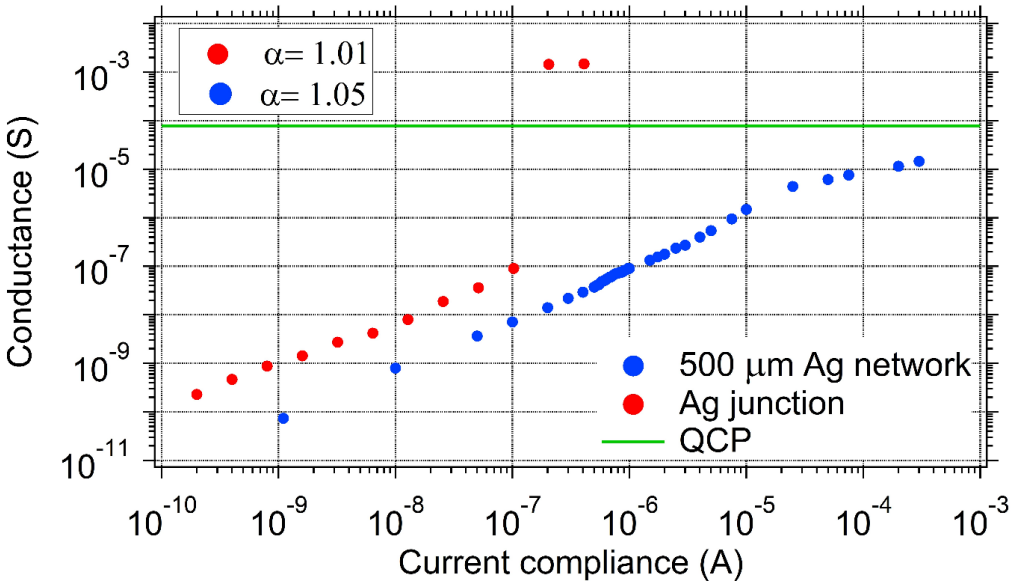

Fig. 4.1 Conductance versus current compliance for a single junction device in red and in blue for a 500×500 µm Ag NW network made both using PVP coated Ag NWs. From a fit in the linear part the two exponent are equal to 1.01 in the case of junctions and 1.05 for the network. The quantum conductance point (QCP) level $\Gamma_0 = 7.75 \times 10^{-5} S$ is highlighted in green.

The relationship between the conductance of a junction Γ_j and the compliance current I_{cc} used to grow a CF within that junction can be expressed as follow:

$$\Gamma_j = A_j {I_{cc}}^{\alpha_j} \quad \text{Eq. (4.1)}$$

In this relation obtained A_j represents a proportionality term while the α_j is a positive exponent that, as we described later in the chapter, is close to the unity. Using equation (4.1), one can fit the conductance versus current compliance data of numerous junction samples to obtain A_j and α_j values. Since Fig. 4.1 strongly suggests that both systems, single junctions and networks, scale in the same way this implies that $\alpha_j \approx \alpha_{nt}$ (with j associated to junctions and nt to networks). Our collaborators demonstrated through simulation that this is always the case for a

network whose conductance is limited by junctions. In doing so, Eq. 4.1 can be rewritten for networks as $\Gamma_{nt} = A_{nt} {I_{cc}}^{\alpha_{nt}}$.

Fig. 4.2 shows an example of $\Gamma - I_{cc}$ plot for an Ag NW network $(200 \times 200\ \mu m)$ that has been fitted to extrapolate values for α_{nt} and A_{nt}. In this log-log plot, the slope corresponds to α_{nt} value while the A_{nt} is obtained from the intercept.

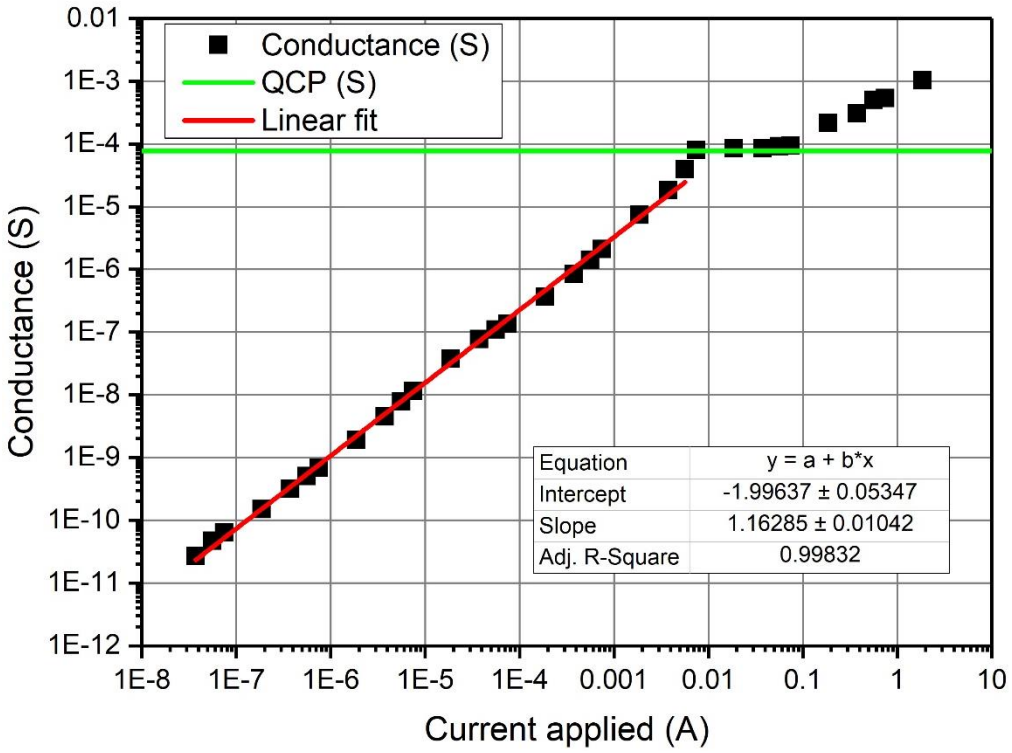

Fig. 4.2 Plot of the conductance versus the current compliance obtained for a $200 \times 200\ \mu m$ Ag NW network with a linear fit that determines the coefficients in equation (4.1) used to run the simulations in NWNs.

Performing the same type of scaling experiments on different samples enable us to gather enough experimental evidences to demonstrate the fact that the α exponent $(\alpha = \alpha_j \cong \alpha_{nt})$ oscillates around one. On the other hand, the A_j and A_{nt} values have a dependence on the type of material used to fabricate the device as we will show in the next chapter. If we now consider the analogy with the ion-drift model [3], we can associate the $A_{j/nt}$ coefficient with the mobility of the diffusing species within the active insulating layer of a junction. Moreover, the α exponent is related to the non-linearity associated with the diffusion barrier [2]. The

PL parameters measured in different nanowire systems (single wire, single junctions and networks) are reported in Table 4.1.

Table 4.1 Summary of the α and A coefficients taken experimentally from different materials samples [2]. Moreover, the self-similar behaviour is shown by the results obtained from networks (NWN) and junctions (JXN).

System type	Material	α	A
NWN $200\mu m$	Ag	1.1 ± 0.07	9.56 ± 10.24
JXN	Ag	1.05 ± 0.05	32.29 ± 15.58
NWN $20\mu m$	Cu	0.97 ± 0.03	0.49 ± 0.43
JXN	Cu	1.05 ± 0.07	3.55 ± 2.92
JXN	$AgTiO_2$	1.03 ± 0.03	7.69 ± 4.77
NWN $50\mu m$	Ni	1.01 ± 0.03	0.2 ± 0.21
Single wire	Ni	0.95 ± 0.01	0.29 ± 0.03
Single wire	TiO_2	0.83	0.003

From the table, it is possible to note how materials such Ag and Cu have α values greater than one, while materials such as Ni or TiO_2 (further discussed in chapter 5) have exponents lower than one. In the attempt to understand these differences between materials, we define a strengthening rate coefficient v_j obtained by taking the derivative with respect to the compliance in equation (4.1).

$$v = \frac{d\Gamma}{dI_{cc}} = A\ \alpha\ {I_{cc}}^{\alpha-1} \qquad \text{Eq. (4.2)}$$

From Eq. (4.2), it is clear that the exponent $\alpha - 1$ determines the strengthening of the junction and network conductance. There are three possible conditions: $\alpha = 1$ gives a constant strengthening rate. The other two possibilities describe processes that involve the speed-up $(\alpha > 1)$ or slowing-down $(\alpha < 1)$ of the formation of the CFs within the junctions with increased current compliance. It will be shown later that depending on which of the three different conditions is operative, the activation of networks happens in different ways. Exponents larger than one leads to the formation of WTA paths across the film while for $\alpha < 1$, the activation involves a larger number of paths (see chapter 5).

4.2 Formation of WTA paths simulation

Fig. 4.3 shows the simulated conductance curves obtained from a digitalized $20 \times 20\ \mu m$ Ag NW network for different α and A_{nt} values [2]. The four different colours of the curves are related to different A_{nt} values, while the α exponents are set at values around 1. From the different panels we noted how changing the α value dramatically influences the evolution of the conductance of the networks. In fact as the α values change we noted how the conductance curves are smoother when $\alpha < 1$ while showing a step like behaviour for exponents larger than one.

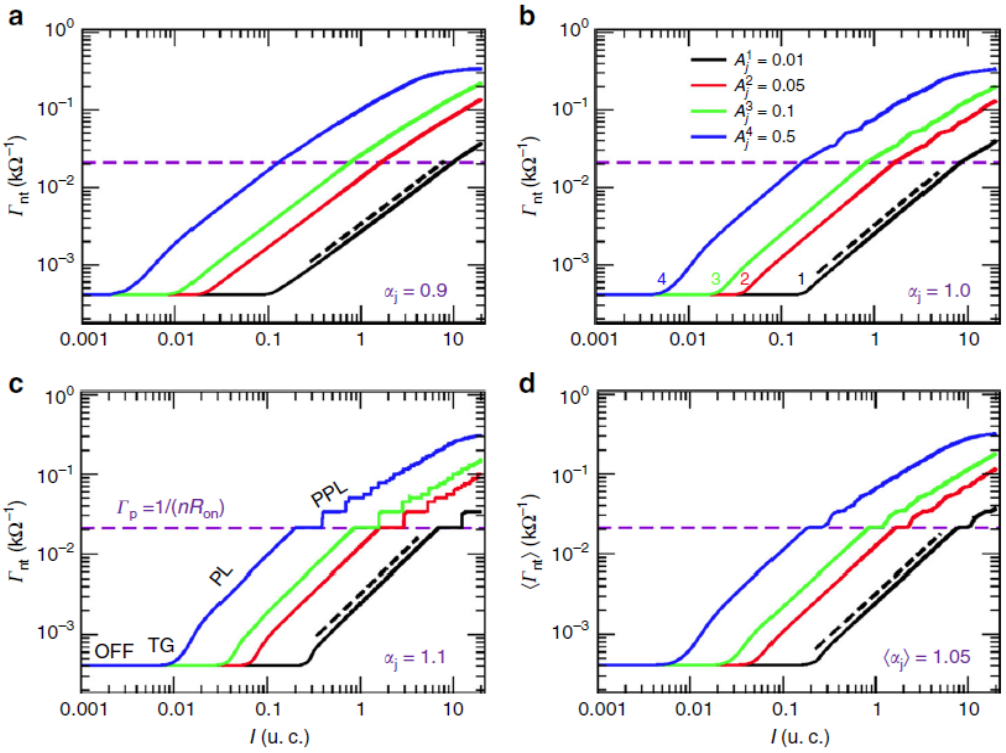

Fig. 4.3 Simulations performed to obtain the behaviour of the conductance versus current of an Ag NW network for different α_j and $A_j$values that characterize the junction units in the network. The values for the exponents are (a) $\alpha_j = 0.9$, (b) $\alpha_j = 1$ and (c) $\alpha_j = 1.1$. In (d) a disordered element is added assuming a distribution of α_j values (rather than all junctions in the network with the same α_j) is used to run the simulations and obtain the different curves for several A_j values [2]. The dashed line corresponds to the first plateau obtained during the simulations.

Although, a direct comparison with the experiment and simulation is not possible, it is possible to see changes in slope in the network data in Fig. 4.2. In contrast, however, the simulations show the presence of discrete steps along the conductance curve that we define as plateaus.

Following this, we distinguish between four different sections along the conductance curves as shown in Fig 4.3 (c). The first one, defined as OFF-threshold is characterized by a homogenous distribution of the voltage across the film. Due to the very low current, the energy supplied to the system is not sufficient to create CFs within the junctions and the overall conductance remains unchanged. The next part corresponds to a transient growth TG condition in which the current starts to become sufficient to create tenuous filaments evolving the overall conductance of the network. Reaching a critical current, the system switches into the power law PL region where there is a proportionality between the improvement of the conductivity and the current compliance used to drive the conductivity of the film. This trend continues until the formation of the first plateau that as remarked before, is the signature of the presence of the first electrical path connecting the electrodes that we define as “winner-takes-all” WTA path. After this plateau, a new regime defined as the post-power-law PPL is characterized by the presence of several plateaus. Plateaus that are related to the formation, and further optimization, of other percolating paths within the network. A clearer picture of this trend can be seen in Fig. 4.4 in which the four regions are highlighted following the activation of a simulated network.

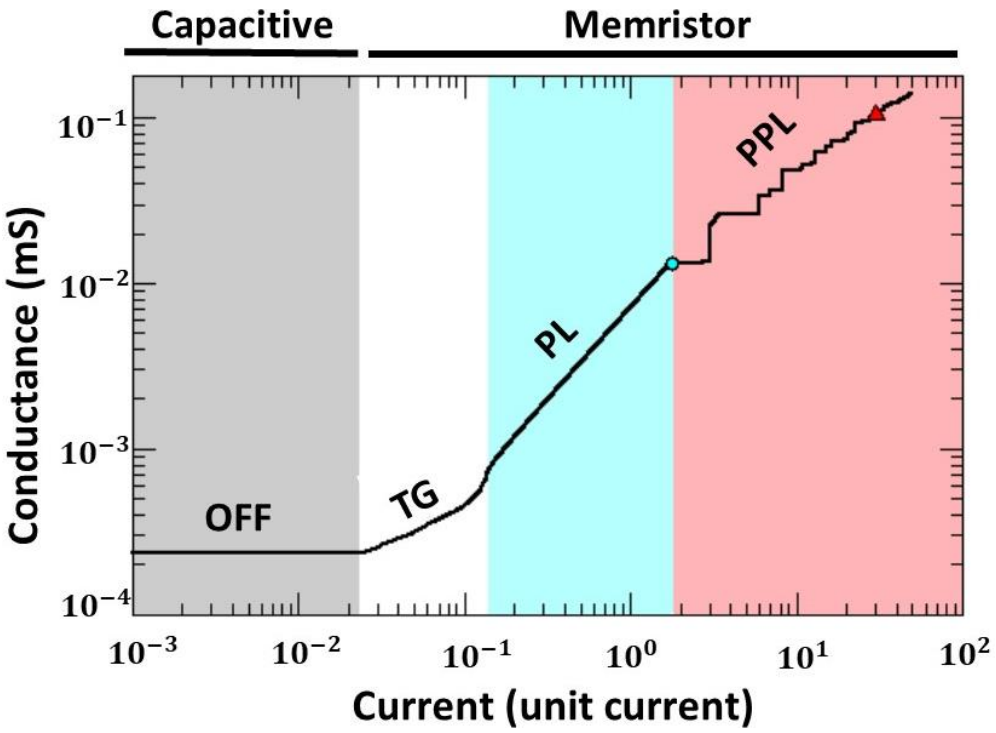

Fig. 4.4 The $\Gamma - I_{cc}$ curve can be divided into four different areas. Initially the system is in the OFF state and the low currents involved does not allow the formation of CFs within the junctions. Increasing the current regime, the network enters in a transient regime TG where the WTA is increasingly stressed. The junctions participating in the WTA starts to be conducting and the tunnelling effect dominates this process. This regime lasts until the network enters in the power law PL regime where there is a direct relation between the current compliance and the overall conductance of the film. The last region, defined as post-power law PPL, is characterized by the presence of several plateaus highlighting the formation of parallel percolating paths [4].

Although the α value obtained from the fit in Fig. 4.2 is very close with the values used for the simulation, the plateaus are clearly present only in the simulated results. As we will see in the next section this is because the sampling rate used to interrogate the network in Fig. 4.2 is too small to capture the formation of the WTA state. Moreover, thanks to our simulation we are able to visualize the different stages of the activation using current maps. Each junction within the network can be associated to an element in the conductance matrix used to run the simulation that through Kirchhoff's circuit rules enable the extraction of a

multitude of physical quantities, including current-flow maps as those shown in Fig. 4.5.

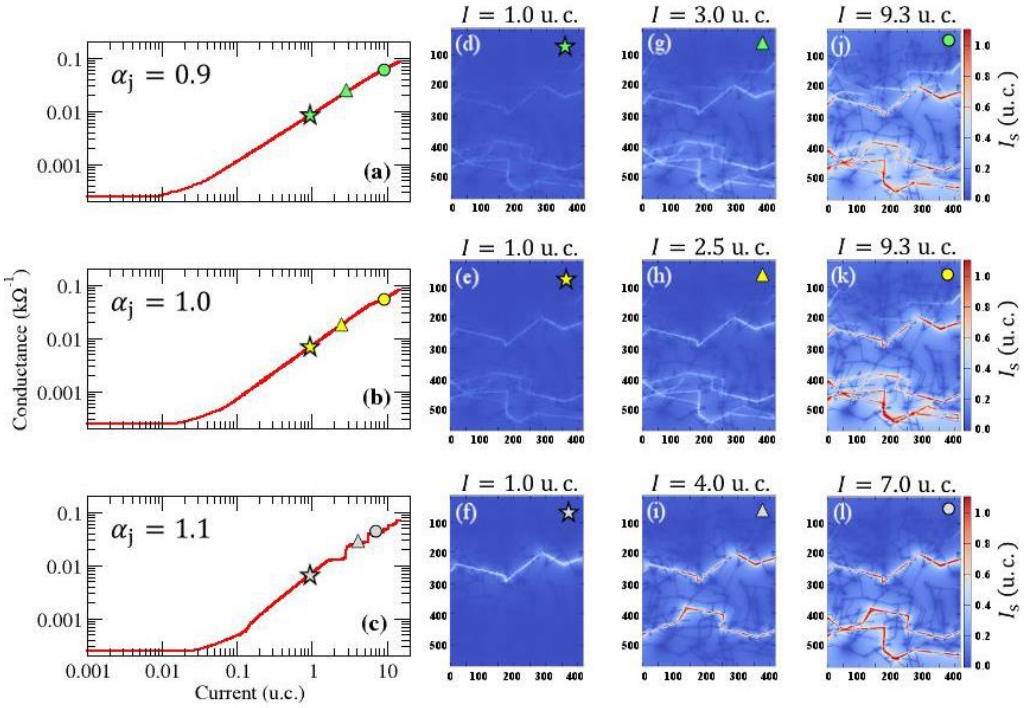

Fig. 4.5 Simulations highlighting the formation of conducting paths within a digitalized Ag NW network for different α_j values. The marks on the conductance curves present in (a),(b) and (c) correspond to the different conductive states the network endures as the current increases [2].

Focusing on the case of $\alpha > 1$ in Fig. 4.5 (c), each of the upward plateau is related to the formation of a new conducting path within the film. This confirms that the flat part of each plateaus in the simulated $\Gamma \times I_{cc}$ plots are related to the optimization of an electrical path as hypothesized in the third chapter. However, the presence of plateaus is not as evident in the case of $\alpha = 1$ and completely absent in the $\alpha < 1$ case. Consequently, we conclude that the activation process happens in two different ways. In the first case $(\alpha > 1)$, the current flows through particular paths that can be considered as the most favourable path, energetically speaking, similar to the activation as described by Sannicolo et al [5]. On the other hand, in the second case $(\alpha \leq 1)$ the activation occurs through a more homogenous and much slower process as shown in Fig. 4.5 (a). Comparing the two cases in Fig. 4.5 (a-c) it is possible to see how for $\alpha > 1$, even for low level of

injected charge, a single electrical path percolates the film. A further increase of the current compliance will lead to the formation of a second percolating path. In contrast, when $\alpha < 1$, the current flows in the network through several electrical paths for the same level of injected current.

4.3 Experimental observation of the conductance plateaus and WTA path

In order to study the formation of plateaus within macroscopic networks, it is necessary to increase the sampling rate used for the compliance current. Fig. 4.6 shows an example of an experiment designated to isolate and highlight the plateaus during the activation of the network. Initially the current sampling used to activate the sample is the same as that used in Fig. 4.1 where for each decade, four different compliances are selected (i.e. $100nA - 250nA - 500nA - 750nA - 1uA$).

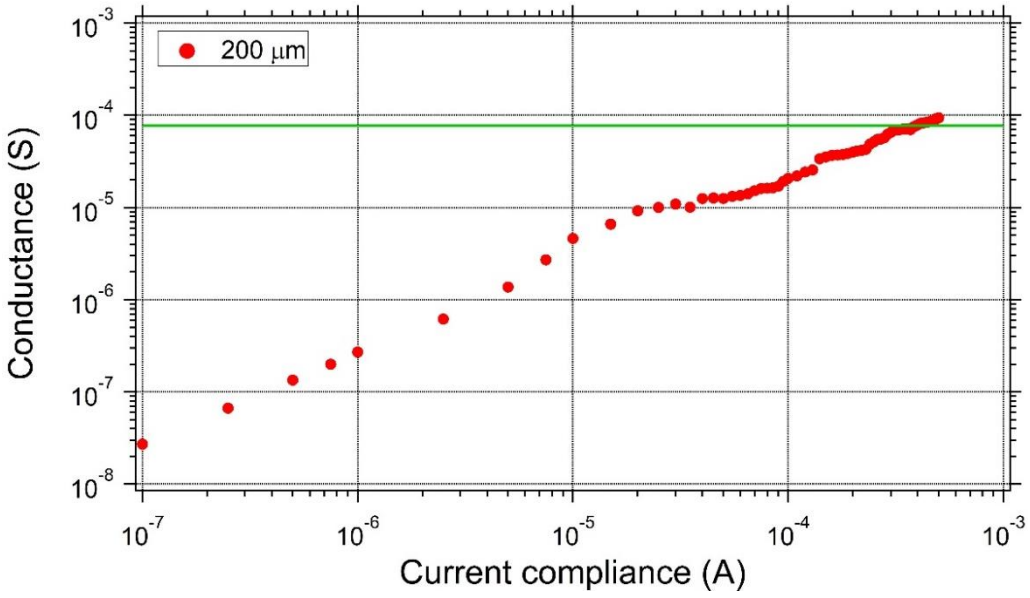

Fig. 4.6 Conductance versus compliance plot for an Ag $200 \times 200\ \mu m$ network using fine current sampling steps that shows the presence of plateaus well below the QCP highlighted in green.

During experiments whenever the range of compliances approached the levels in which the plateaus are expected to appear, the sampling rate (compliance steps) is further increased as shown below in Fig. 4.7. A zoom of the region under investigation highlights the formation of plateaus previously shown by the simulation in Fig. 4.3 and Fig. 4.5.

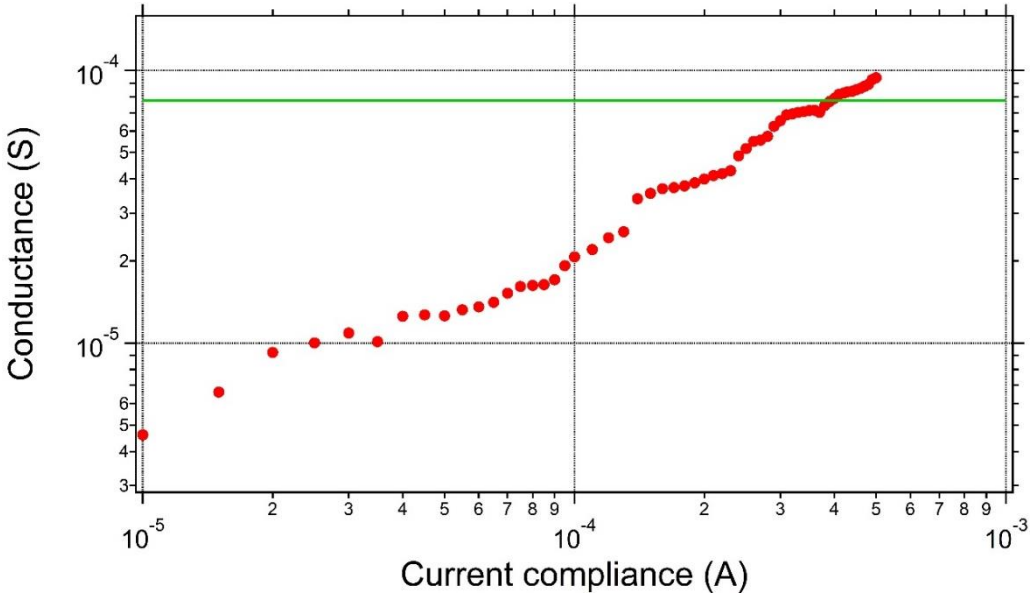

Fig. 4.7 Zoom in of Fig. 4.6 in the proximity of the first plateau that highlights the presence of several steps below the QCP (green line).

It can be noted how the shape of the plateaus obtained from an Ag NW network of $200 \times 200\ \mu m$ results much smoother than those found in the simulation of Fig. 4.5. One reason for this difference is the finite current resolution in experiment. The second is due to assumption in simulations of fixed α and A values. In reality, the conductance of the junctions within the network can vary and that the assumptions $\Gamma_{off} = 10^{-7} S < \Gamma_j < \Gamma_0 = 7.75 \times 10^{-5}\ S$, that is that junctions increase conductance up to the QC level and then stop, does not hold experimentally. As demonstrated in the first chapter, when a CF grows within the active layer, the conductance reaches the QCP (Γ_0) when the conductive filament that bridges the electrodes ends with a single atom [6–8]. Further electrical stress will cause a strengthening of the CF resulting in multiple channels and a conductance level that will be multiple integers of Γ_0 as described by

Tappertzhofen et al [8]. The experimental evidence in Fig. 4.6, we show that in networks we obtain conductances that are instead fraction of Γ_0 corroborating results from our simulation. Fig. 4.8 shows that these plateaus correspond to the formation of a series of n quantum conductors connecting the two electrodes for each of the different NWNs sizes.

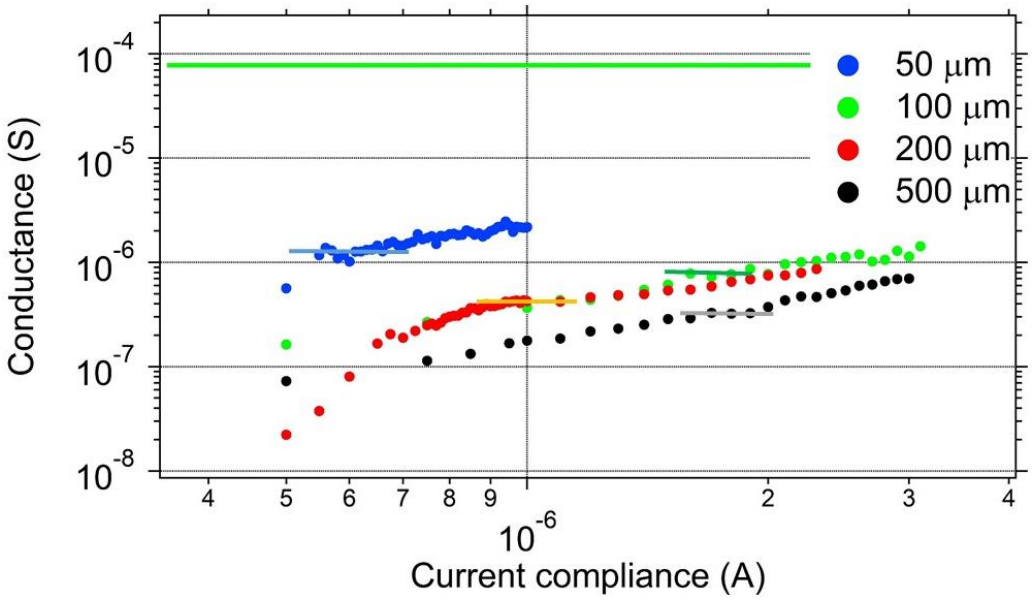

Fig. 4.8 Comparison between the conductance curves obtained for Ag NW networks with different electrode distances. As described in equation (4.3), the presence of the plateau depends on the number of junctions within the electrical main path. Consequently, smaller samples have plateaus closer to the quantum of conductance level. Moreover, as the sizes of the network become wider, the formation of a percolating path involves more junctions lowering then the position of the plateau. Here, the plateaus for four different network sizes are highlighted by horizontal lines and the estimated number of junctions are reported in table 4.2. The green solid line represents the QCP level $\Gamma_0 = 7.75 \times 10^{-5}$.

The plateaus of smaller networks are always closer to the QCP (green line in Fig. 4.8) indicating that a lower number of junctions is involved in the conduction path. Therefore, identifying the conductance at the plateau as Γ_p we have:

$$\Gamma_p = \frac{\Gamma_0}{n} \qquad \text{Eq. (4.3)}$$

where Γ_0 is the quantum of conductance and n is the number of junctions required to bridge the electrodes. It is possible to do a rough estimation on the minimum

number of NWs required to bridge the electrodes considering a NWN made of Ag NWs with an average length being $6.7\ \mu m$ (see Fig. 2.16). In the most idealized case, for a network with $50\ \mu m$ electrode-electrode separation and considering that all NWs are perfectly aligned towards the electrodes, at least 8 NWs (9 junctions) are necessary to electrically connect the electrodes. However, for such a complex system and due to the high randomness nature of the film, this condition is very unlikely to happen. Calculating instead the number of junctions n from Eq. 4.3 for the $50\ \mu m$ network (Γ_p from the blue solid line in Fig. 4.8) gives a number of junctions $n = 64$. Table 4.2 shows the values extrapolated from Fig. 4.8, using Eq. 4.3, of the number of junctions participating in the current conduction through the network. It is important to remark that despite the randomness of the film, a direct comparison between different networks is possible since the density of NWs is maintained always constant.

Table 4.2 Conductance of the plateaus $\Gamma_p\ (\mathrm{S})$ is shown as the distance between the electrodes increases. The estimation of the number of junctions n participating in the electrical path is performed from the plateau levels in Fig. 4.8 using equation (4.3) as $n = \Gamma_0/\Gamma_p$.

NWN size	$\Gamma_p\ (S)$	n
50 μm	$1.22\ 10^{-6}$	64
100 μm	$7.57\ 10^{-7}$	102
200 μm	$3.25\ 10^{-7}$	205
500 μm	$3.78\ 10^{-6}$	240

Although the numbers reported in Table 4.2 are extrapolated from Γ_p level, it is necessary to consider that we are oversimplifying the problem just to prove that the numbers in table 4.2 reflect the reality of the increasing network size. In fact, as reported by O'Callaghan et al [9], the calculation of the number of junctions in such complex systems can be very challenging. Several reports [9–12] have highlighted the fact that the number of junctions within random networks is strongly related to the number of the wire present in the mesh. Furthermore, the

implementation of geometrical parameters such as the area of the wire and the contact probability increases dramatically the difficulty of the problem. In order to visualize the conducting NWs in networks under electrical stress, we decide to use passive voltage contrast technique [13].

4.4 Visualization of WTA path in NWNs

In this section, an extensive study on networks of different dimensions is undertaken to visualize the WTA path formation at the early stages of the activation. An example of a $20\ \mu\mathrm{m}$ Ag NWN electrical stressed with repeated high compliance current sweeps is shown in Fig. 4.9.

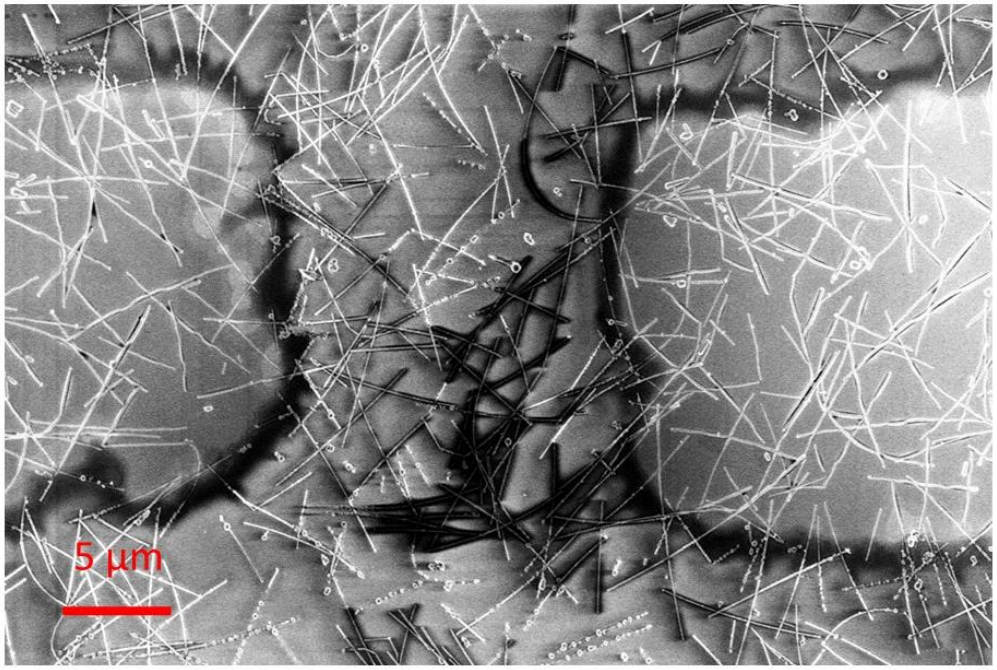

Fig. 4.9 Passive voltage contrast image [13] that shows which areas of a Ag nanowire network have been activated after several I-V sweeps with a compliance equal to $10\ mA$.

The network was intentionally stressed to permanently activate the junctions within the film and create a solid connection between the two electrodes. Thanks to the low energy incident beam ($2\ kV$), the electrons accumulate on the surface showing a contrast between the floating and the grounded NWs (see section

2.1.2.2). Due to high level of electrical stress imposed to the network, the charge on the activated NWs was able to fade away giving a darker contrast, highlighting the conduction path. Fig. 4.10 (a) shows the SEM chamber equipped with the Kleindiek Nanotechnik micromanipulator, used to contact the Ag NW network and perform the electrical measurements. The electron gun appears on the top of the image in Fig. 4.10 (a) and points towards the sample that is attached by a carbon tape onto the SEM stage. An image of the actual sample and the two electrical probers in contact with the sample is shown in Fig. 4.10 (b). An external system enables the movement of the probers and contacting of the network pads, while a Keithley digital multimeter Model 2000 was used to source the voltage to the sample.

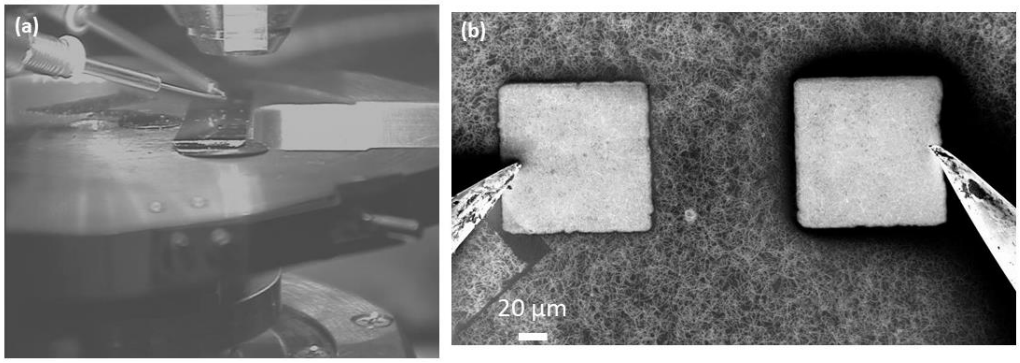

Fig. 4.10 In (a) the image shows the SEM chamber. The micromanipulator approaching the sample from the left side are used to electrically interrogate the network while the end of the SEM column is visible right on the top of the sample. In (b) an Ag NW network with an electrode (Ti/Au $-\ 5/35nm$) distance $d = 100\ \mu m$ contacted with the Pt probers.

The aim of this study is to show the formation of the initial WTA and the evolution of the NWNs resulting in the formation of different current paths. From both simulation and the experimental evidence we know that the path at the early stage of the activation is self-selected (see Fig. 4.5). Along the activation curve ($\Gamma\ \times I_{cc}$ plots), in the PL regime, the CFs within the junctions are strengthened by the current flowing through the film. Once the main path is fully optimized, at the plateau, alternative electrical paths will emerge increasing the conductivity of the

network approaching the PPL regime. Therefore, the following three sections describe the stages a network experiences during the activation.

4.4.1 OFF and Transient regimes – Path selection

The first example that shows the preliminary stage of the activation, OFF and TG states referring to Fig. 4.4, is reported in Fig. 4.11. An Ag NW network with an electrode distance of $200\ \mu m$ is kept under the threshold voltage V_{on} required to activate the network ($18\ V$ for this particular case). In this condition, the system is in a precursor forming stage, TG regime, in which almost all the junctions in the network are stressed through the application of a very low voltage resulting in current in the pA range. Through this voltage application the network ultimately selects the least resistive paths and once sufficient current is supplied to the network the WTA path is formed.

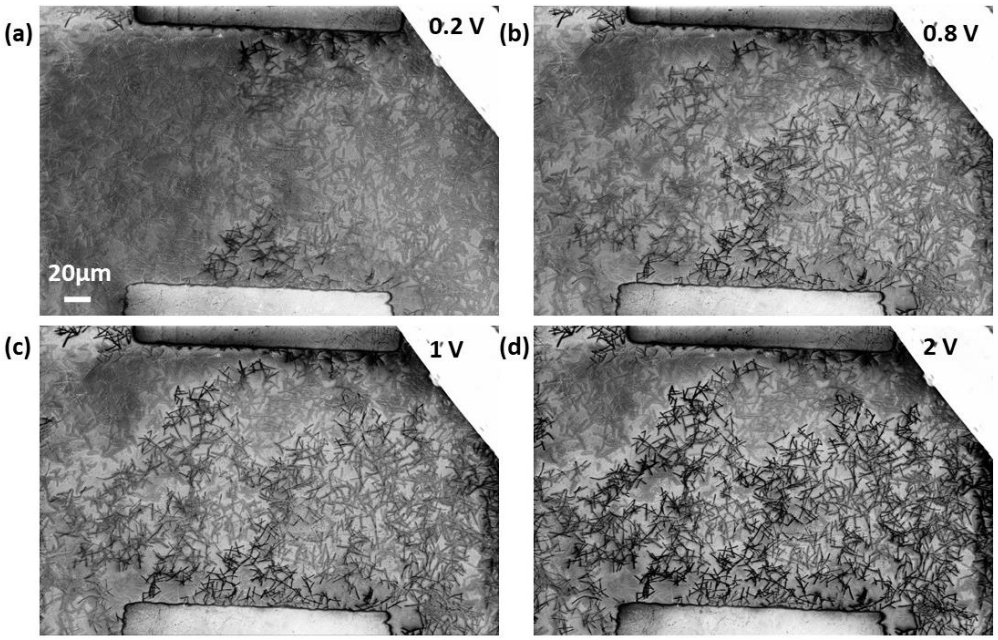

Fig. 4.11 Passive voltage contrast images showing the Ag nanowires prior to any electrical activation due to the low currents involved ($\approx pA$). At this stage, the network is in a transient regime in which it self-selects the more efficient path to connect the electrodes. The darker contrast is due to the voltage that increased gradually and redistributed homogeneously over the film going from (a) to (d).

In Fig. 4.11 (a), a voltage of $0.2\ V$ is applied to the sample and an overall current of several tens of pA is flowing through the entire film. The bottom electrode, that appears brighter, is under a constant voltage and as a consequence, the electrons are unable to leave the surface of the sample. On the other hand, the charge on the top electrode is free to leak since the electrode is grounded. Initially, when $0.2\ V$ is applied to the network, only few NWs show a dark contrast since the electrodes voltage is too low as to facilitate charge to leak from NWs. The increase of the voltage allows additional nanowires to leak charge and in doing so samples the connectivity paths across larger regions of the network. The behaviour of the network in the regime is similar to that of a leaky capacitor. The application of a voltage forces the accumulation of charges on a side of the capacitor. If the potential difference between the two plates is not enough, the charge will remain on one side, however when the potential overcomes a certain threshold, the electrical breakdown of the insulating layer enables the conduction of charge. The same process is also happening in the network shown Fig. 4.11; once the voltage overcomes a certain threshold (V_{on}), the current starts to flow, and the formation of CFs within the junctions begins. As discussed earlier, this condition is well described by the capacitance model discussed in section 3.2.3. Each junction is represented by a binary capacitor that can be at an ON or OFF state. However, once the WTA path is chosen, the capacitance model is no longer able to describe the connectivity evolution; it is then necessary to switch to the memristive model [4] that can account for the response to the system to charge flow. A memristive description in the form of a variable gap model allows for the formation and the evolution of CFs within the WTA path, as discussed in the next section.

4.4.2 Power law regime - WTA path

Once again an Ag NW network is used to highlight the presence of the WTA path. The as-deposited Ag NW network ($d = 100\ \mu m$) in Fig. 4.12 (a) is imaged to determine the initial configuration of the sample prior to the application of any voltage. A voltage dual sweep $0 - 20\ V$ is applied to the system and a V_{on} equal

to $14\ V$ was found. Immediately after the end of the voltage sweep ($I_{cc} = 50\ nA$), both probes where grounded to facilitate the flow of electrons and to help to visualize the activation paths within the NWNs as shown in Fig. 4.12 (b). This set compliance level corresponds to the early stage of the PL regime.

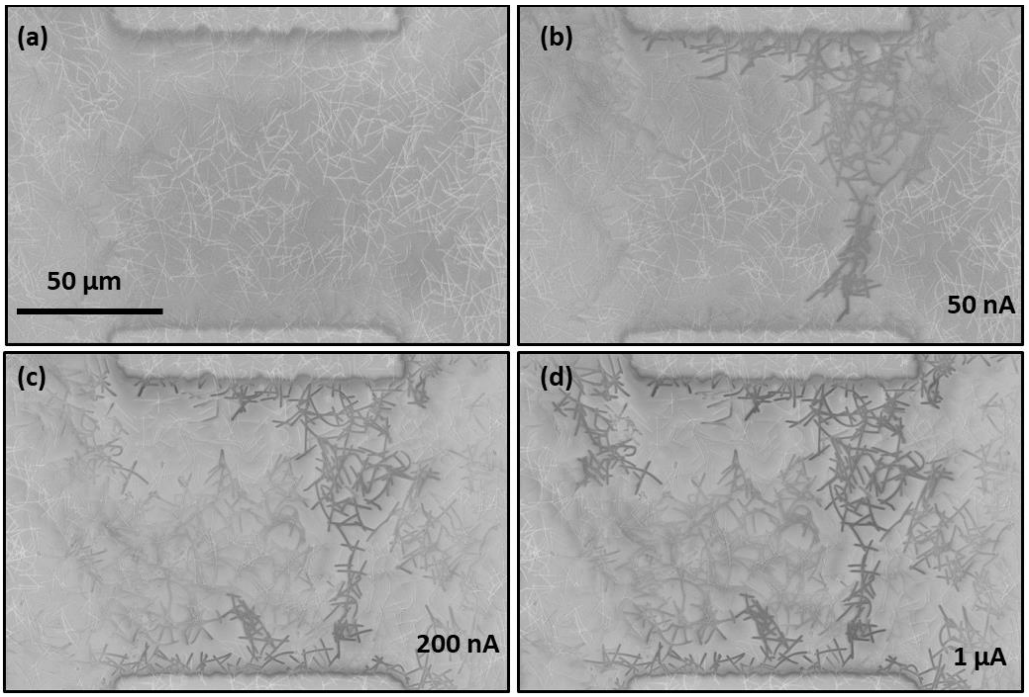

Fig. 4.12 $100\ \mu m$ silver network used to visualize the formation of the WTA path. The network initially at the OFF state is shown in (a). A voltage sweep is subsequently performed using a compliance of $50\ nA$ as can be seen from (b). The network self-selects the least energy path. Increasing the I_{cc} to $200\ nA$, (c) case, helps to strengthen the CFs inside the junctions and their respective wires gain a darker contrast in the image. Moreover, in (d) a compliance of $1\ \mu A$ is sufficient to optimize the WTA and to create the second electrical path that from the top right corner points to merge with the part of the network that is already being activated by the previous voltage sweeps.

Fig. 4.12 represents the first visual confirmation that in the power law PL regime, the WTA path is already established, and the electrical energy injected by the voltage sweeps is dissipated only at the junction along the WTA path. Moreover, increasing the compliance up to $200\ nA$, Fig. 4.12 (c), results in a further enhancement in the contrast along the activated NWs within the WTA path. This change in contrast is due to strengthening of the junctions progressively becoming

more and more conductive (closing of the tunnelling gap). A further increase of the compliance to $1\ \mu A$ causes the formation of alternative paths from the top electrode showing that the system has now entered in the PPL regime. If we now go back to the extrapolated number of junctions made in table 4.2, it is possible to confirm that the number of junctions involved in the conduction is very close to what is reported in table 4.2. Fig. 4.12 (c), which correspond closely to the plateau condition for a $100\ \mu m$ network roughly shows 100 junctions are participating to the WTA path, consistent with in Table 4.2.

4.4.3 Post-Power Law regime - Multiple paths

Once the system enters the PPL regime, different parallel paths are responsible for the conduction. Here, a separate $100\ \times 100\ \mu m$ network is used to visualize this condition. As before the network is activated through a voltage sweep but a larger current compliance of $10\ \mu A$ (comparing with Fig. 4.12) is used to activate a larger area of the sample. The SEM images in Fig. 4.13 (a-b) show the network before and after the voltage sweep.

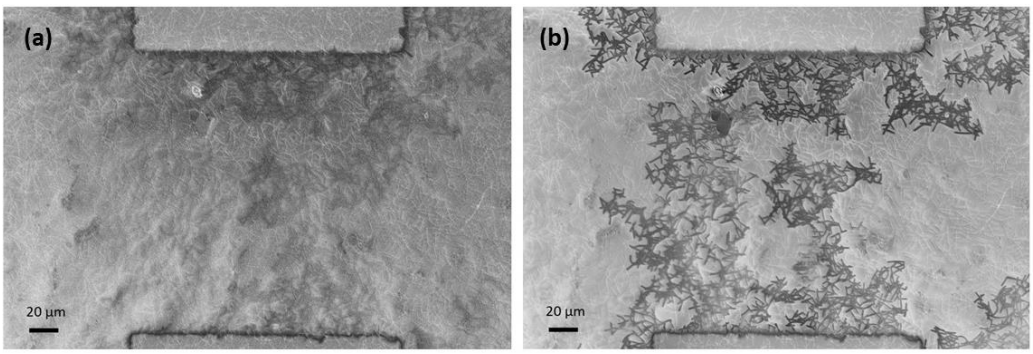

Fig. 4.13 In (a) a $100\ \mu m$ silver network is imaged before the electrical tests while in (b) the same network after a voltage dual sweep with a $10\ \mu A$ current compliance. The two separated electrical paths are visible in (b).

In Fig. 4.13 (b), two separated paths are visible. The first electrical path on the left side of the image is most likely the WTA path while the second path on the right side is starting to merge. Clearly the injection of additional current creates multiple

paths that hugely increases the number of junctions participating to the conduction in the film. Therefore, to describe in deeper details the activation next section discussed the formation of electrical paths from an energy dissipation point of view.

4.5 Energy dissipation within NWNs

The vast number of measurements and calculations of electrical conductance in nanowire networks enable us to analyse and to estimate the power dissipation through the samples. Fig. 4.14 shows the experimental $\Gamma \times I_{cc}$ data obtained from a $500 \times 500\ \mu m$ Ag NW network that will be used throughout this section to interpret the results in terms of the conductance power laws and current trends.

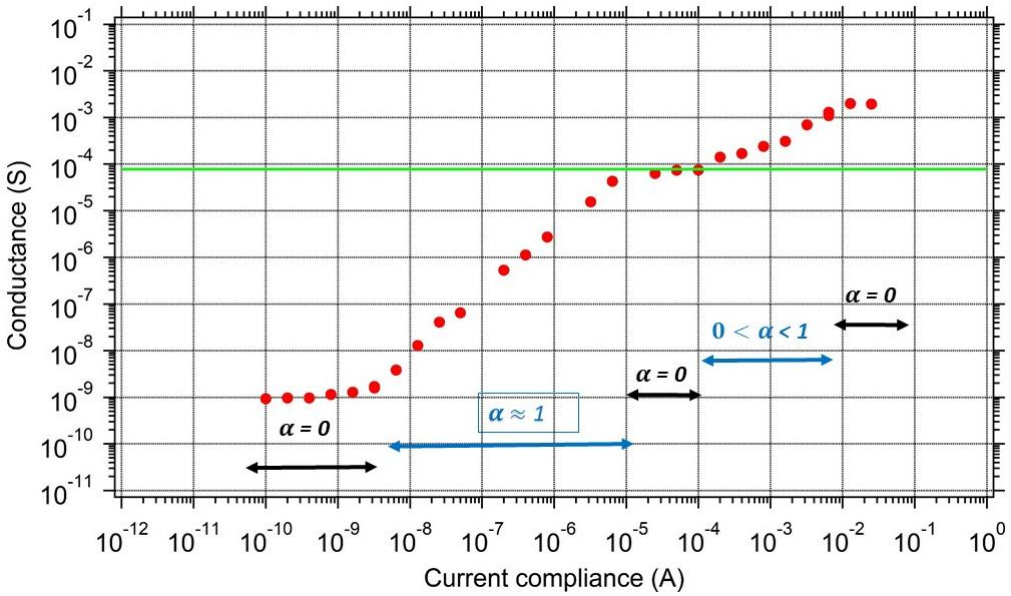

Fig. 4.14 Conductance vs current compliance plot obtained from a $500 \times 500\ \mu m$ Ag NW network that shows four different stages in the activation curve. If power laws were used to fit distinct sections of the curve, their exponent values α would fluctuate as depicted in the panel.

In order to estimate the power dissipation within the system we have to start from Eq. (4.4). Electrical power can be expressed in terms of current I and conductance Γ as $P = I^2/\Gamma$. For a nanowire network, we have $\Gamma_{nt} =$

$A_{nt}I^{\alpha_{nt}}$ with α_{nt} fluctuating around 1. For the sake of notation simplicity, we express $A_{nt} = A$ and $\alpha_{nt} = \alpha$. The power dissipated on the network is then given by

$$P = I^{2-\alpha}/A \quad \text{Eq. (4.4)}$$

Note that a new exponent can be associated with the power, i.e. $\beta = 2 - \alpha$ and that in regions of Fig. 4.14 containing well-defined conductance plateaus, $\alpha = 0$, and hence $\beta = 2$. Combining now the results of Fig. 4.14 with Eq. (4.4) we can describe the activation in terms of power dissipation within the film. At the first stage of the activation, the current supplied to the system is very low and it is not sufficient to change the total conductance of the network. As soon as the current is sufficient to create a connection between the electrodes (WTA path), the change in conductance curve is accompanied by a change in power dissipations. Within the PL conductance regime, the power supplied is used to create conductive filaments within the junctions which enables a gradual current-flow through the network. Therefore, we infer that the energy dissipation is responsible for two distinct conduction effects in nanowire systems. One is related to the closure of the tunnelling gap within the junctions through energy for the corresponding redox reaction [14,15] and a second one due to the conduction itself that strongly depends on the electrical history of the sample and its memristive characteristics (i.e. $\Gamma(I,t)$). In this regime, the network dissipates power in the most efficient manner with $\beta \cong 1$. In other words, the network dissipates power in a linear fashion with the injected current and hence non-ohmic. When approaching the first plateau roughly at $10\ \mu A$, $\alpha = 0$ and the power varies quadratically with the current. In this condition, all the power injected into the network is dissipated through Joule heating [16,17] since the junctions within the WTA are optimized and hence the electrochemical reaction has ceased and thus behaves as a system of ordinary resistors in series. Supplying further energy in the PPL regime produces more paths that will continue to be optimized in parallel to the already established WTA path. In this regime, the power law between the first and second plateaus has an exponent $\alpha = 0.73$ and consequently a power exponent equal to $\beta = 1.27$. This indicates that the overall power of the network is non-ohmic once again,

but it is being dissipated in the most efficient manner as in the WTA stage since $\beta > 1$. As the network activates more and more parallel paths, its electrical response will evolve towards the one of an ordinary resistor with $\beta \to 2$ with nearly 100% of its power being dissipated through Joule heating. Simulated results for the conductance and power evolution in an Ag nanowire network are shown in Fig. 4.15. There one can see how the differences in conductance exponents directly affect the power evolution in macroscopic networks as previously discussed.

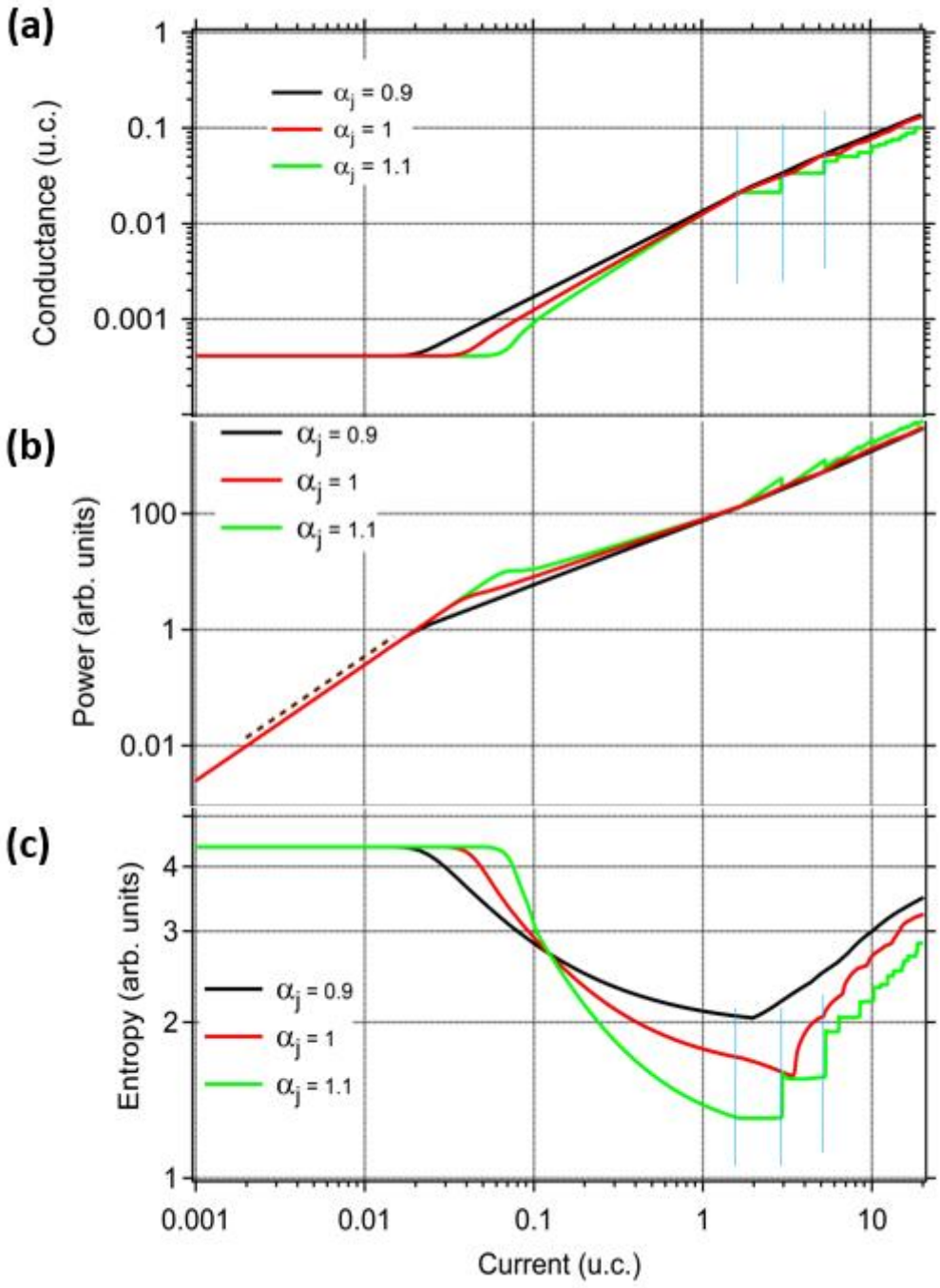

Fig. 4.15 The simulated data of Fig. 4.3 are used here to extrapolate the power and entropy along the activation of a network. In the $\Gamma \times I_{cc}$ plot (a) the three different curves represent different α values. The power in (b) is calculated from the conductance data on the panel (a) using Eq. (4.4). The dashed black line is an eye-guide line with an exponent equal to two. While in (c) the mathematical entropy is calculated from Eq. (4.5). The minimum in the entropy plot demonstrates how the formation of a single path bridging the electrodes represents the lowest energy-consuming path. The blue lines in (a) and (c) mark the beginning of each plateaus.

Another quantity that can be used to quantify the network efficiency in transmitting current through its skeleton using the least amount of junctions possible is the so called Von Neumann entropy [18]. In the context of network information theory, the WTA can be interpreted as a state of minimum entropy/uncertainty in which the sourced signal is convolved into a single conducting path rather than spread into multiple current-carrying paths across the network. By computing the Von Neumann mathematical entropy, we are able to identify this minimum and to determine the current ranges in which the network propagates signals more efficiently by dissipating the least amount of power. As described in the third chapter, the network, after the digitalization process, can be mapped onto the Kirchhoff matrix where the conductance of each junction and inner segment are an element in the matrix [19]. This matrix contains all conduction and connectivity information of the network and it can be interpreted as the Laplacian matrix of a weighted mathematical graph [20] from which useful properties about the network can be obtained. For the sake of simplicity, we will omit the details of such entropy calculation and describe only the key points. The mathematical Von Neumann entropy is given by $S = -tr\ (\rho\ ln\rho)$ [21] where the entropy is calculated using the trace of the density matrix ρ. Making the eigen decomposition of ρ in terms of the eigenvalues and eigenvectors associated with the j^{th} junction within the network as $\rho = \sum_j n_j |j\rangle \langle j|$, the entropy can be written as

$$S = -\sum_j n_j ln\ \ n_j \qquad \text{Eq. (4.5)}$$

The calculated entropy is shown in Fig. 4.15. There one can see the entropy reaching its minimum when the WTA is fully optimized for $\alpha > 1$. For networks made with junctions of $\alpha \leq 1$, a minimum in the entropy is also observed however, since these exponent values do not favour WTA formation, their minimum entropy values are considerably higher than for the case with $\alpha > 1$. This confirms that the WTA state is the most favourable condition for signal propagation in nanowire networks as it compresses information into a single path avoiding then loss of information through current leakages in the device. Once the junctions of the WTA are fully optimized the formation of a different electrical

path is highlighted by the presence of the second plateau (see blue vertical lines in (a) and (c)). The entropy follows the jump of the conductance trace reaching a new equilibrium state associated to a larger entropy value. In this condition the information can travel along parallel path increasing the possibility to have leakage current and the consequent loss of the information.

4.6 Conclusion

Within the fourth chapter we have introduced the self-similar scaling law that regulates the activation process in single wire devices and networks. Despite the huge difference in terms of dimensions we prove how the formation of CFs within junctions govern both the system at a micro and macroscopic level. The precious work done with the simulations by our collaborators helped to confute our hypothesis further enhancing the quality of the results obtained.

The hint provided by the formation of plateaus in the scaling curve ($\Gamma \times I_{cc}$) led us directly to the most important discovery done during this PhD project the formation of WTA path. Thanks to the PVC technique we were able to visualize the formation of electrical paths within the network and define four different regions along the activation of the film. Through the simulations the Von Neumann entropy enables us to show how the WTA paths correspond to the most efficient to make electrical connections between the electrodes.

The following chapter will be used to give a general overview of different materials used during this study to implement switching properties to the network that are naturally absent considering Ag NWs.

References

1. Balatti, S., Larentis, S., Gilmer, D. C. & Ielmini, D. Multiple Memory States in Resistive Switching Devices Through Controlled Size and Orientation of the Conductive Filament, (2013).
2. Manning, H. G. et al. Emergence of winner-takes-all connectivity paths in random nanowire networks, (2018).
3. Thomas, S., Prakash, S. & Priya, K. Characterization of memristor based on non-linear ion drift model, (2017).
4. O' Callaghan, C., Rocha, C. G. & Niosi, F. Capacitive and memristive behaviours in metallic nanowire networks, (2018)
5. Sannicolo, T. et al. Direct Imaging of the Onset of Electrical Conduction in Silver Nanowire Networks by Infrared Thermography: Evidence of Geometrical Quantized Percolation, (2016).
6. Oliver, S. M. et al. Quantum point contacts and resistive switching in Ni/NiO nanowire junctions, (2016).
7. Melliz, M. B., Pollinit, A. & Melli, M. Quantum conductance in single- and double-wall carbon nanotube networks Quantum conductance in single- and double-wall carbon nanotube networks, (2007).
8. Tappertzhofen, S., Valov, I. & Waser, R. Quantum conductance and switching kinetics of AgI-based microcrossbar cells, (2012).
9. O 'Callaghan, C., Gomes Da Rocha, C., Manning, H. G., Boland J. J. and Ferreira, M. S. Effective medium theory for the conductivity of disordered metallic nanowire networks, (2016).
10. Bellet, D. et al. Transparent electrodes based on silver nanowire networks: From physical considerations towards device integration, (2017).
11. Behnam, A. & Ural, A. Computational study of geometry-dependent resistivity scaling in single-walled carbon nanotube films, (2007).
12. He, S., Xu, X., Qiu, X., He, Y. & Zhou, C. Conductivity of two-dimensional disordered nanowire networks: Dependence on length-ratio of conducting paths to all nanowires Enhanced light trapping in Ge-on-Si-on-insulator photodetector by guided mode resonance, (2018).
13. Z. Gemmill, L. Durbha, S. Jaconson, G. Gao, K. weaver. SEM and FIB Passive Voltage Contrast, (2017).
14. Sawa, A. & Meyer, R. Resistive Switching from fundamentals of nonoionic redox processes to Memristive Device Applications, (2016).
15. Chang, T.-C., Chang, K.-C., Tsai, T.-M., Chu, T.-J. & Sze, S. M. Resistance random access

memory, (2016).

16. Sorel, S., Bellet, D. & Coleman, J. N. Relationship between material properties and transparent heater performance for both bulk-like and percolative nanostructured networks, (2014).
17. Jeong, W., Kim, K., Kim, Y., Lee, W. & Reddy, P. Characterization of nanoscale temperature fields during electromigration of nanowires, (2014).
18. Petz, D. Entropy, von Neumann and the von Neumann entropy, (2001).
19. Kirkpatrick, S. Percolation ancl Conduction, (1973).
20. Guichard, D. An Introduction to Combinatorics and Graph Theory, (2018).
21. Bengtsson, I. & Zyczkowski, K. Geometry of quantum states: An introduction to Quantum Entanglement, (2006).

Chapter 5

Other network materials

The third and fourth chapters contained a detailed description of the electrical activation processes in Ag NW networks. Starting from this base, this chapter gives an overview of other materials and networks studied in this PhD project. The first part of the chapter demonstrates how NWNs, made of different materials, exhibit the same self-similar conductance scaling law discussed in the previous chapter. Although a wide range of materials behave as Ag NWs do, the most important difference is the value of the power law scaling exponent α obtained from the $\Gamma - I_{cc}$ curves and consequently the strengthening coefficient for the network. The main reason to investigate the behaviour of other materials is to address the networks properties that are not easily elucidated in the case of the Ag@PVP NWNs. In the following, the focus will be moved to the investigation of the electrical behaviour in terms of switching capabilities. Analysing the electrical characteristics of $AgTiO_2$ networks we have found a nonpolar characteristic behaviour that can be modulated by the use of the compliance current. This proves that the properties of single NWs can be transferred to networks.

Moreover, two examples of unipolar resistive switching (URS) behaviour will be shown in the case of Cu and Ni NWNs prior to conclude the chapter with a brief section summarizing the qualities of NWNs made with materials that have switching characteristics.

5.1 Same scaling, different materials

As stated in the introduction, we will now show that the mechanism of activation is a common property of NWNs. Through the theory described in the third chapter, we are able to describe the conductance evolution with current within networks of different materials. Fig. 5.1 shows results obtained for several NWN systems including Cu@CuO_x, Ni@NiO_x and Ag@CTAB that will be further discussed in this chapter. Even from a preliminary analysis, it can be noted how the conductance of the networks, regardless the dimension of the devices, tends to follow the scaling trend introduced in the fourth chapter.

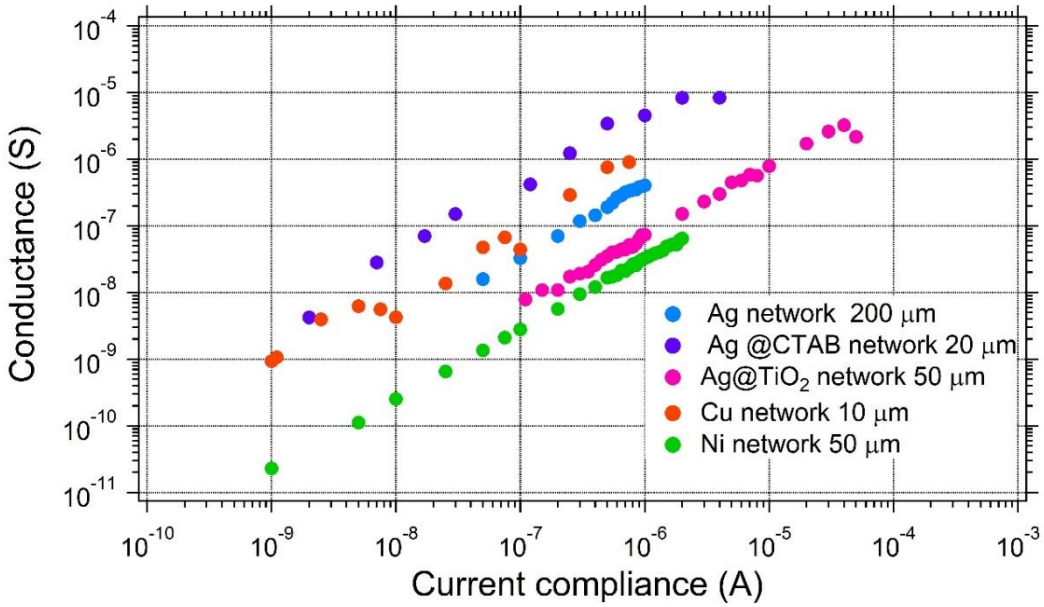

Fig. 5.1 Γ vs I_{cc} plot for different network materials. Can be noted how all the curves, regardless the dimension of the device have practically the same slope. On the other hand, the A_{nt} coefficient varies over a much broader range considering the different materials.

From a simple comparison between the curves we note that the α_{nt} values are close each other while the A_{nt} values (intercepts) show a wide spread with different types of NWs materials. Later, referring to the ion-drift model we show that one reason for these differences is associated with the different mobility of the ions within the active layers. Furthermore, in the next section we show the

conductance behaviour of four different networks starting from the Ag based materials.

5.1.1 Ag based materials

Ag@CTAB

The first case presented is about a network made of Ag@CTAB nanowires. The nanowires were fabricated by our collaborators at University College Cork (UCC) through chemical reaction using $AgNO_3$ in an ascorbic acid ambient [1]. The dissolution of the salt provides Ag NPs that are used as seeds and dispersed in a mixture of H_2O and CTAB [2]. The CTAB in solution acts exactly as the PVP does in the formation of the Ag@PVP NWs [3,4] favouring the formation of the NWs in a particular direction [3]. The solution obtained from the process is then drop casted onto a silicon substrate to test the quality of the nanowires through SEM analysis. Representative SEM images are shown in Fig. 5.2 and as can be seen from Fig. 5.2 (a) the quality of NWNs are quite good. However, closer inspection of Fig. 5.2 (b) shows the presence of wire bundles and clumps influencing the quality of the network.

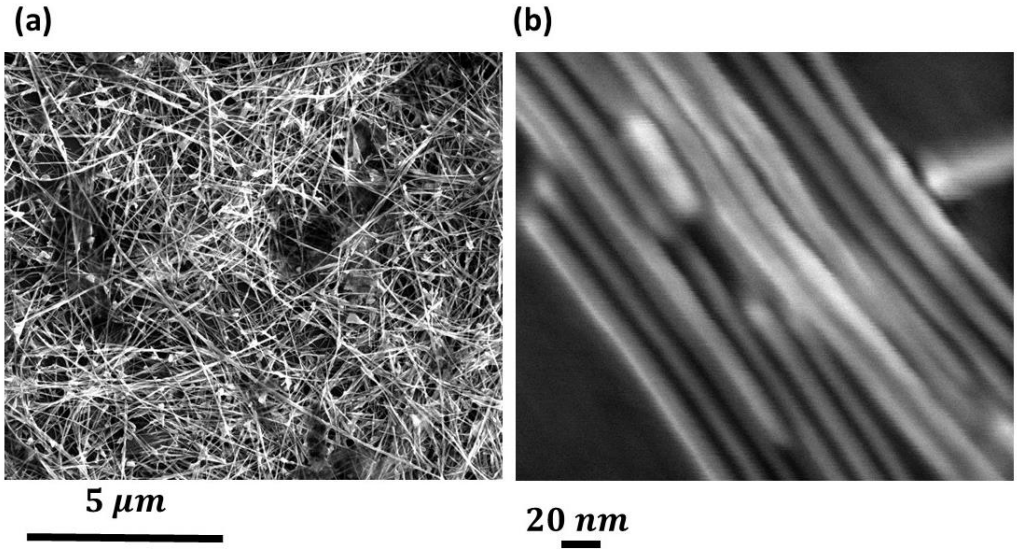

Fig. 5.2 SEM image of Ag@CTAB nanowires (a) deposited on a silicon substrate. In (b) a zoom highlights the fact that the NWs are not very dispersed in solution but instead they tend to form bundle of wires.

After drop casting the solution the electrodes were formed using a shadow mask as described in section 2.2.3 of the second chapter. The samples were then imaged using SEM before, see Fig. 5.3 (a), and after the electrical measurements, as shown in Fig. 5.3 (b-d). A conventional two probe approach was used to perform the measurements in which the electrode on the right side was subjected to a positive bias while the left one was grounded. The actual networks (of dimensions $20 \times 20\ \mu\mathrm{m}$) are shown in Fig 5.3 (a). Although a brief sonication is useful to separate the NWs, we opted not to apply any further processing to prevent any possible deterioration of the NWs quality. Unfortunately, due to the poor quality of the coating layer, the devices are unusable after the first series of tests as highlighted from Fig. 5.3 (b-d). We observed the accumulation of what we believe is CTAB on the grounded electrode; under electrical stress the CTAB layer that cover the NWs migrates from one electrode to the other showing a very poor adhesion between the Ag and the CTAB layer.

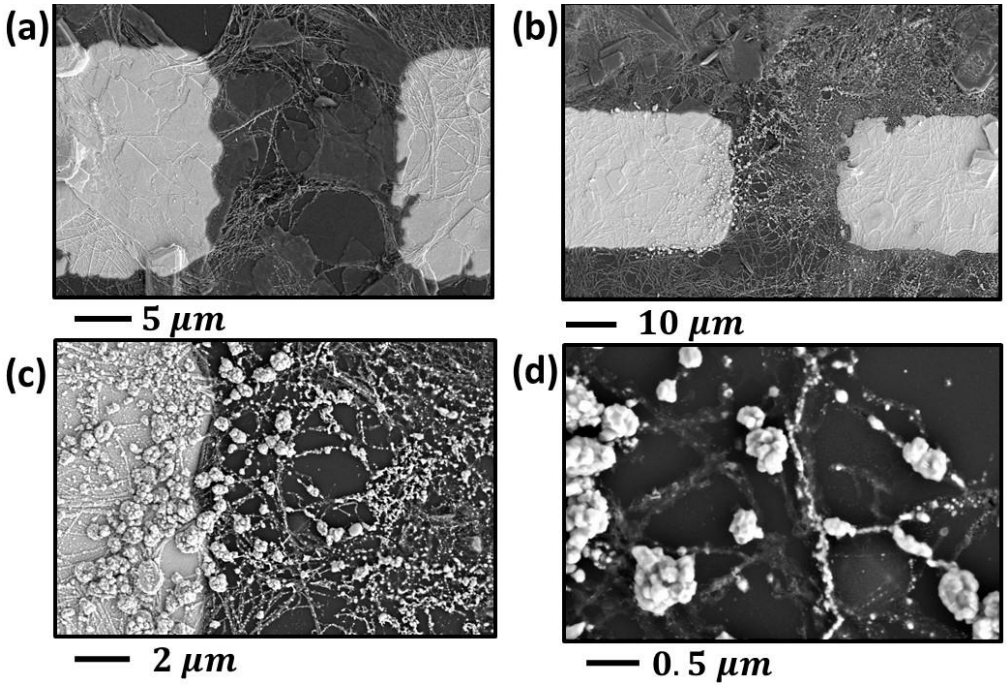

Fig. 5.3 As-dropcast sample contacted through a Ti/Au - 5/35 nm metal deposition (a). The network is very inhomogeneous as the NWs have tendency to form bundles all over the surface. Increasing zoom on the sample (b-d) after the electrical tests can be noted the accumulation of CTAB molecules on the grounded electrode.

Despite after the CTAB diffusion the electrical measurements were recorded, the results from a $20 \times 20\ \mu m$ network are reported in Fig. 5.4. As already highlighted from Fig. 5.1, the scaling law remains valid even for the Ag@CTAB NWs case. From the fit, the α value is equal to 1.05 indicating an activation process similar to the Ag@PVP networks.

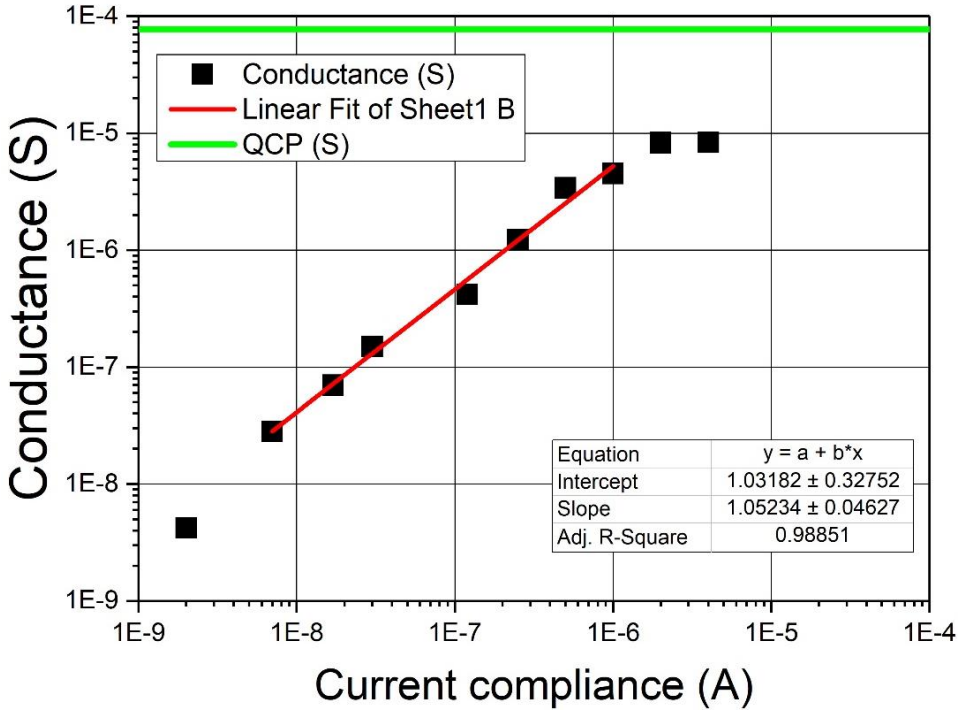

Fig. 5.4 Conductance versus current compliance curve obtained from the Ag@CTAB network present in Fig. 5.3 (b) with electrodes separated by $20\ \mu m$. From the linear fit on the log-log plot the slope of results to be equal to 1.05. The green line represents the quantum conductance point level $\Gamma_0 = 7.75 \times 10^{-5} S$.

These electrical measurements prove that the use of CTAB coated NWs behaves similarly to PVP coated Ag NWs. However, due to the poor adhesion of the coating layer onto the Ag internal core, we decided to focus our attention on more robust structures such as core-shell NWs.

Ag@TiO_2

Another example of device driven by the drift of the Ag ions is the core-shell structure Ag@TiO_2. A TEM image of the NWs, prepared in UCC, can be found in Fig. 2.17 (a). The procedure to create the NWs involves an initial step to create Ag@PVP NWs via polyol reduction process (see section 2.5.2) [3,4]. In a second step, the PVP is removed from the surface of the wires and replaced with the TiO_2 layer using a thioglycolic acid mediated process [5,6]. Further information on the

procedure used can be also found in the report by Manning et al [6]. The NWs were then spray-deposited on the substrate to create single wire devices as Fig. 5.5 (a) [6] and networks shown in Fig. 5.5 (b).

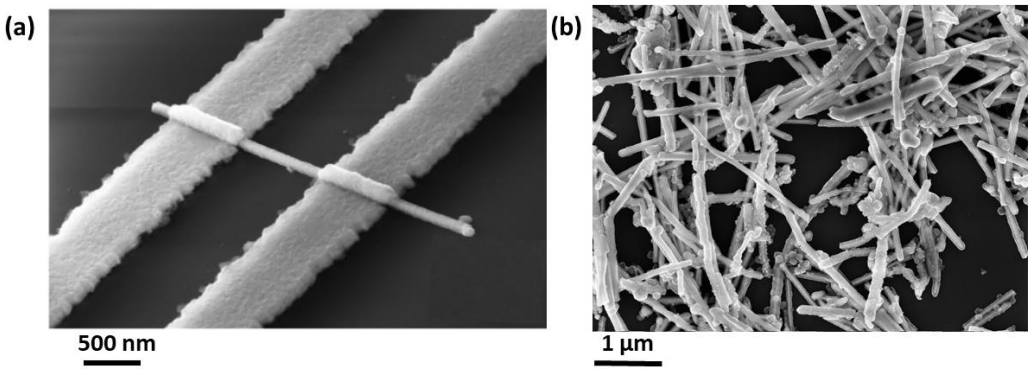

Fig. 5.5 A single Ag@TiO_2 wire device contacted through an Ag metal deposition in (a) while in (b) a SEM image of the network before the metal deposition to realize the electrical contacts. The coating is very homogenous along the NWs and further investigations have proven that the shell is made of a polycrystalline rutile TiO_2 [6].

The activation of a NW device shown in Fig. 5.5 (a) depends strongly on the electrode material used. In fact, the electrical behaviour, in terms of switching capabilities, change drastically if the contacting electrodes are realized using Au or Ag metal deposition. We know that the formation of a conducting filament in the wire junctions is driven by ion migration that require electroactive metal ions. These ions (Ag ions resulted from the redox reactions in this specific case), create two bridges within the TiO_2 active layer switching the device into the ON state, with Ag metal ions from the electrode and the core both being involved. No such switching is observed for Au contacted wires since a complete circulate cannot be formed and with the further application of the electrical stress to an electrical failure occurs due to the electro migration of Ag ions from within the NWs. On the other hand, having Ag electrodes gives the capability to switch the device between LRS and HRS in a uni or bipolar way as proven in the single wire case [6]. The Ag ions contained in the electrodes act as an ion reservoir that enables the device to switch back and forth between the HRS and LRS without experiencing any electrical breakdown.

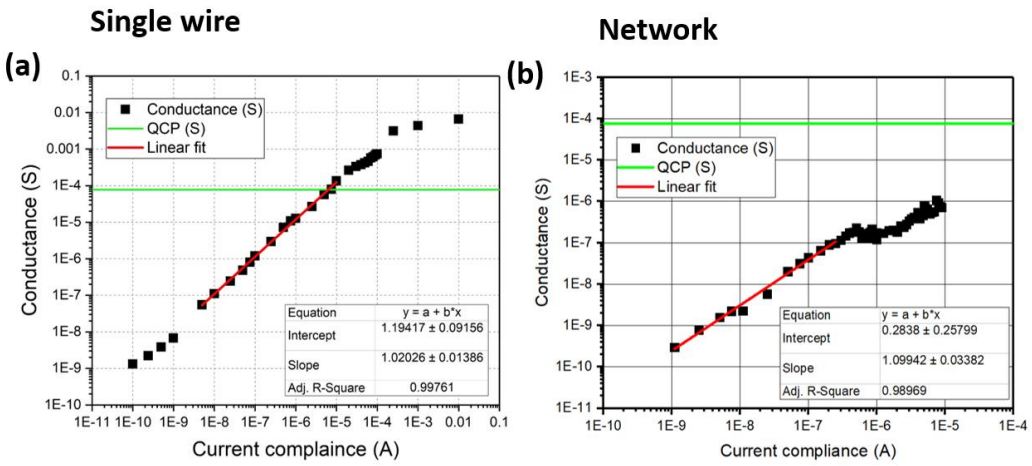

Fig. 5.6 In (a) the scaling curve obtained from the $AgTiO_2$ single wire device with an exponent $\alpha = 1.02$ while in (b) the curve acquired from a $50 \times 50\,\mu m$ $AgTiO_2$ network $\alpha = 1.09$. Comparing the curves and the coefficients extrapolated from the fit confirm the self-similarity introduced in the fourth chapter. Moreover, due to the smaller sampling rate in the case of network it is possible to observe the initial plateau well below the quantum conductance point (QCP) highlighted in green.

The results presented in Fig. 5.6 confirm the self-similar scaling trend that regulates the conductance evolution of a single NW device in Fig. 5.6 (a) and a $50 \times 50\,\mu m$ network in Fig. 5.6 (b). Moreover, comparing the coefficients obtained from the fits show how the α_{nt} is very close to 1.1 while for single wire is instead closer to the unity.

5.1.2 Cu NWNs

As introduced in the first chapter, Cu shows resistive switching properties and in particular a unipolar behaviour [7,8]. Referring to section 1.4 a unipolar device is defined as a two-terminal component that can be switched between HRS and LRS applying the same voltage polarity. Once the CF is fully formed within the active layer, a CuO_x layer in this specific case (see Fig. 2.17), it can be reset by removing the compliance current. If the current flowing within the device creates enough Joule heating the filament will be disrupted switching to the OFF state [9,10].

Focusing on the scaling process, an example of $\Gamma \; vs \; I_{cc}$ curve obtained from a 10 μm network is shown in Fig. 5.7.

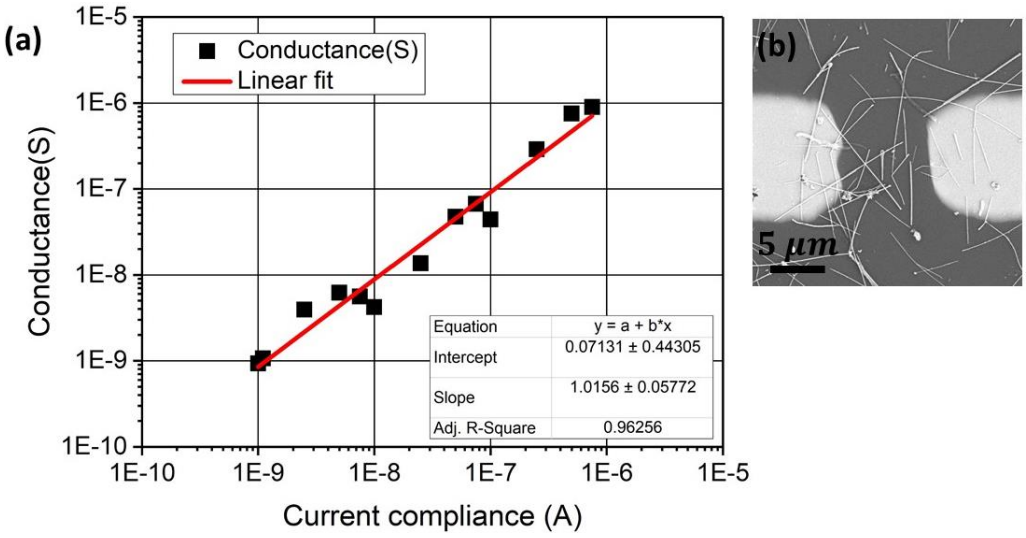

Fig. 5.7 Conductance versus current compliance curve (a) obtained activating the sample shown as inset in (b) realized through shadow mask deposition. From the fit in (a), a slope equals to 1.01 confirms the values reported in Table 4.1. The network fabricated via drop-casting the solution onto the substrate has an electrode (Ti-Au 5-35 nm) distance equal to $10 \; \mu m$.

The exponent taken from the linear fit conducted in Fig 5.7 (a) is equal to 1.01. From a statistical analysis considering over 10 different networks made of Cu NWs, the average exponent is found to be closer to 1 instead of 1.1. Therefore, in order to explain this behaviour we discuss here memristor model to prove that the different coefficient is due to nonlinear effects taking place within the active layer. It is important to remark that in our case we adapted the model to study the growth of the conductive filaments within junctions and in treating networks we are making several simplifications. Following the same approach elaborated by Strukov et al [11] to describe the motion of charges in a TiO_x system and assuming to have a uniform film across the device [12] we have that the electrical response can be written as:

$$V(t) = \left[R_{on}\frac{w(t)}{D} + R_{off}\left(1 - \frac{w(t)}{D}\right)\right] I(t) \quad \text{(Eq. 5.1)}$$

$$\frac{d\,w(t)}{dt} = \mu_v \frac{R_{ON}}{D} I(t) \quad \text{Eq. (5.2)}$$

where t is the time, D is the length of the junction, μ_v is the mobility of the ions within the active layer, $I(t)$ is the current to which the device is subjected and $R_{ON/OFF}$ represents the resistance values respectively of the ON/OFF state. $w(t)$ is a state variable that describes the length of the conductive filament as the time evolves. To describe the evolution of the conductance Γ we refer to an expression based on the tunnelling mechanism shown as follow.

$$\Gamma_j = \Gamma_0 e^{-[\beta(D - w(t))]} \quad \text{Eq. (5.3)}$$

in which Γ_0 is the quantum of the conductance and β is a decay parameter related to the tunnelling barrier. In the limit condition of a full activated junction $D = w(t)$ and the conductance Γ_j corresponds to the quantum conductance Γ_0 as expected. Combining now Eq. (5.2) and Eq. (5.3) assuming sufficiently small tunnel barrier lengths, one can obtain the state equation to describe the filament growth.

$$\frac{dw}{dt} = \frac{A_j}{\beta\Gamma_0} I(t) = \frac{\mu_v}{D\Gamma_0} I(t) \qquad \text{Eq. (5.4)}$$

Eq. (5.4) relates the formation of the CF in terms of the A coefficient enabling a better understanding of why different materials have different A values. Expressing the evolution of the CF in terms of ion mobility we can prove that the A term is strongly influenced by material and for this reason all the curves presented in Fig. 5.1 have similar α but different A values.

A second experiment to test the formation of plateaus performed in Cu NWNs is presented as follow. A very sparse Cu NWs solution was dropcast onto a Si substrate to create networks contacted using a shadow mask through a Ti/Au $5/35\ nm$ deposition. We decide to move to very sparse devices in order to accentuate the presence of the plateaus formation along the activation of the film.

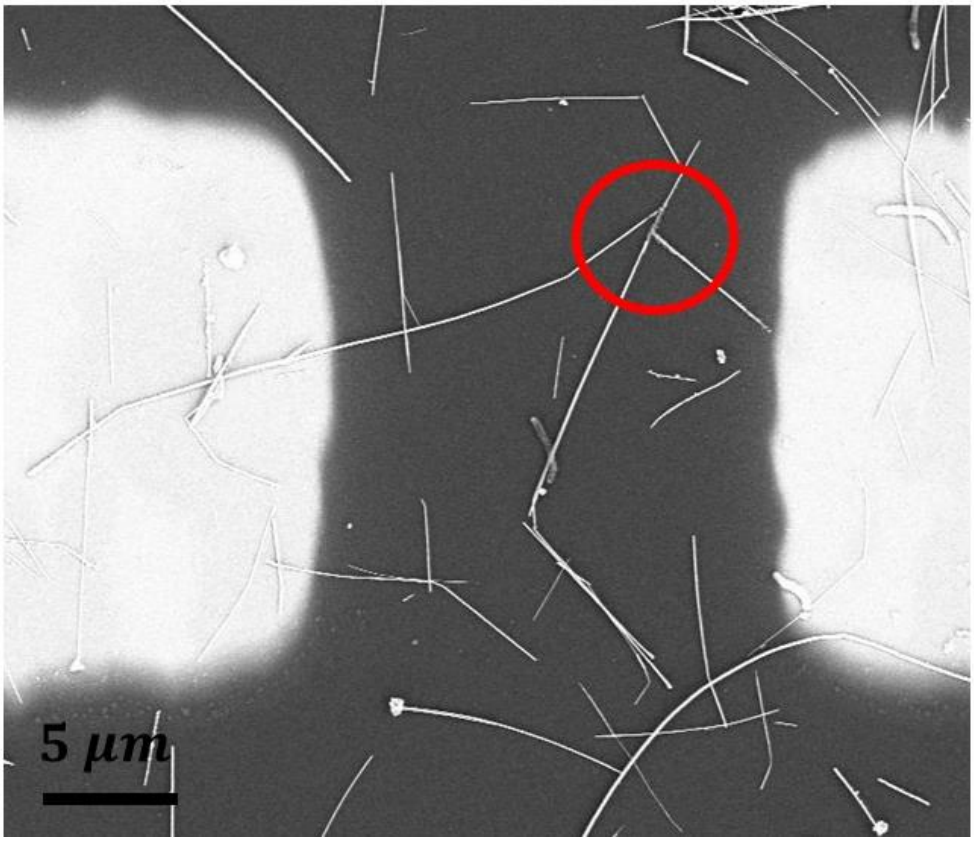

Fig. 5.8 Ultra-sparse Cu NWNs fabricated to have a limited number of junctions between the electrodes $10\ \mu m$. The red circle indicates two of the four junctions that enables the conduction across the device.

This sample has an electrode distance of $10\ \mu m$ and due to the low NWs concentration, the passage of current occurs only through the highlighted NWs (red circle). The resulting $\Gamma\ vs\ I_{cc}$ curve is shown in Fig. 5.9 giving from a fit in the power law regime a slope value of 1.02.

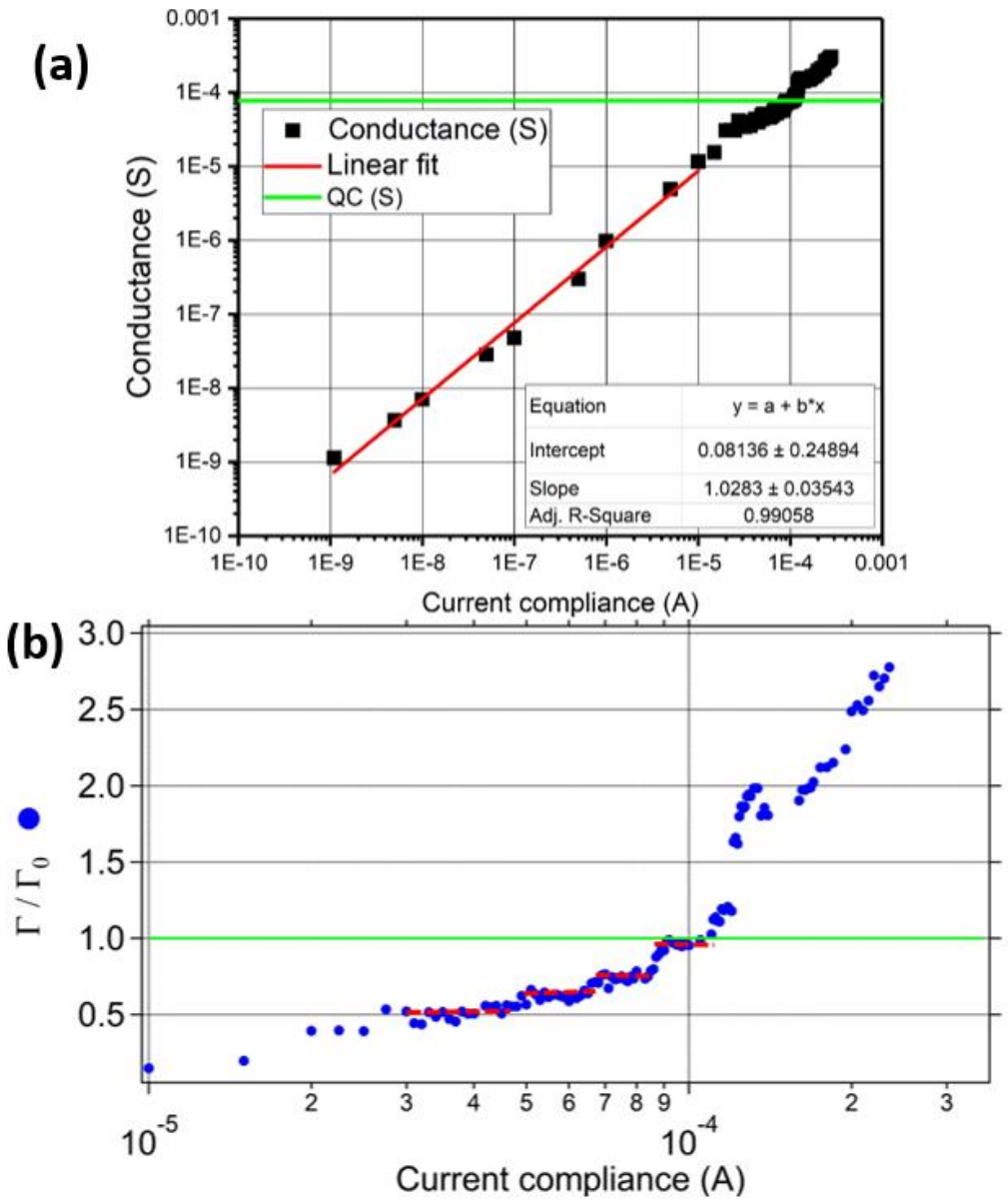

Fig. 5.9 In (a) the conductance vs I_{cc} obtained from the device shown in Fig. 5.8. The same scaling experiment already used previously on Ag@PVP NWNs was used either in this case to highlight the formation of plateaus. The finest sampling rate is utilized in proximity of the expected range following Eq. 4.3. In (b) the experimental data points of (a) are plotted with respect of Γ_0. The red dashed lines indicate four different plateaus associated to the optimization of the junctions in the network.

The first plateau appears for a fraction of the quantum conductance Γ_0 but as the current supplied to the system increases we can see other three plateaus associated to the optimization of the junctions present in the device. Along the activation within the four junctions that bridge the electrodes (two at the interface

NWs-electrodes and two between NW and NW) the tunnelling gap is reduced increasing the conductance of the system. When a filament is completed we have the formation of a plateau until all the four junctions are optimized behaving exactly as a series of quantum conductors (at the fourth plateau $\Gamma_p = \Gamma_0$).

5.1.3 Ni NWs

The last example we will discuss in this section to show the self-similar scaling behaviour among NWN made of different materials is a Ni NWN. These nanowires were bought from the commercial supplier Nanomaterials [13] (see Fig.2.17) deposited on Si substrate and contacted with Ti-Au electrodes using shadow mask.

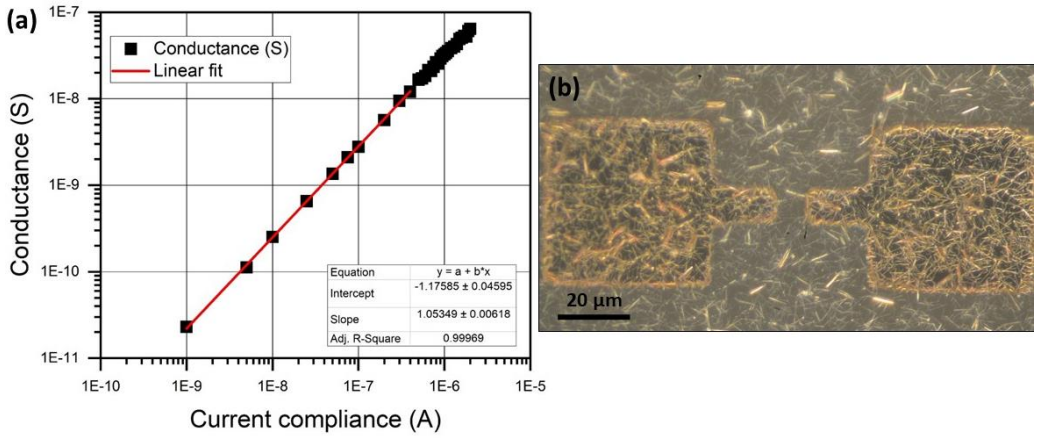

Fig. 5.10 In (a) a scaling curve obtained from a Ni NWNs $(d = 50\ \mu m)$ spray-deposited onto a glass slide. In (b) an optical picture showing a $10\ \mu m$ network device.

The conductance scales with respect to the compliance used to activate the network in the same way as found earlier for Ag and Cu networks. The major difference lies on the fact that in order to drive the system to higher conductance states larger currents are usually required. This can be associated to several factors, one of the major problems comes from the lower mobility, reflected a higher barrier to diffusion with the oxide surface coating for Ni compared with Ag or Cu ions. Another contributor is represented by the higher junction resistances between individual Ni NWs. However, during the scaling despite a reasonably high

current compliance and a good sampling rate, it was not possible to visualize any plateaus along the curve. Therefore, using a second Ni network further pushing the compliance limit to $10\ \mu A$ we tried to highlight the formation of plateaus. The results plotted with respect of the compliance are shown in Fig. 5.11.

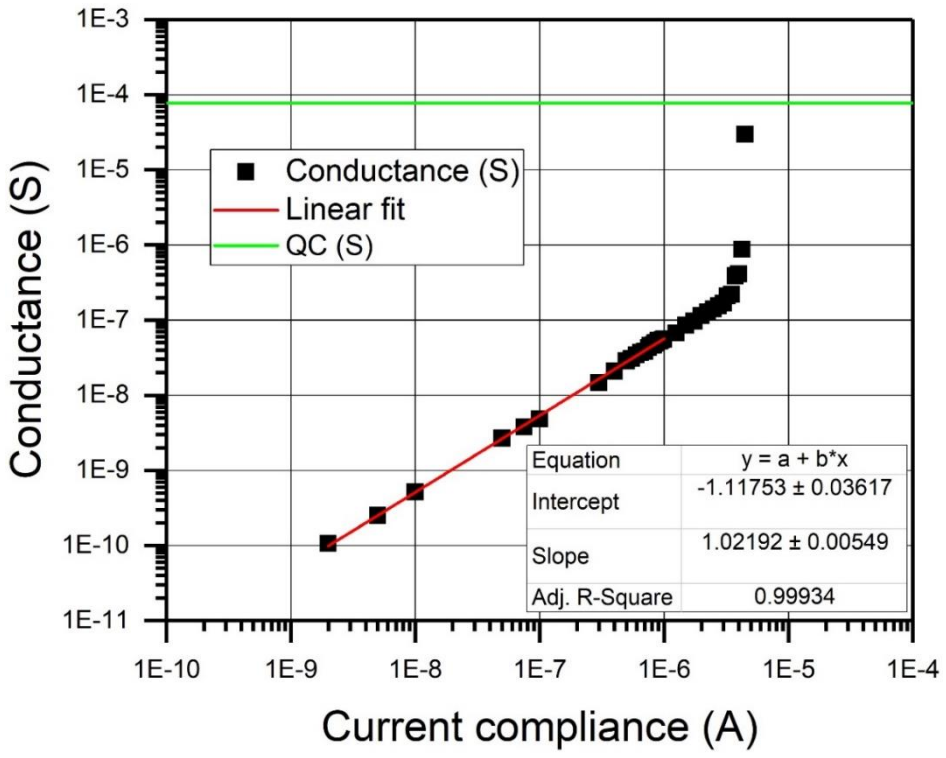

Fig. 5.11 The conductance vs compliance plot shows an abrupt jump when a current compliance of $4\ \mu A$ was used. During the experiments performed on Ni sample we were not able to distinguish any plateau during the measurements. This probably happens because this kind of films, if properly electrically stimulated, experiences an abrupt switching process from the OFF to the ON state.

The linear fit on the power law regime gives a slope equals to 1.02, but more interestingly, when a $I_{cc} = 4\ \mu A$ is used, the conductance experiences a huge jump of a couple of orders of magnitude. This behaviour can be most likely associated to a hard switching mechanism that corresponds to the total activation of the entire film. This hypothesis can be supported by the fact that the exponent from the fit fluctuates around one. In fact, in this case our theory predicts that the activation happens in a more homogenous way. The strengthening rate, defined

in eq. 4.2, is independent from the current compliance (case $\alpha_j = 1$) and the CFs within most of the junctions of the network grow simultaneously forming much more stable connections.

In showing this we have proven how networks made of alternative materials behave similarly to the Ag@PVP network case. We can either confirm that our models are able to describe the conductance evolution of several systems.

The next section aims instead to present the capabilities of the same materials treated in the first part of the chapter in terms of switching properties.

5.2 Switching properties of NWNs

The world of resistive switching devices can be mainly categorized in three major mechanisms: unipolar (URS), bipolar (BRS) and complementary resistive switch (CRS) [9,14]. The devices used in literature to study resistive switching are the classical stack of nanoconfined materials in a sandwich type structures known as MIM cells [15,16]. Despite the different geometry, the mechanisms that differentiate the behaviours between different devices are centred in each case around the chemical reaction involved in the activation process. For example, it is quite common to associate to the unipolar behaviour devices made with NiO or TiO_2 as active layers material [17–19]. On the other hand, devices in which switching is based on ion motion, such Ag or Cu, can be identified as bipolar switching devices [20,21]. The presence of an active electrode acting as reservoir of ions is therefore crucial in this kind of structures. Now, in terms of basic mechanisms, the difference lies on the fact that the first class of devices can be switched through a thermochemical process while in the second case thanks to electrochemical reactions [22,23]. On this basis we now discuss the switching properties of NWNs realized with $AgTiO_2$, Cu and Ni NWs. In the first case we are going to prove how bipolar and unipolar resistive switching can coexist in the same device simply modulating the current compliance used to drive the system in a particular conductance state. In the second part, we move to the unipolar behaviour shown

by Cu and Ni NWNs before to conclude with a brief overview of the sample treated in terms of their switching capabilities.

5.2.1 Nonpolar resistive switching - $AgTiO_2$ NWNs

The coexistence between unipolar and bipolar resistive switching is defined as nonpolar switching behaviour. Here, we show experimental evidence that demonstrates how this behaviour can be achieved in networks made of $AgTiO_2$ NWs. Furthermore, making a comparison with the results obtained by Manning et al. [6] in single $AgTiO_2$ nanowire devices we prove how the capabilities associated to the single NWs, with the due considerations, are directly transferable to networks made of the same material. Despite it might result in an obvious statement, it is not trivial that an object with determined properties maintains the same properties if embedded in a much more complex environment. Consider the properties of a particle or a neuron considered as single unit or interacting in more complex environment such as a condensed phase or a brain.

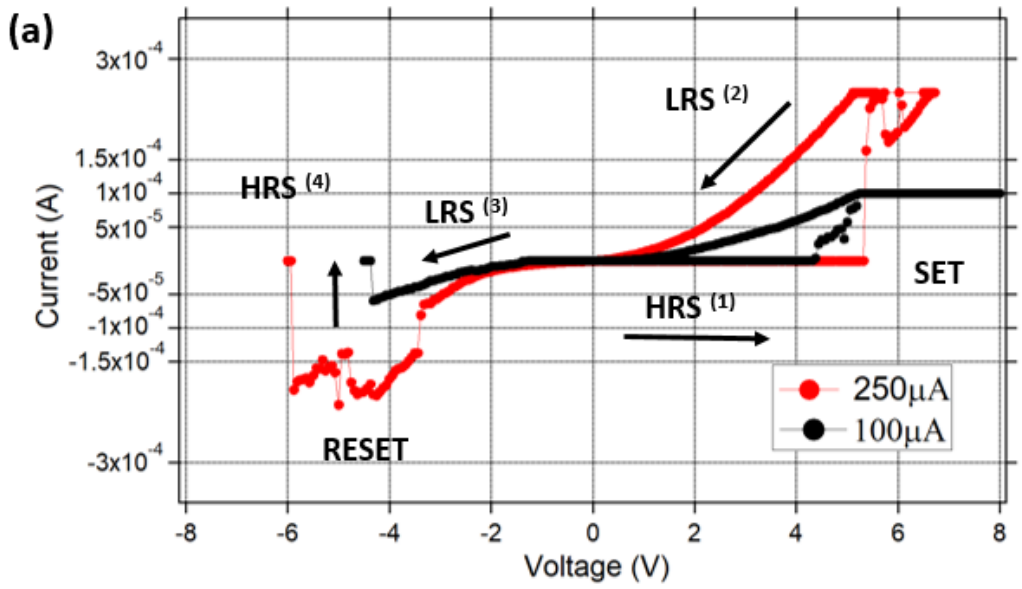

Fig. 5.12 Electrical behaviour of an $AgTiO_2$ network with $d = 50\ \mu m$ that show BRS behaviour at low current compliances $I_{cc} < 750\ \mu A$. The black curve is obtained from a dual sweeps using a compliance of $100\ \mu A$ with a reset voltage of $4.3\ V$. The system initially is in the HRS $^{(1)}$ state, after the SET of the cell the LRS $^{(2)}$ is reached and with the application of a negative voltage the device can be switched again to the HRS $^{(4)}$. The same process is repeated in the subsequent sweep at increased current $250\ \mu A$ requiring a greater voltage to be reset $5.8\ V$.

The electrical bipolar behaviour of an $AgTiO_2$ network $(d = 50\ \mu m)$ is shown in Fig. 5.12. The system initial is in the OFF state, defined as HRS $^{(1)}$, and is activated applying a voltage sweep that once it overcomes a certain threshold, $4\ V$ in this specific case, rapidly decreases the resistance of the film reaching the LRS $^{(2)}$. During the back sweep, in going from positive to negative voltage LRS $^{(3)}$, the resistance remains unchanged until a RESET event occurs. The application of the negative voltage forces the systems to go back into the HRS $^{(4)}$ with resistance value similar to the OFF state prior the activation (few $G\Omega$). On nanoscale level, considering a junction, the application of the voltage enables the growth of the filament but on a larger scale, in the case of NWNs, it involves the formation of multiple filament, one for each junctions of the WTA path, to enable conduction. The subsequent voltage sweep at increased compliance current, red current trace in (a), shows again the same bipolar resistive switching behaviour. The higher compliance enable us to drive further the conductivity decreasing the tunnelling

gap within the junctions consequently increasing the reset voltage needed to switch off the system. Disrupting a more stable connection usually requires higher voltages as can be seen from Fig. 5.12 (a) in which the $V_{RESET} = -4\ V$ for the $100\ \mu A$ case and $-6\ V$ for $250\ \mu A$. The trend is similar to the case of single wire device (see inset Fig. 5.13) with the V_{RESET} following the increase of the compliance used to sweep the voltage. This difference in V_{RESET} magnitude can be attributed to the dimension of the actual sample under study however it is reasonable to think that larger devices will require higher voltages for a reset event. The increase in the compliance utilised to modulate the conductance of the film causes the switching between the bipolar (BRS) and unipolar (URS) resistive switching. This condition occurs when a current compliance of $750\ \mu A$ is used as shown in Fig. 5.13. The application of a negative voltage is not sufficient anymore to reset the device that in order to be reset will require voltage sweeps without current compliance. However, similarly to networks, even in the case of single NW device the change between BRS to URS behaviours is related to the current compliances used to perform the measurements. In fact, as can be seen from the inset of Fig. 5.13, the electrical behaviour of a single wire device [6] is practically identical to the network one. The only difference is represented by the different current range needed to change regime that is equal to $750\ \mu A$ for NWNs and $150\ \mu A$ for single wire device but once again this is merely related to the actual dimensions of the device.

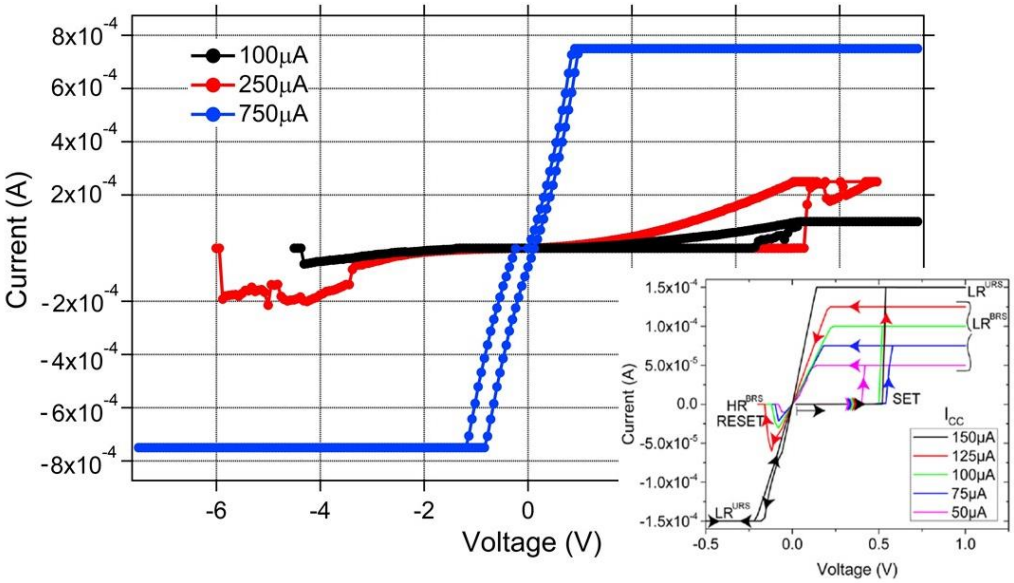

Fig. 5.13 Current traces obtained from the $AgTiO_2$ NWN shown in Fig. 5.12 at higher I_{cc}. Increasing the current compliance causes the system to change its behaviour from bipolar to unipolar. As inset, the similar behaviour obtained from a single wire devices [6] in which the only difference is related to the current compliances used. The transition from BRS to URS happens most likely when the CFs are fully optimized and a hard switching effect occurs, just as in Ni systems do, switching to the unipolar resistive switching trend.

Unfortunately, due to the limitation of the experimental setup (see section 2.6), during the electrical characterization of the NWNs we were not able to reset the network. But it is reasonable to think that stressing the network in a more pronounced way will cause the rupture of the CFs by Joule effect switching the device into the OFF state. In Fig. 5.14 a second network of smaller size is used to prove that with sufficient current the network can be reset. Since the wire density is maintained constant, decreasing the electrode distance from $20\ \mu m$ to $10\ \mu m$ will reduce the number of NWs accordingly lowering the energy required to reset the film.

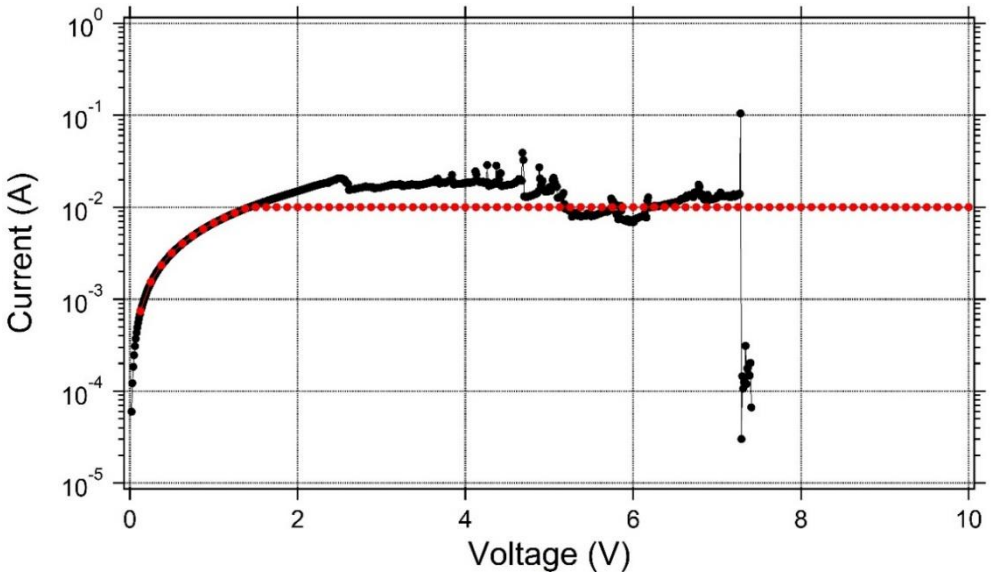

Fig. 5.14 Data obtained for a $10\ \mu m$ $AgTiO_2$ network. The first sweep in red activates the sample. The second one without compliance current (black curve) proves the unipolar characteristic of the film that under sufficient current can be reset.

The red curve represents the initial sweep from $0\ V$ to $20\ V$ used to activate the NWN ($10\ \mu m$). A second voltage sweep, in black, with $100\ mA$ compliance current was then sufficient to reset the network to the OFF state passing from a resistance value of few thousands of Ω to $M\Omega$. When a current of $20\ mA$ flows within the device the resistance starts to deteriorate until, after an abrupt jump, the device definitely turns OFF around $7V$.

Therefore, from the experimental evidence shown in this section we can infer that, despite the different dimensions, both the systems networks and wires behave in a similar way. Without treating the problem from a theoretical point of view we can conclude confirming that the properties of single wire device are directly transferable to networks with some slightly adjustments related to the current compliance used to obtain different electrical behaviours.

5.2.2 Unipolar resistive switching - Cu NWNs

Two examples of networks that behave as unipolar resistive switching are studied in the following. The first device treated is a network realized with Cu NWs while later in this section some experimental evidences of switching will be either shown considering Ni NWNs. Fig. 5.16 shows the sample used to study the electrical behaviour of Cu NWs.

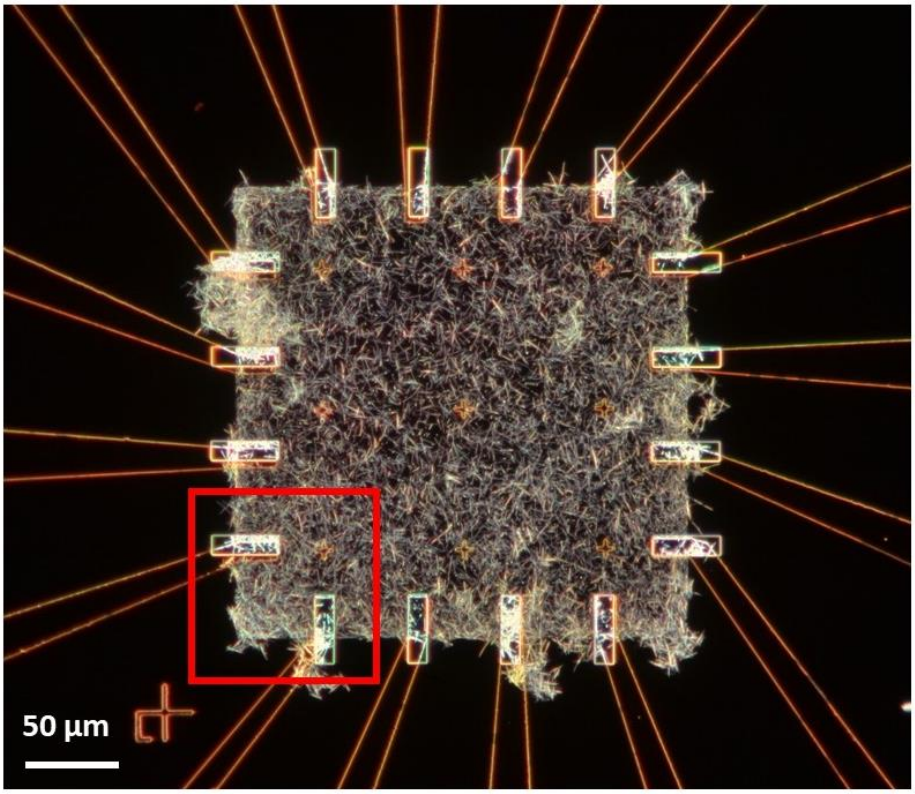

Fig. 5.15 Optical image of a Cu NWN obtained in a two steps. The first step involves the spinning of a resist on the substrate followed by an EBL exposure to illuminate the network area. The NWs were then spray deposited and after the lift-off, the area not exposed during the EBL, along with the NWs on top, is removed. The portion of the network used to electrically test the behaviour of Cu NWNs is highlighted in red and the distance between the two electrodes, taken from the diagonal, is $35\ \mu m$.

A common two point measurements approach was used to activate the highlighted part of the network (red square in Fig. 5.16) and monitor its response as the compliance current changes. The relative current traces obtained from a

voltage sweep are reported in Fig. 5.16. An initial compliance of $5\ \mu A$ was used to switch the device from the HRS to the LRS. The voltage is ramped up in a non-linear fashion in the HRS (1) until the threshold voltage required to turn on the entire film is reached. In the back trace (when the system is in the LRS (2)), the current remains unaltered until the end of the sweep. The subsequent voltage sweeps, recorded at larger current values (in blue), have a compliance equals to $0.5\ \mathrm{mA}$ that is still not enough to return the system to the OFF state. Only when the compliance is set to $100\ mA$ (red curve) the device experiences a reset event and the current has a sudden drop of four order of magnitudes.

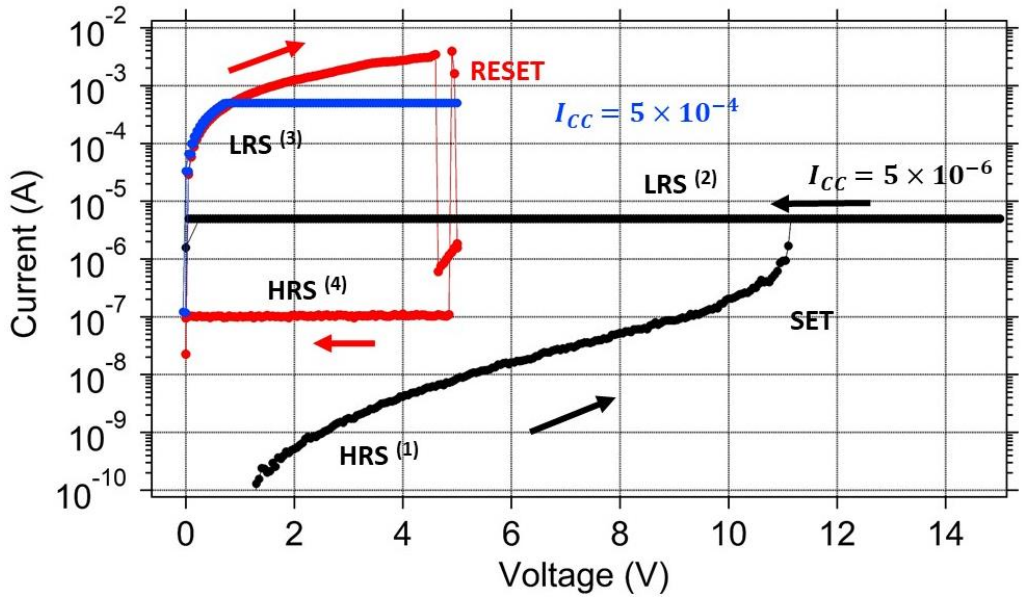

Fig. 5.16 Unipolar resistive switching obtained from a $35\ \mu m$ Cu NWN. The initial sweep in black is performed to activate the film that goes from a resistance of several $G\Omega$ to $M\Omega$. The following voltage sweep is repeated at increased compliances until, with a compliance of $100\ mA$ (red curve), the network experiences a reset operation.

In this condition (HRS (4)) the network has a resistance value of roughly $70\ M\Omega$ but the application of subsequent voltage sweeps can re-activate the sample going back and forth from the HRS to the LRS.

5.2.3 Unipolar resistive switching - Ni NWNs

Similar considerations can be either made for the case of Ni NWs. Fig. 5.17 shows the activation, in black, and the following voltage sweep with a compliance of $I_{cc} = 1\ mA$ used to reset the Ni network.

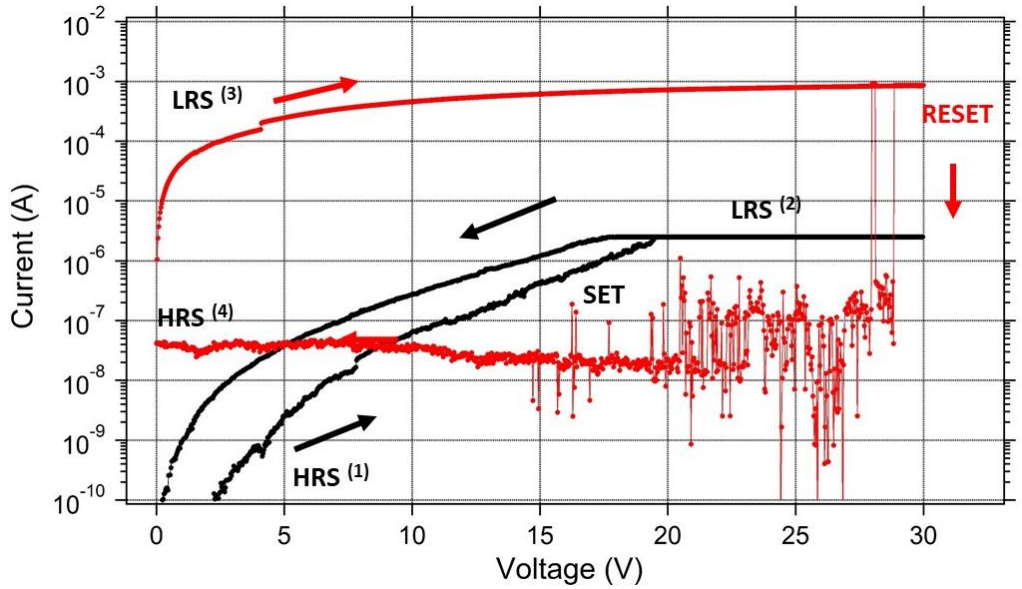

Fig. 5.17 SET and RESET obtained from a $50 \times 50\ \mu m$ Ni network. The activation, in black in the graph, is performed with a voltage dual sweep from $0\ V$ to $30\ V$. The system goes from the high resistance state (1) to its low resistance state (2). The next sweep has a compliance current equal to $1\ mA$. In this case the curve starts from a LRS [(3)] but approximately at $30\ V$ the network switches OFF to a HRS [(4)].

The first activation of the network, black curve in the figure, is performed using a voltage dual sweep $0\ V \rightarrow 30\ V \rightarrow 0\ V$. Even in this case the system goes from its HRS to the LRS when the V_{on} is reached. The larger voltage, if compared with the previous case, is simply due to the larger sizes of the device $50 \times 50\ \mu m$ and to the higher resistance associated to the Ni junctions. However, once the network is in the LRS [(2)] the resistance associated to the network are comparable to the Cu case. The reset event is performed repeating the same voltage dual sweep starting from the LRS (3) until the V_{reset} equal to $29\ V$ in this case in which the resistance goes from $30\ k\Omega$ to few $G\Omega$.

5.3 Conclusion

Looking now at the entire picture, this chapter underlines the weaknesses and the advantages of the different materials treated so far. From the discussions presented in the previous chapters we learnt how the activation occurs in NWNs. It is either possible to identify from the scaling curve if the network will prefer the activation creating a single WTA paths or through multiple simultaneous paths. But this is thanks to the utilization of different materials that we have the control to switch the network between the ON and OFF state. This is a fundamental step towards the final goal of implementation in memory or neuromorphic devices [24,25]. From what we saw in this chapter $AgTiO_2$ NWNs represents without a doubt the best solution. Its ductility and versatility grant the possibilities of having bipolar or unipolar switching using the same device. Using different compliances enables the modulation of parameters such as retention time, resistance ratio and endurance of the device [6].

On the other hand, Cu or Ni NWNs might represent a viable solution for unipolar behaviour. With respect to the core-shell $Ag@TiO_2$ NWs those materials are much more studied and therefore the conduction mechanism within $Cu@CuO_x$ or $Ni@NiO_x$ is a very well-studied problem [17,25–27]. Moreover, they can be either used as alternative materials with lower scaling coefficient giving the possibility to choose the kind of the activation needed according the application requirements. Ag NW networks are a more versatile solution used during this study as a platform to understand the mechanism beyond the activation of networks. Unfortunately, Ag NWs do not allow the RESET operation drastically limiting its usage.

Despite more tests are required to prove the reproducibility of the results, the data shown in this chapter are very promising. Further experiments are needed to study in a detailed way the endurance, retention time and the timing required to write/read the information from the device. Moreover, focusing on what we studied so far, we can infer that the energy consumption is one of the key parameters that might boost the use of NWNs in memory devices. The energy cost required to SET and RESET the device, taking the $AgTiO_2$ NWNs as example, is very

low if compared with commercial devices [18,28]. In fact, the energy to SET and RESET a NWN is well below the mJ range, approximately $200\ \mu J$ in the bipolar regime and few mJ for the unipolar one. However, in reality for a $50\ \mu m$ network the SET/RESET operation involves tenths or even thousands of junctions further lowering the energy required to write/read the information on a single cell level.

Another remarkable advantage of NWNs is the capabilities in modulating the conductance states changing the current compliance. This allows multilevel resistance states for storage information with different retention times.

References

1. Xu, L. *et al.* One-Step Synthesis of Au-Ag Nanowires through Microorganism-Mediated, CTAB-Directed Approach, (2018).
2. Xu, Y., Chen, L., Wang, X., Yao, W. & Zhang, Q. Recent advances in noble metal based composite nanocatalysts: Colloidal synthesis, properties, and catalytic applications, (2015).
3. Jana, N. R., Gearheart, L. & Murphy, C. J. Wet chemical synthesis of silver nanorods and nanowires of controllable aspect ratio, (2001).
4. Lee, H. S. *et al.* Synthesis of dimension-controlled silver nanowires for highly conductive and transparent nanowire films, (2015).
5. Korte, K. E., Skrabalak, S. E. & Xia, Y. Rapid synthesis of silver nanowires through a CuCl- or $CuCl_2$ -mediated polyol process, (2008).
6. Manning, H. G., Biswas, S., Holmes, J. D. & Boland, J. J. Nonpolar Resistive Switching in Ag@TiO 2 Core−Shell Nanowires, (2017).
7. Chen, C., Yang, Y. C., Zeng, F. & Pan, F. Bipolar resistive switching in Cu/AlN/Pt nonvolatile memory device, (2010).
8. Schindler, C., Thermadam, S. C. P., Waser, R. & Kozicki, M. N. Bipolar and unipolar resistive switching in cu-doped SiO2, (2007).
9. Ielmini, D., Nardi, F. & Cagli, C. Universal reset characteristics of unipolar and bipolar metal-oxide RRAM, (2011).
10. Jeong, W., Kim, K., Kim, Y., Lee, W. & Reddy, P. Characterization of nanoscale temperature fields during electromigration of nanowires, (2014).
11. Strukov, D. B., Snider, G. S., Stewart, D. R. & Williams, R. S. The missing memristor found, (2008).
12. Manning, H. G. *et al.* Emergence of winner-takes-all connectivity paths in random nanowire networks, (2018).
13. https://nanomaterials.iolitec.de/en.
14. W. Lu et al. Electrochemical metallization cells - Blending nanoionics into nanoelectronics?, (2012).
15. Valov, I. & Kozicki, M. N. Cation-based resistance change memory, (2013).
16. I. Valov,S. Tappertzhofen, E. Linn, S. Menzel, J. van den Hurk, and R. W. *et al.* Atomic Scale and Interface Interactions in Redox-Based Resistive Switching Memories, (2014).
17. Oka, K., Yanagida, T., Nagashima, K., Tanaka, H. & Kawai, T. Nonvolatile Bipolar Resistive Memory Switching in Single Crystalline NiO Heterostructured Nanowires, (2009).
18. Kwon, D.-H. *et al.* Atomic structure of conducting nanofilaments in TiO_2 resistive switching memory, (2010).
19. Kim, K. M., Jeong, D. S. & Hwang, C. S. Nanofilamentary resistive switching in binary oxide

system; a review on the present status and outlook, (2011).

20. Guo, H. X. *et al.* The growth of metallic nanofilaments in resistive switching memory devices based on solid electrolytes, (2009).
21. Li, Q. *et al.* Applied Physics Express Flexible transparent memory cell: bipolar resistive switching via indium–tin oxide nanowire networks on a poly(dimethylsiloxane) substrate, (2016).
22. Yang, Y. *et al.* Observation of conducting filament growth in nanoscale resistive memories, (2012).
23. Tappertzhofen, S., Valov, I. & Waser, R. Quantum conductance and switching kinetics of AgI-based microcrossbar cells, (2012).
24. Linn, E., Menzel, S., Ferch, S. & Waser, R. Compact modeling of CRS devices based on ECM cells for memory, logic and neuromorphic applications, (2013).
25. Tu, C.-H. *et al.* Resistive memory devices with high switching endurance through single filaments in Bi-crystal CuO nanowires, (2014).
26. Liang, K.-D. *et al.* Single CuO x Nanowire Memristor: Forming-Free Resistive Switching Behavior, (2014).
27. Cagli, C. *et al.* Resistive-Switching Crossbar Memory Based on Ni-NiO Core-Shell Nanowires, (2011).
28. J. Meena, S. Min Sze, U. Chand and T. Tseng. Overview of emerging nonvolatile memory technologies, (2014).

Chapter 6

Conclusions

During this PhD project, the electrical properties of NWNs were studied in detail along with the activation of the film. Below, we highlight the main points and conclusions drawn from this thesis.

Within the first chapter, the basic notions regarding the NWNs were discussed. A general overview of the state-of-the-art of memristor devices helped to address the main objectives of this study by introducing the so called MIM devices. Through an overview of the literature, three different types of memory ECM, VCM and TCM were introduced. According to the chemical process driving the activation of the MIM cell the formation of the conductive filaments were described in detail. After this introductive part, the focus was then moved to the potential of the NWNs. Several applications were discussed, including the requirements for transparent conductors memory and neuromorphic devices.

The second chapter describes the techniques used to realize and characterize devices and the underlying theory of the physical principles involved. The scanning electron microscope is the principal instrument used across this PhD project to image and create devices. The interaction between the electron beam and the sample was explained in detail to understand the different working principles of SEM and TEM. Particular attention was given to the electron beam lithography that used throughout the project for fabrication purposes. Moreover, another important advantage of SEMs is the possibility to visualize different levels of contrast during the imaging of samples. Through this voltage contrast technique, the formation of the electrical paths within networks was highlighted at different stages of the activation. Furthermore, all the fabrication processes to

fabricate single wire/junctions devices and networks were described. Through a mix & match approach UV lithography and EBL enable us to electrically contact nanoscale objects with sub μm resolution. Through the first UV lithography step, features on mm scale can be deposited over a large while the finest features are realized with the EBL electrically contacting NWs. In the latter case the capabilities of the SEM are exploited reaching resolution below the μm scale. Furthermore, the steps required to fabricate networks were reported. Through an initial spray deposition step, NWs are deposited over large surfaces and contacted with shadow masks to realize actual devices. Thanks to the high scalability of the process a large number of devices can be fabricated simultaneously prior to the electrical characterization. The chapter ends by describing the setup used to perform the electrical tests on NWs devices.

The third chapter is the first experimental chapter in which the basis of our experimental approaches to characterize the NWNs are introduced. A brief overview on the current state of the art regarding the activation of highly disordered NWNs is used to introduce the readers. After that, we introduce the "tools" required across the project to describe the activation processes, the capacitive and memristive models. Employing these two models we were able to fully describe the connectivity evolution of networks through the formation of CFs within the junctions comprising them. The CFs formation was further characterized through investigation at different temperatures and studying their retention time in single junctions and network devices.

The results acquired from a single wire and junctions devices provide the basis for our "part to whole" approach to describe the evolution of networks. The experimental evidence was used as feed to simulate the activation process within networks to enable us to introduce a self-similar scaling behaviour between the network conductance at the current flowed through the system. The constant sharing of information between experimental and simulated results led us to the visualization of plateaus along $\Gamma \; vs \; I_{cc}$ related to the electrical optimization of what we define as "winner-takes-all" paths. These paths, that span the entire network, can be considered as the most favourable configuration for signal

propagation. When the CFs within the junctions of the WTA paths are optimized the conductance for a very narrow window remain unchanged, behaving like common resistors in series. By overcoming a certain current threshold, the voltage is redistributed across the film causing the adjacent junctions to join the main path. The overall conductance increases until the entire film is activated. To prove the accuracy of our model, we directly visualized the presence of the WTA paths through PVC images, which also helped define three different regimes along the activation process. An initial phase in which the network is capacitively probed and during which it self-selected the most favourable paths is defined as the transient regime. A second stage characterized by a power law regime in which the current is sufficient to start the formation of the CFs through redox reactions happening at the junction level and a final part where multiple electrical paths emerge. Moreover, utilizing the Von Neumann entropy we showed that the formation of WTA paths results in entropy minimisation and the current localisation that represent the most effective way to activate NWNs by transferring the information across the film.

The fifth chapter includes an analysis of different NWs materials. The knowledge acquired from Ag NWNs used as platform materials are exploited to describe the activation process on devices realized with different materials. Thanks to our collaborator from UCC, a wide range of materials and structures were been tested across the PhD projects. One of the most interesting cases is represented by the core-shell Ag@TiO_2 NWs. Based on the current used to set these devices, networks made of Ag@TiO_2 NWs show nonpolar resistive switching capabilities in which either bipolar or unipolar behaviour can be achieved. For compliance currents lower than $750\ \mu A$ networks act as bipolar resistive switching device but when larger currents are used the system enters into a hard switching state in which the CFs can be dissolved only through Joule heating, typical of unipolar devices. Two additional types of core-shell NWs were tested. Cu@CuOx and Ni@NiOx NWs both show unipolar behaviour regardless of the current compliance or device dimension used. Ni NWNs when electrical stressed, switch to a hard resistive state as Ag@TiO_2 NWNs do. On the other hand, Cu NWNs

showed larger plasticity in modulating the conductivity of the film comparing with Ni case. This was demonstrated by the fact that the presence of plateaus was observable in Cu networks but not in Ni ones.

Future and perspectives

The aim of this PhD project was to elucidate the activation process within randomly oriented nanowire networks. In order to achieve this goal, a bottom-up approach was used gathering information from single junction devices to simulate the electrical behaviour of more complex structures such as networks. Thanks to the interplay of the experimental and simulation, a new dynamical model emerged that helped to unveil three different stages along the activation process. We have shown that a particular class of materials self-select WTA paths within the film minimizing the energy required to create a stable electrical connection. A future step in the context of devices implementation is represented by core-shell NWs. These nanostructures exhibited remarkable switching properties that enable the programmability of the film. This, along with the notions about WTA paths, open a wide window on different research fields. In keeping the conductance of NWN below the plateau level, gives us the possibility to access to multi-storage levels in which the retention of the information is directly related to the amount of current flown within the device.

Following this, the next step is the realization of a platform that enables us to supply different voltage stimulus in different positions of the network. In delivering the electrical signals, pulses or sweeps, one can in principle perform I/O operations storing simultaneously information in different areas of the film. The action of the current compliance will be crucial since it might drastically influence the response of the film to input probe pulses that monitor the connectivity and memory conductance level. However, one of the most interesting challenge will be the extrapolation of the information out of the network once the writing operation is performed.